Heart & Brain. Linking cardiovascular pathologies and neurodegeneration with a combined biophysical and statistical methodology

Jaume Banus

UNIVERSITÉ CÔTE D'AZUR

ÉCOLE DOCTORALE
SCIENCES ET TECHNOLOGIES DE L'INFORMATION ET DE LA COMMUNICATION

THÈSE DE DOCTORAT

Coeur & Cerveau: lien entre les pathologies cardiovasculaires et la neurodégénérescence par une approche combinée biophysique et statistique

Jaume BANUS COBO

INRIA, Équipe EPIONE

Thèse dirigée par Maxime SERMESANT et co-dirigée par Marco LORENZI et Oscar CAMARA

Soutenue le 26 Mai, 2021

Présentée en vue de l'obtention du grade de DOCTEUR EN AUTOMATIQUE, TRAITEMENT DU SIGNAL ET DES IMAGES de l'UNIVERSITÉ CÔTE D'AZUR.

Devant le jury composé de :

Alistair YOUNG	King's College London	Rapporteur
Boudewijn LELIEVELDT	Leiden University Medical Center	Rapporteur
Juan Domingo GISPERT	Barcelonaβeta Brain Research Center	Examinateur
Frederik BARKHOF	VU University Medical Center Amsterdam	Examinateur
Maxime SERMESANT	Inria Sophia Antipolis	Directeur de thèse
Marco LORENZI	Inria Sophia Antipolis	Co-directeur de thèse
Oscar CAMARA	Universitat Pompeu Fabra	Co-encadrant

Epione e-patient / e-medicine

Inria

upf. Universitat Pompeu Fabra Barcelona

Membres du Jury

Titre français
Coeur & Cerveau: lien entre les pathologies cardiovasculaires et la neurodégénérescence par une approche combinée biophysique et statistique

Titre anglais
Heart & Brain: Linking Cardiovascular Pathologies and Neurodegeneration with a Combined Biophysical and Statistical Methodology

Devant le jury composé de :

Rapporteurs

Alistair YOUNG, Professeur, King's College London
Boudewijn LELIEVELDT, Professeur, Leiden University Medical Center

Examinateurs

Juan Domingo GISPERT, Directeur de recherche, Barcelonaβeta Brain Research Center
Frederik BARKHOF, Professeur, VU University Medical Center Amsterdam
Maxime SERMESANT, Chargé de recherche - HDR, Inria Sophia Antipolis
Marco LORENZI, Chargé de recherche - HDR, Inria Sophia Antipolis
Oscar CAMARA, Professeur, Universitat Pompeu Fabra

Abstract

Clinical studies have identified several cardiovascular risk factors associated to dementia and cardiac pathologies, but their pathological interaction remains poorly understood. Classically, the investigation of the heart-brain relationship is mostly carried out through statistical analysis exploring the association between cardiac indicators and cognitive biomarkers. This kind of investigations are usually performed in large-scale epidemiological datasets, for which joint measurements of both brain and heart are available. For this reason, most of these analyses are performed on cohorts representing the general population. Therefore, the generalisation of these findings to dementia studies is generally difficult, since extensive assessments of cardiac and cardiovascular function in currently available dementia dataset is usually lacking. Another limiting factor of current studies is the limited interpretability of the complex pathophysiological relations between heart and brain allowed by standard correlation analyses. Improving our understanding of the implications of cardiovascular function in dementia ultimately requires the development of more refined mechanistic models of cardiac physiology, as well as the development of novel approaches allowing to integrate these models with image-based brain biomarkers. To address these challenges, in this thesis we developed new computational tools based on the integration of mechanistic models within a statistical learning framework.

First, we studied the association between non-observable physiological indicators, such as cardiac contractility, and brain-derived imaging features. To this end, the parameter-space of a mechanistic model of the cardiac function was constrained during the personalisation stage based on the relationships between the parameters of the cardiac model and brain information. This allows to tackle the ill-posedness of the inverse problem associated to model personalisation, and obtain patient-specific solutions that are comparable population-wise.

Second, we developed a probabilistic imputation model that allows to impute missing cardiac information in datasets with limited data. The imputation leverages on the cardiac-brain dynamics learned in a large-scale population analysis, and uses this knowledge to obtain plausible solutions in datasets with partial data. The generative nature of the approach allows to simulate the evolution of cardiac model parameters as brain features change. The framework is based on a conditional variational autoencoder (CVAE) combined with Gaussian process (GP) regression.

Third, we analysed the potential role of cardiac model parameters as early biomarkers for dementia, which could help to identify individuals at risk. To this end, we imputed missing cardiac information in an Alzheimer's disease (AD) longitudinal cohort. Next, via disease progression modelling we estimated the disease stage for each individual based on the evolution of biomarkers. This allowed to obtain a model of the disease evolution, to analyse the role of cardiac function in AD, and to identify cardiac model parameters as potential early-stage biomarkers of dementia.

These results demonstrate the importance of the developed tools by providing clinically plausible associations between cardiac model parameters and brain imaging features in an epidemiological dataset, as well as highlighting insights about the physiological relationship between cardiac function and dementia biomarkers. The obtained results open new research directions, such as the use of more complex mechanistic models that allow to better characterise the heart-brain relationship, or the use of biophysical cardiac models to derive in-silico biomarkers for identifying individuals at risk of dementia in clinical routine, and/or for their inclusion in neuroprotective trials.

Keywords: medical imaging, cardiovascular modelling, neurodegeneration, lumped models, machine learning, variational autoencoder, Gaussian process, personalisation.

Résumé

Les études cliniques ont identifié plusieurs facteurs de risque cardiovasculaire associés à la démence et aux pathologies cardiaques, mais leur interaction pathologique reste mal comprise. Habituellement, l'étude de la relation cœur-cerveau est principalement réalisée à travers d'analyses statistiques explorant l'association entre les indicateurs cardiaques et les biomarqueurs cognitifs. Ce type d'étude est généralement réalisé dans des bases de données épidémiologiques à grande échelle, pour lesquelles des mesures conjointes du cerveau et du cœur sont disponibles. Pour cette raison, la plupart de ces analyses sont effectuées sur des cohortes représentant la population générale. Par conséquent, la généralisation de ces résultats aux études sur la démence est difficile, car les évaluations approfondies des fonctions cardiaques et cardiovasculaires dans les bases de données sur la démence actuellement disponibles font généralement défaut. Un autre facteur limitatif des études actuelles est l'interprétabilité limitée des relations physiopathologiques complexes entre le cœur et le cerveau que permettent les analyses de corrélation standard. L'amélioration de notre compréhension des implications de la fonction cardiovasculaire dans la démence nécessite finalement le développement de modèles mécniaques de la physiologie cardiaque plus raffinés , ainsi que le développement de nouvelles approches permettant d'intégrer ces modèles avec des biomarqueurs cérébraux basés sur l'image. Pour relever ces défis, nous avons développé dans cette thèse de nouveaux outils informatiques basés sur l'intégration de modèles mécaniques dans un cadre d'apprentissage statistique.

Premièrement, nous avons étudié l'association entre des indicateurs physiologiques non observables, tels que la contractilité cardiaque, et des caractéristiques d'imagerie dérivées du cerveau. À cette fin, l'espace des paramètres d'un modèle mécanique de la fonction cardiaque a été contraint pendant l'étape de personnalisation sur la base des relations entre les paramètres du modèle cardiaque et les informations cérébrales. Cela permet d'attenuer le caractère mal defini du problème inverse associé à la personnalisation du modèle, et d'obtenir des solutions spécifiques au patient qui sont comparables au sein de la population.

Deuxièmement, nous avons développé un modèle d'imputation probabiliste qui permet d'imputer les informations cardiaques manquantes dans des bases de données limitées. L'imputation repose sur les dynamiques cœur-cerveau apprises à partir de l'analyse d'une grande population de sujets, et utilise cette connaissance pour obtenir des solutions plau-

sibles dans des bases de données partielles. La nature générative de l'approche permet de simuler l'évolution des paramètres du modèle cardiaque lorsque les caractéristiques du cerveau changent. Le cadre est basé sur un "conditional variational autoencoder" (CVAE) combiné à une régression "Gaussian process" (GP).

Troisièmement, nous avons analysé le rôle potentiel des paramètres du modèle cardiaque comme biomarqueurs précoces de la démence, ce qui pourrait aider à identifier les individus à risque. Dans ce but, nous avons imputé les informations cardiaques manquantes dans une cohorte longitudinale de la maladie d'Alzheimer. Ensuite, grâce à la modélisation de la progression de la maladie, nous avons estimé le stade de la maladie pour chaque individu sur la base de l'évolution des biomarqueurs. Ceci a permis d'obtenir un modèle de l'évolution de la maladie, d'analyser le rôle de la fonction cardiaque dans la maladie d'Alzheimer, et d'identifier les paramètres du modèle cardiaque comme biomarqueurs potentiels de la démence à un stade précoce.

Les résultats démontrent l'importance des outils développés en obtenant des associations cliniquement plausibles entre les paramètres du modèle cardiaque et les caractéristiques de l'imagerie cérébrale dans une base de données épidémiologiques. Ces résultats mettent également en évidence des informations sur la relation physiologique entre la fonction cardiaque et les biomarqueurs de la démence. Les résultats obtenus ouvrent de nouvelles voies de recherche, telles que l'utilisation de modèles mécaniques plus complexes permettant de mieux caractériser la relation cœur-cerveau, ou l'utilisation de modèles cardiaques biophysiques pour dériver des biomarqueurs in-silico afin d'identifier les individus à risque de démence dans la routine clinique, et/ou pour leur inclusion dans des essais neuroprotecteurs.

Mots-clés: imagerie médicale, modélisation cardiovasculaire, neurodégénérescence, modèles regroupés, apprentissage automatique, autoencodeur variationnel, processus Gaussien, personnalisation

Acknowledgements

I would like to thank first my thesis supervisors, Maxime Sermesant, Marco Lorenzi and Oscar Camara. Thank you for giving me this opportunity and for all your help and support during these years. Every interaction with you has taught me a lot, thank you very much for your ideas and motivation in difficult moments, you have helped me to grow as a researcher and as a person. Many thanks also to Nicholas Ayache for allowing me to be part of this fabulous team, allowing me to enjoy such an inspiring research environment in the wonderful Côte d'Azur.

I am very grateful to Alistar Young and to Boudewijn Lelieveldt for reviewing this manuscript and providing constructive feedback and insights. Sincere thanks to Frederik Barkhof and to Juan Domingo Gispert for accepting to be members of my jury and their helpful and inspiring comments. Thanks also to Xavier Pennec and to Irene Vignon-Clementel for your valuable inputs in the *comité de suivi*. Thank you all for your valuable time.

Many thanks to all the Epione team and the people I have met at INRIA, it has been a pleasure to share meals, coffee breaks and the retreats at Auron with all of you. Thanks for the beach volley afternoons, the *futbolin* games, the beers and the hikes! Thanks to Marco M. for the chess and football lessons, to Zihao, for letting us see Julian cry with laughter, to Yann T. for your patience and kindness even when I speak French, to Selma for your facility to make me laugh and your competitiveness in the beach volley afternoons, to Pawel for your joy in the *futbolin* games, to Raphaël and Julian for showing us the best hiking routes, to Benoît for complaining together, to Marta for being the best Bordeaux guide. And especially, to Sara, for your advice, energy and for those games of 'cards against humanity', to Santiago, for your generosity, your contagious happiness, and your harepas!, and of course to Luigi and Clément, I couldn't have had better office mates, I am grateful to have shared this experience with you. Luigi, thanks for always teaching me something new, for solving any problem, and thanks for your limoncellos. Clément, there is only one way to summarize it: Switerland-Serbia 2018, that day I knew we would live great things. *Caballeros*, it will be hard to be in an office without you! And again, thanks to all the Epione memebers for making INRIA such a nice place, Nicolas G, Shuman, Bastien, Tania, Nicolas C. , Yann F., Etrit, Irene, Yingyu, Wen, Florent, Gaëtan, Hind, Buntheng, Paul, Dimitri, Hari and all the others. And thanks to Isabelle for your help in the navigation of INRIA's burocracy.

To my friends, for their invaluable support and for being there despite my tendency to disappear. Thank you for making me feel close to home even when I was far away.

Simone, thank you for being by my side every day and making me smile even in the most difficult moments, thank you for your constant support and for understanding me even when I don't understand myself. I feel very lucky to grow up together with you, thank you.

And to my family, my parents and my sister, thank you for all the support, help and love throughout my life. This thesis is dedicated to you,

Jaume

Financial Support

This work has been supported by the French government, through the 3IA Côte d'Azur Investments in the Future project managed by the National Research Agency (ANR) with the reference number ANR-19-P3IA-0002, and by the ANR JCJC project Fed-BioMed 19-CE45-0006-01. The project was also supported by the Inria Sophia Antipolis - Méditerranée, "NEF" computation cluster and by the Spanish Ministry of Science, Innovation and Universities under the Retos I+D Programme (RTI2018-101193-B-I00) and the Maria de Maeztu Units of Excellence Programme (MDM-2015-0502).

Contents

Glossary:

τ: Arterial compliance.

σ_0: Contractility.

C_1: Stiffness.

R_0: Left ventricle radius.

R_p: Peripheral resistance.

AF: Atrial fibrillation.

BSA: Body surface area.

CO: Cardiac output.

DBP: Diastolic blood pressure.

EDV: End-diastolic volume.

EF: Ejection Fraction.

ESV: End-systolic volume.

GM: Grey matter.

IUP: Iteratively updated priors.

MBP: Mean blood pressure.

SBP: Systolic blood pressure.

SV: Stroke volume.

WM: White matter.

WMHs: White matter hyperintensities.

1 Introduction

Contents

1.1 Clinical context

In 2018, 48 million people worldwide suffered from dementia with an estimated cost of 819$ billion per year, making dementia one of the leading causes of death and disability. Due to the global ageing of the population, the prevalence of dementia is expected to triple by 2050 [Wolters, 2018; Nichols, 2019]. The growing burden of dementia imposes an increasing level of stress on the families and over the healthcare system, thus curative and preventive measures are urgently needed. Dementia is associated with a broad range of neurological disorders, Alzheimer's disease (AD) being the most common [Dichgans, 2017]. AD is a neurodegenerative disease in which subclinical alterations in the brain take place decades before the occurrence of clinical symptoms and cognitive decline [Jack, 2013]. During the presymptomatic phase, abnormal deposition of extracellular beta-amyloid ($A\beta$) as amyloid plaques and intracellular tau as tangles are formed. Amyloid plaques interfere with neuron synapses, while tau tangles block the transport of nutrients inside the neurons, impairing proper functioning and ultimately leading to cell death [Scheltens, 2016]. So far clinical trials have failed to develop a disease-modifying therapy in patients diagnosed with dementia [Wolters, 2018], thereby promoting the focus towards the presymptomatic phase of the disease. Hence, two types of biomarkers are currently needed: 1) biomarkers for a cost-effective screening phase that help to identify individuals at risk, and/or at early stages of the disease; and 2) biomarkers specific of late disease stages to monitor disease evolution.

In this context, studies such as the Alzheimer's disease neuroimaging initiative (ADNI) [Mueller, 2005], have been established in order to identify useful biomarkers. The core biomarkers defining AD are related to tau and amyloid aggregation [Jack, 2013]. These

biomarkers can be obtained from biofluids, such as cerebrospinal fluid (CSF), or from positron-emission tomography (PET) images. Both methods provide similar information accurately reflecting AD-specific pathogenic events [Olsson, 2016; Hansson, 2018; Mattsson, 2014]. Moreover, other biomarkers non-specific of AD have been identified related to neurodegeneration and cognitive decline, such as brain morphological changes or reduced glucose metabolic activity [Jack, 2018]. However, these biomarkers reflect late disease stages. Concerning early onset biomarkers, only genetic risk factors have been identified [Broce, 2019; Wolters, 2018]. This is a major inconvenience for clinical routine practice and for clinical trials, since selecting participants based on relatively rare genetic variants could render results less applicable to the large population at risk.

Nevertheless, there is increased evidence from clinical and pathological studies that AD often co-occurs with the presence of a vascular component that contributes to accelerate cognitive decline [Kapasi, 2017]. Microinfarcts, microbleeds or strokes among other cerebrovascular events have been associated to neurodegeneration [Veldsman, 2020], and the resulting cognitive effects are generally defined with the term vascular cognitive impairment (VCI) [Dichgans, 2017]. Moreover, multiple epidemiological and general population studies, such as the UK Biobank [Sudlow, 2015], the Framingham Study [Feinleib, 1975] or the Rotterdam study [Hofman, 2015], have identified several risk factors for dementia, such as midlife hypertension, obesity, smoking or diabetes, which are shared with cardiovascular diseases, such as heart failure (HF) [Doehner, 2018] or atrial fibrillation (AF) [Diener, 2019; Sepehri Shamloo, 2020]. Interestingly, a number of the dementia-associated cardiovascular risk factors are potentially modifiable and are already targeted to prevent cardiovascular diseases in developed countries. This could be related to the fact that in industrialised countries the prevalence of dementia has reduced by about 20% per decade since 1970s [Satizabal, 2016; Matthews, 2016; Schrijvers, 2012]. Nevertheless, this will not be enough to compensate for the rapid ageing of the population. Clinical evidence suggests that abnormal alterations in cardiovascular risk factors and vascular biomarkers may be detectable before neurodegenerative markers, such as brain morphological changes [Friedman, 2014; Lane, 2019], as well as abnormal biomarkers specific of AD [Iturria-Medina, 2016]. According to these findings, the disease evolution timeline may manifest early vascular anomalies prior to brain morphological alterations (Figure 1.1) [Sweeney, 2018]. However, clinical trials aimed at reducing the incidence of dementia based on cardiovascular risk factors have not shown positive results [Wolters, 2018]. These outcomes illustrate that better than assess effects on cognition, we need to understand the underlying physiological pathways connecting cardiovascular diseases and cognitive impairment. This could help to slow down cognitive decline and delay or prevent the onset of dementia.

Neurodegeneration has been linked to microvasculature dysfunction and small vessel disease (SVD), which denotes common abnormalities associated to microvessel damages seen on brain imaging [Wardlaw, 2019], such as white-matter hyperintensities (WMHs)

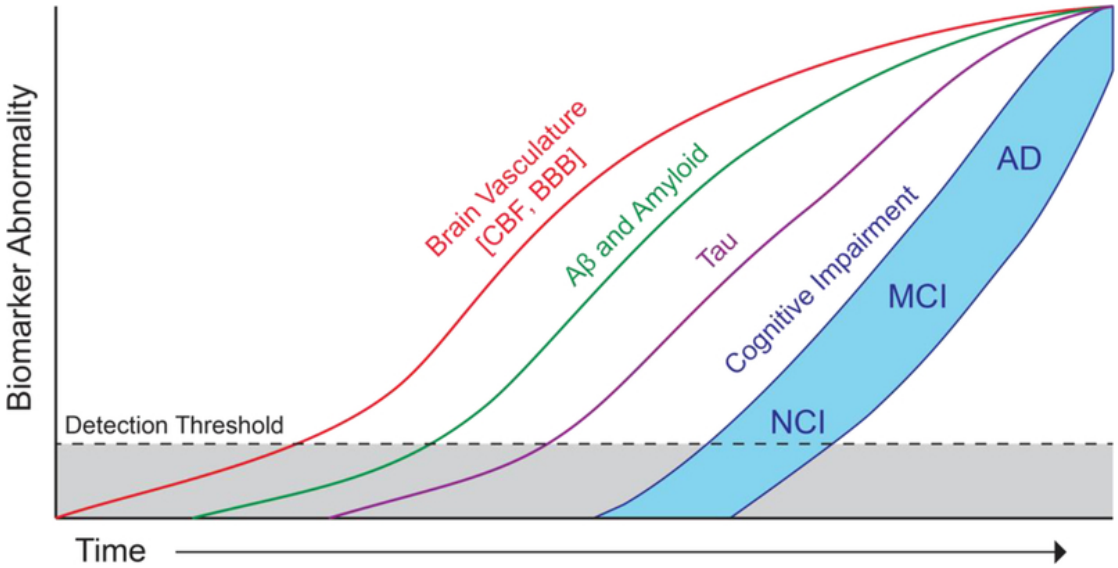

Fig. 1.1.: Hypothetical model of Alzheimer's disease biomarkers including brain vasculature changes. Early cerebral blood flow (CBF) and brain-blood-barrier (BBB) dysfunction may contribute to initial stages of Alzheimer's disease progression. Mainly from no cognitive impairment (NCI) to mild-cognitive impairment (MCI). Reprint with authorization from [Sweeney, 2018].

[Wardlaw, 2015]. In the case of WMHs, these abnormalities have been associated to cognitive decline [Debette, 2010] and abnormal blood pressure [Gupta, 2018; Moroni, 2018]. While the exact etiology of WMHs is unknown, it is believed that they may have a vascular origin and have been linked to capillary transient time heterogeneity (CTH), which takes place when there is a mismatch between capillary flow and oxygen delivery [Østergaard, 2013]. CTH is associated to endothelial dysfunction, which hampers cerebrovascular reactivity, affecting the ability of arterioles and capillaries to modify their radii in response to neuronal activity and direct blood flow where needed. Hypotheses behind the source of microvascular damage point to the increase of arterial stiffness with age and/or pathologies such as hypertension [ORourke, 2007]. This increased stiffness decreases the attenuation of pressure oscillations. Thus, the capillary bed receives a pulsatile flow instead of a steady-flow. This may increase stress on the capillary endothelial wall and trigger neuronal damage [Stone, 2015; Toth, 2017]. Moreover, carotid arterial stiffness is negatively associated with cerebral blood flow in older adults [Tomoto, 2021]. In turn, cerebral hypoperfusion has been associated with accelerated cognitive decline and increased risk of dementia in the general population [Wolters, 2017]. Impaired blood flow has also been associated with increased levels of neuronal oxidative stress, resulting in cerebral inflammation, that can also lead to vascular damage [Iadecola, 2013; Wolters, 2018]. Moreover, the pulsatility in cerebral arteries is thought to be involved in the brain waste clearance process through the regulation of CSF circulation and the flow in perivascular spaces of the brain [Wardlaw, 2020]. However, this process is not yet well understood and is currently focus of active research [Agarwal, 2021; Mestre, 2020].

At the same time, the brain can regulate the cardiac function altering heart's contractility or heart rate depending on its perfusion needs. However, stiffening of the arteries affects cardiovascular coupling; the decreased elasticity of the main arteries rises the systolic pressure, which in turn forces the heart to increase its contractility or heart rate in order to supply the same amount of blood. Therefore, a prolonged hypertension may result in cardiac remodelling processes such as left-ventricular hypertrophy, which has been associated to a lower brain volume [Patel, 2017] and a higher burden of WMHs [Ryu, 2014]. Moreover, reduced cardiac output and brain blood flow were also associated to greater WMHs burden [Jefferson, 2009; Bahrani, 2017]. Hence, impaired cardiac function may result in impaired brain perfusion, and may explain the relationship between heart failure (HF) [Doehner, 2018] or atrial fibrillation (AF) [Diener, 2019; Sepehri Shamloo, 2020] with cognitive decline. However, due to the tight relationship between heart and brain through numerous physiological feedback mechanisms, it is difficult to elucidate which mechanism initiates the pathological cycle. Moreover, the lack of datasets combining joint heart and brain information in neurodegenerative disease hampers their joint study.

This context motivated recent initiatives such as the Heart-Brain study [Hooghiemstra, 2017], in which researchers seek to quantify the haemodynamic status of the heart and of the brain through image-derived biomarkers, assessing their contributions to vascular cognitive impairment by means of statistical association analysis. In this study it has been reported that a substantial number of patients with HF and carotid occlusive disease (COD) present cognitive impairment [Hooghiemstra, 2019]. However, in opposition to [Wolters, 2017], an association between reduced cerebral blood flow (CBF) and decreased cognitive function has not been found [Leeuwis, 2020].

1.2 Methodological context

As introduced in the previous section, epidemiological datasets contain multimodal patient-specific data, and allowed to identify several risk factors shared between cardiovascular diseases and dementia. Moreover, these datasets open the door to study diverse phenotypes, based for example on imaging, genomics and demographic data. Therefore, a number of hypotheses can be tested, such as the association between cardiovascular risk factors and brain imaging features [Cox, 2019] or the association between lifestyle and genetic risk factors with dementia [Lourida, 2019]. Most of these hypotheses are tested through standard statistical tools such as univariate or multivariate regression analysis and survival analysis models.

There are two main drawbacks associated to the current analyses: 1) the heterogeneity of the epidemiological datasets limits the number of subjects diagnosed with a neurodegen-

erative disease and disease-specific biomarkers, such as PET imaging or CSF measures are scarce; 2) while statistical association analysis allows to easily formulate and test association hypotheses, it offers a limited interpretation of the complex relationship between organs.

Hence, we need computational tools making full use of the large-scale biological information available in epidemiological datasets to obtain models that allow us to extrapolate the learned associations from these datasets to clinical and disease specific cohorts. To achieve that, we need deeper physiological and biomechanical insights than the ones obtained from pure association analysis. In this context, mechanistic and biophysical models represent an opportunity to introduce physiological knowledge in the links between the available measurements.

Biophysical models allow to estimate in-silico biomarkers representing physiological properties that cannot be measured in-vivo, such as the contractility or the stiffness of the heart fibres. These models allow for example to describe the brain vasculature, and to quantify physiological aspects such as blood flow auto-regulation effects in the brain [Acosta, 2018], or the simulation of the whole-body circulation with detailed compartmental components [Blanco, 2015]. Recently, mechanistic approaches have been used to study the effect of atrial fibrillation (AF) in brain perfusion and determined that the loss of periodicity in the AF beat-series may lead to a higher occurrence of hypoperfuse and hypertense events in the distal regions of the cerebrovascular circulation (arterioles and capillaries) [Scarsoglio, 2017]. Additionally, Aghilinejad et al. [Aghilinejad, 2020] determined that the stiffening of the aorta relative to the carotid arteries increased the pulsatility of blood flow in the brain vasculature, leading to increased microvascular damage. However, although these approaches offer a high level of interpretability, their personalisation is not trivial.

Personalising a cardiovascular model for a given subject implies solving an inverse problem to estimate the model parameters such that the generated simulations are as close as possible to the available clinical data. This problem is usually severely ill-posed and requires large data samples and arrays of measurements to opportunely tune their parameters. Several approaches have been proposed for cardiac-related inverse problems. When sequential data is available, it is common to rely on filtering methods such as the unscented Kalman filter (UKF) [Pant, 2017], that correct the model based on the discrepancy between upcoming input data and model's prediction. Other options involve data-driven approaches such as reinforcement learning [Neumann, 2016], gradient-based solutions based on the adjoint method [Delingette, 2012] or gradient-free approaches such as genetic algorithms [Khalil, 2006]. Moreover, in the case of high-order biophysical models, such as 3D models, these methods are computationally expensive. Thus, multi-fidelity approaches, based on evolutionary algorithms [Molléro, 2017] or

filtering methods [Pant, 2014], have been used to combine the computational efficiency of reduced-order models with the accuracy of higher-order models.

Nevertheless, personalisation is commonly carried out at most in tens or a few hundreds of subjects [Molléro, 2018]. Hence, those approaches are typically oriented towards obtaining solutions that mimic the observed clinical features but they do not prioritise obtaining homogeneous solutions in groups of subjects. Therefore, a large variability between solutions in similar subjects can be found. This hampers the significance and conclusions drawn from statistical association analyses that include the estimated cardiac model parameters.

Thus, approaches allowing to bridge the gap between statistical association analysis and personalised mechanistic models have the potential to give insights impossible to obtain through standard statistical analysis, thanks to the estimation of non-measurable physiological properties. In turn, the mechanistic constraints introduced in these models can help to extrapolate the knowledge learned in large-scale population studies to pathological studies where cardiac data is limited but there is a rich set of disease-specific biomarkers.

1.3 Objectives and organisation of the thesis

In this thesis we explore the use of personalised biophysical models as a method to introduce prior knowledge of the cardiac function in the analysis of heart-brain interactions through their internal dynamics. We hypothesise that these models could allow to obtain early biomarkers with the potential to identify individuals at risk of dementia. In particular, we investigate the following research questions:

- How can we obtain comparable population-wise estimations of cardiovascular model parameters, and use them to analyse the heart-brain interaction?
- How can we study the interplay between cardiac function and brain imaging markers in disease-specific datasets with limited cardiac information?
- What is the potential of biophysical model parameters as non-specific biomarkers to identify individuals at risk of dementia?

The thesis is organised as follows:

In **Chapter 2**, we give an introduction of the heart electromechanical behaviour, the brain anatomy and their physiological relationship, relating the cardiac physiological properties to the model parameters used in our work.

In **Chapter 3**, we investigate how to incorporate prior knowledge encoded in a biophysical model to study the relationships between brain and cardiac function. We tackle the problem of obtaining a population-wise homogeneous solution in an ill-posed setting and how the use of external information, such as brain imaging data, aids to simplify the problem. Moreover, we demonstrate the potential of our approach by assessing differences in a pathological subgroup diagnosed with atrial fibrillation (AF).

In **Chapter 4**, we present a framework that allows to infer the parameters of a biophysical cardiovascular model from incomplete brain-specific datasets, using the heart-brain dynamics learned in a large-scale complete cohort, the UK Biobank. The parameters of the cardiovascular model are obtained using the personalisation approach presented in Chapter 3. We show how the developed imputation framework allows to accurately impute the missing information and simulate the evolution of the model parameters as brain features change.

In **Chapter 5**, we explore the potential of the biophysical model parameters as biomarkers to identify population at risk of dementia. Leveraging on the tools described in Chapter 3 and 4, we can infer the missing cardiac information in a longitudinal study focused on Alzheimer's disease, ADNI. Next, we use disease progression modelling to estimate the disease stage of every subject based on the evolution of their biomarkers. This allows to study the role of cardiac function in relation to brain morphological changes and cognitive scores during disease progression. The obtained results show that abnormal alterations in cardiovascular biomarkers take place before alterations in other biomarkers associated to neurodegeneration. The results are in-line with hypothetical disease evolution timelines proposed previously [Sweeney, 2018].

In **Chapter 6**, potential future work and perspectives are discussed.

In **Appendix**, we present ongoing work aimed to study the influence of cardiac function in the cerebrospinal fluid (CSF) flow. We introduce our implementation of a computational fluid dynamics (CFD) solver based on the lattice Boltzmann method (LBM), and preliminary results based on the processing of quantitative flow images of CSF and carotid blood flow.

1.4 Publications and software packages

The described contributions led to the following peer-reviewed publications:

Journal articles

- Banus J., Lorenzi M., Camara O., Sermesant M. Biophysics-based Statistical Learning: Application to Heart and Brain Interactions. In MedIA (*in reviews*)

- Banus J., Sermesant M., Camara O., Lorenzi M. Alzheimer's Disease Progression Model including Heart & Brain (*in preparation*)

Conference articles

- Banus J., Sermesant M., Camara O., Lorenzi M. (2020) Joint Data Imputation and Mechanistic Modelling for Simulating Heart-Brain Interactions in Incomplete Datasets. In: Martel A.L. et al. (eds) Medical Image Computing and Computer Assisted Intervention – MICCAI 2020. MICCAI 2020.

- Yang Y., Gillon S., Banus J., Moceri P., Sermesant M. (2020) Non-invasive Pressure Estimation in Patients with Pulmonary Arterial Hypertension: Data-Driven or Model-Based?. In: Pop M. et al. (eds) Statistical Atlases and Computational Models of the Heart. Multi-Sequence CMR Segmentation, CRT-EPiggy and LV Full Quantification Challenges. STACOM 2019.

- Banus J., Lorenzi M., Camara O., Sermesant M. (2019) Large Scale Cardiovascular Model Personalisation for Mechanistic Analysis of Heart and Brain Interactions. In: Coudière Y., Ozenne V., Vigmond E., Zemzemi N. (eds) Functional Imaging and Modeling of the Heart. FIMH 2019.

Software packages

- Imputation framework: https://gitlab.inria.fr/epione/hdcob.git

1.5 Data availability

UK Biobank data are available through a procedure described at `http://www.ukbiobank.ac.uk/using-the-resource/`. ADNI data are publicly available at `http://adni.loni.`

usc.edu/. The exact number of samples currently available in both datasets may differ slightly from those described in this thesis.

1.6 Code availability

The source code for the imputation model is publicly available at https://gitlab.inria.fr/epione/hdcob/, and for the disease progression model at https://gitlab.inria.fr/epione/GP_progression_model_V2/.

2 Heart & Brain: Physiological Relationship

Contents

A deep in-detail physiological analysis of both organs is out of the scope of this thesis. However, we would like to provide an overview of the most important concepts and knowledge required to understand the basis of the heart-brain relationship, the role of the parameters of the personalised biophysical model, and the conclusions drawn from the results obtained at the different chapters. Most information and concepts illustrated in this chapter come from cardiovascular physiology [Herring, 2018; Sevre, 2015; Prabhakar, 2020; Pappano, 2013] and neuroanatomy books [Vanderah, 2015]. However, papers tackling controversial and ongoing research topics are cited when needed.

2.1 The Heart

The heart is a viscoelastic muscular organ whose main function is to periodically pump the blood throughout the circulatory system. It can be divided in two pumping systems in series, the right and the left side, each with two separate chambers, a ventricle and an atrium. The left side receives oxygenated blood from the lungs and pumps it to the rest of the body (**systemic circulation**). The right side receives deoxygenated blood and pumps it to the lungs, where it exchanges CO_2 for O_2 (**pulmonary circulation**).

The heart is made of three tissue layers, the epicardium, myocardium and endocardium. The endocardium is the layer in the inner surface of the chambers, it is comprised mainly of endothelial cells over connective tissue. The epicardium is the outermost layer, it is a visceral layer made of mesothelial cells, adipose and connective tissue, it cushions the heart and nerves and blood vessels are located in it. At the roots of the great vessels

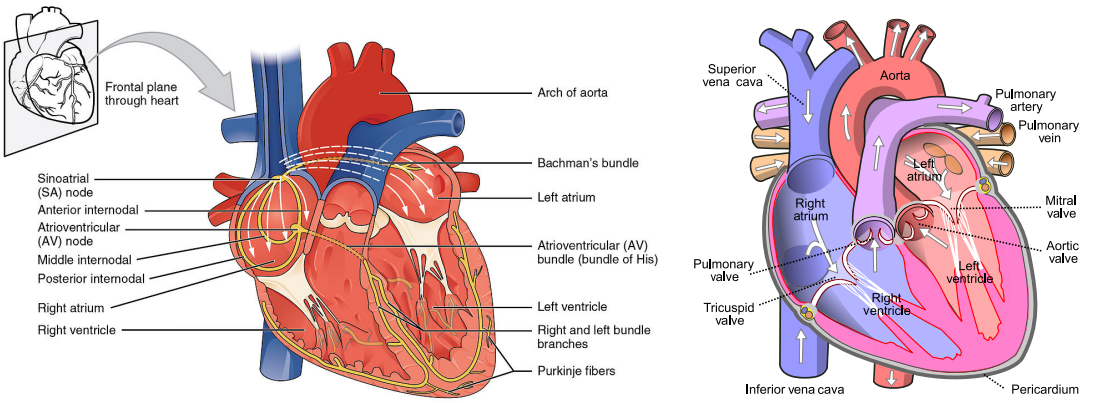

(a) Conduction system

(b) Anatomy and flow direction

Fig. 2.1.: Diagrams of the human heart a) Heart conduction system, represented in yellow. It includes the sinoatrial node (SA),the atrioventricular (AV) node and Purkinje fibres. The white arrows indicate the propagation of the depolarization induced by the SA; image from https://commons.wikimedia.org/ b) Main aspects of the heart anatomy, the white arrows indicate the blood flow direction; image from https://commons.wikimedia.org/. Details are available in the text.

it reflects back and continuous to form the pericardial sac, filled with pericardial fluid that prevents friction during heart contractions. In between, we find the myocardium, it is a muscle layer composed of cardiomyocytes that enables the contraction of the heart. It is the thickest layer, being thicker in the ventricles than in the atria, due to the higher pressures generated in the ventricles. The myocytes of the ventricles are organised primarily in a circumferential orientation, originating from the base of the heart (near the aortic orifice) and sweeping towards the apex, they gradually undergo a 180-degree change where fibres vary transmurally from approximately -70 in the epicardium to +80 degrees in the endocardium. When they contract they twist and shorten longitudinally, with the base descending towards the apex. Moreover, the heart has a system of valves structurally designed to allow flow in only one direction, the valves passively open and close in response to the direction of the pressure gradient across them. There are two types of valves in the heart: the atrioventricular valves that regulate the flow from the atrium to the ventricles, and the semilunar valves, that regulate the flow from the ventricles to the arteries.

The contraction of the myocardium is caused by a multi-scale physical phenomena, known as **excitation-contraction coupling** process whose basic unit is the sarcomere. The sarcomeres are composed of long, fibrous proteins. The two main proteins are the myosin and the actin, which form the thick and thin filaments respectively. The myosin head binds to the actin active sites forming a *cross-bridge*, this allows the myosin head to 'pull' the actin along its length, this generates a *power stroke*, forcing the actin to slide along the myosin filament. The myosin-actin interactions are mediated mainly by calcium and ATP. The phosphorylation of ATP gives the energy to the myosin heads, and the concentration of calcium determines the number of active actin binding sites. In our

work, the mechanistic modelling of the excitation-contraction coupling is done using the Bestel-Clement-Sorine (BCS) model. An important parameter of the model is σ_0, which represents the maximum contraction strength generated by the sarcomere. The model is described in detail in Section 3.3.1.1.

The cascade of events inducing the calcium release inside the cardiomyocytes is initiated by a membrane depolarization that triggers an action potential in the cell, which is dependent on the electrochemical gradients of sodium, potassium and calcium. However, as opposite to the skeletal muscle, the cardiac cells do not need an external stimulus. Certain cardiomyocytes have the ability to fire action potential spontaneously (**automaticity**) at a regular frequency (**rhythmicity**). They act like pacemakers controlling the heartbeat frequency. There are three regions that have this ability: the sinoatrial node (SA), the atrioventricular (AV) node and the bundle of his/Purkinje. Usually, the SA node controls the heartbeat, and the AV creates a delay between the atrium contraction and the ventricle to ensure proper ventricular filling. However, if the SA node fails the other nodes can take over. The action potential generated in these nodes propagates through the gap junctions that exist in the borders between myocardial fibres, in contact with each other longitudinally. Thus, the cardiac impulses progress more rapidly in a direction parallel to the long axes of the fibres. The cardiac depolarisation is modelled in our work using Equation 3.11, which links the fraction of the ventricle that is depolarised to the BCS model, by determinig the relaxation and contraction rates of the sarcomere.

The sequence of electrical changes, pressures, and mechanical events within the heart during each beat is known as the cardiac cycle. Each cycle has two periods, diastole and systole. During diastole the heart muscle relaxes and refills with blood, then during systole the heart ventricles contract and blood is pumped towards the arteries. Moreover, each cycle can be divided in four stages based on the positions of the inlet and outlet valves:

- Ventricular filling: The AV valves are open, the ventricles are in diastole, and initially also the atria. Thus, blood flows passively from the superior and inferior vena cava through the relaxed atria and into the ventricles. At the end of the phase there is the atrial systole, *atrial kick*, which pumps extra blood into the ventricle. The volume of blood in the ventricle at the end of this phase is called end-diastolic volume (EDV).

- Isovolumetric contraction: The ventricle starts to contract, as soon as the pressure rises above the atrial pressure the AV valves are closed and ventricular pressure rises quickly. The maximum rate of rise of pressure dP/dt is often used as an index of contractility.

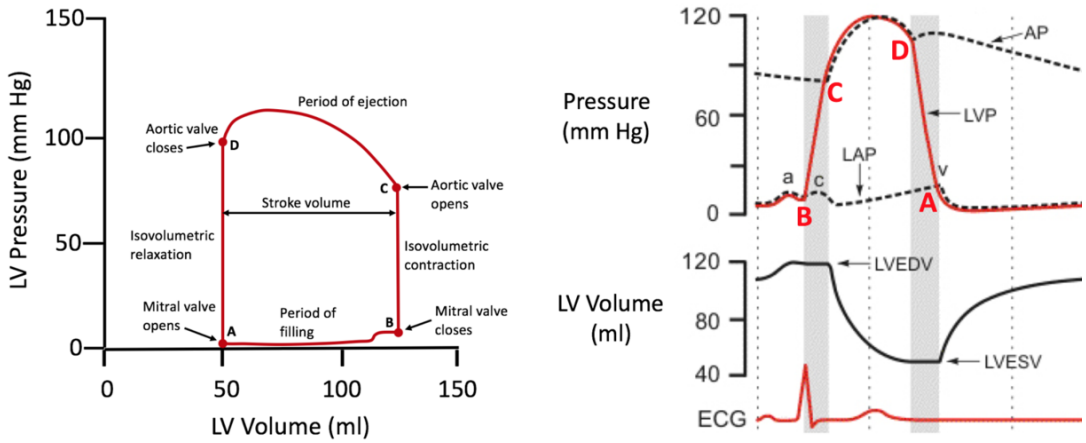

(a) Pressure-volume loop

(b) Wiggers diagram

Fig. 2.2.: a) Pressure-volume (PV) loop: it represents the changes in left ventricular pressure and volume throughout the cardiac cycle. Diastolic filling starts at A when the mitral valve opens and terminates at B, when the mitral valve closes. With isovolumetric contraction there is a steep rise in pressure and no change in ventricular volume. At C, the aortic valve opens, and ejection begins. During the first phase of ejection, rapid ejection, there is a continued but less steep increase in ventricular pressure. This is followed by reduced ejection and a small decrease in ventricular pressure. When it falls below the aortic pressure the aortic valve closes, D, and isovolumetric relaxation takes place, characterized by a sharp drop in pressure and no change in volume. The mitral valve opens again to complete one cardiac cycle. b) Wiggers diagram: in this diagram the cardiac cycle is often represented as beginning midway through diastole, the top row shows the pressure temporal profile for the left ventricle (LVP), the left atrium (LAP) and the aorta (AP). The bottom row, shows the evolution of the left ventricle volume and the ECG signal; LVEDV, left ventricle end-diastolic volume; LVESV, left ventricle end-systolic volume. Images from https://www.cvphysiology.com/

- Ventricular ejection: When ventricular pressure becomes higher than the atrial pressure (**afterload**), the semilunar valves are pushed open and the blood is ejected into the arteries. Initially the blood is ejected faster than it can drain away through the peripheral vessels, (*rapid ejection phase*), and most of the blood is accommodated temporally in the distended elastic arteries. Later, the ejection rate slows down and pressure begins to fall, when if falls below the arterial pressure a brief backflow closes the valve, the closure creates a notch in the arterial pressure trace, called the *incisura*. For the rest of the cycle the arterial pressure decays gradually towards its diastolic minimum. The ejected volume is known as stroke volume (SV), and the residual volume in the ventricle is the end-systolic volume (ESV). The proportion, SV/EDV, is the ejection fraction (EF).

- Isovolumetric relaxation: The relaxing myocardium causes the ventricular pressure to fall rapidly, when it falls below atrial pressure the pressure gradient opens the AV valves, and the ventricular filling begins.

In our work, Equation 3.7 is used to model the phases of the cardiac cycle by linking the ventricular blood flow to the atrial, ventricular and arterial pressures.

The examination of the relationship between pressure and volume in the heart during each cardiac cycle reflects the properties and conditions of the myocardial cells and provides a haemodynamic characterisation of the heart. For example, during the ventricular filling the pressure increases due to the stretching of the ventricle induced by the blood volume. Overall, the resulting relationship between pressure and volume reflects the length-tension relationship of the ventricular cells. As can be seen in Figure 2.2b, from A to B the pressure-volume curve in diastole is initially quite flat (compliant), indicating that large increases in volume can be accommodated with only small rises in pressure. The ventricle becomes much less distensible with greater filling, as evidenced by the sharp rise of the diastolic curve at large intraventricular volumes. This resistance to stretch of the myocardium at high filling pressures serves as a safety factor protecting against overloading of the heart in diastole. The stretching of the sarcomeres at the end of the filling determines the **preload**. In our model this property is linked to the parameter C_1, which determines the stiffness of the cardiac fibres, as can be seen in Equation 3.6.

An important indicator on how the heart is meeting the body's demands is the cardiac output (CO), which measures the volume of blood in a given minute. It is obtained multiplying the stroke volume by the heart rate (HR), i.e. the number of heartbeats per minute (bpm). In a normal individual at rest CO ranges between 4 and 6 L/min. However, in certain situations the hart may need to adapt this quantity. There are three main factors that determine CO: 1) myocardial contractility (i.e., excitation-contraction coupling processes); 2) preload; and 3) afterload. These three factors determine the strength and velocity of the myocardial contraction. The CO is regulated mainly by two systems:

- Intrinsic cardiac regulation: Based on the **Frank–Starling** mechanism. As we said, the stretching of the sarcomeres (preload) varies based on the volume of blood flowing into the ventricle, known as **venous return**. This stretching influences the ability of the actin and myosin to form cross-bridges. Therefore, up to a certain range the contractility increases as the EDV increase, but after a given stretching it plateaus. It should also be noted that the "stretch" of the atrial wall can directly increase the rate of the SA node by 10–20 %; this also aids in the amount of blood that will ultimately be pumped per minute by the heart.

- Autonomous nervous system: Heart rate and cardiac contractility can be regulated via reflex mechanisms that involve baroreceptors and chemoreceptors that modulate the sympathetic and parasympathetic activity of the nervous system. Substantial

groupings of such baroreceptors can be found at the arch of the aorta and on the internal carotid arteries (*carotid sinus*). Those specifically located in the carotid help to maintain normal blood pressure in the brain, whereas those located in the area of the ascending arch of the aorta help to govern general systemic blood pressure. Baroreceptors are sensitive to the stretching of the arterial walls, which will results in changes of the firing rate of these receptors. Chemoreceptors monitor the chemical composition of blood, and are located close to the baroreceptors in small structures known as the carotid and aortic bodies. The chemoreceptors within these bodies detect changes in blood levels of O_2 , CO_2 , and H^+. In order to detect hypoxia (low availability of O_2), acidosis (increased blood concentrations of H^+), and/or hypercapnia (high concentrations of CO_2). In response to these receptors the central nervous system regulates the vascular tone, the release of hormones, and/or the respiratory function.

2.2 Vascular system

The blood is a non-Newtonian fluid whose viscosity depends on the haematocrit, i.e: the proportion of red cells, an increase in haematocrit increases the internal friction of blood and hence, viscosity. Nevertheless, the viscosity falls in microvessels, facilitating microvascular perfusion. The viscosity drops as flow and shear rate increase, this is called shear thinning, in blood it is attributed to the deformation and lining up of red cells along the laminar flow lines. This effect is important because it greatly reduces microvascular resistance, and therefore the arterial pressure needed to perfuse the microcirculation. The blood is distributed throughout the entire body by the vascular system, a schematic representation is available in Figure 2.3. The blood vessels can be divided in different segments based on their physiological properties:

- Main arteries: such as the aorta or the carotids, are very elastic and present a pulsatile flow. The elasticity allows them to maintain the blood pressure throughout the body. When the aorta receives the blood from the heart, it recoils and stores mechanical energy, once the ejection phase is over the distention is used to push the blood during the diastole, this is known as the **Windkessel effect**. Around 67%–80% of the stroke volume is temporarily stored in the elastic arteries during systole, while 20%–33% runs off through the peripheral resistance.

- The arterioles: are relatively rigid, its function is to impose a steady flow by means of a higher frictional loss. They represent most of the vascular resistance to blood flow and is where the biggest pressure drop occurs, as can be seen in Figure 2.4. Changes in the total peripheral resistance (TPR) are mostly due to changes in them. In fact, they can regulate the percentage of the total blood flow to individual organs.

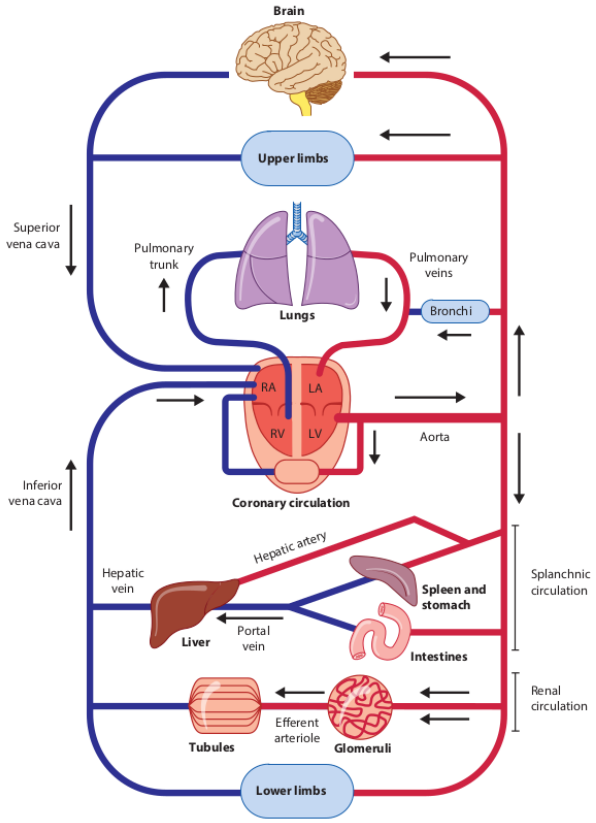

Fig. 2.3.: Schematic representation of the vascular tree: we can see how most of the organs are arranged in parallel with respect to the aorta. However, some specific cases like the liver, are arranged in-series with other organs. This type of arrangement is called a portal system, and is used to transport substances from one site to another. Reprint with authorisation from [Herring, 2018].

However, individual arteriole do not usually remain relaxed or contracted for long; its muscle tone changes constantly (**vasomotion**), and in some tissues vasomotion has a regular rhythm.

- The capillaries: are the smallest and most numerous blood vessel resulting from the continuous branching of the vascular tree, they have a very thin wall composed of only an endothelial cell and the supporting basement membrane. The circulation broadening slows down the blood, this slow velocity in capillaries is key for the nutrients and gas exchange. The forces that drive the movement of fluid into and out of the capillaries, **Starling forces**, depend on the balance of hydrostatic and osmotic pressures. The hydrostatic pressure tends to push the fluid out of the capillaries, and inversely for the osmotic pressure. Hence, if the hydrostatic pressure is higher than the osmotic there is a *filtration* of fluid towards the interstitial space, while the opposite process, *absorption*, takes place when osmotic pressure is dominant. Usually both process are in equilibrium along the capillaries, i.e: there is no net flow of filtration. However, if there is a net flow it resolves into an

edema, which can be caused by changes in the hydrostatic pressure due to cardiac dysfunction.

- Venules and veins: On its return to the heart from the capillaries, blood passes through venules and then through veins of increasing size, reaching a diameter similar to the arteries but half as thick. Veins support much lower pressures, are very compliant and present a steady flow. The veins acts as a volume reservoir, and can accommodate high increases in blood volume. Contractions of the skeletal muscles aid in returning blood to the heart. The increased blood flow due to the contractions is only towards the heart due to the valves that are present within the veins. The venous pressure influences the end-diastolic volume, which as we saw in the previous section, increases stroke volume and cardiac output according to Frank-Starling's law.

The flow of any liquid, such as the blood, can be described by the Navier-Stokes equations, which are based on the conservation of momentum (Newton's second law), energy and mass. However, they result in a non-linear system without a general solution, except under certain assumptions and simplifications. For example, if we consider an incompressible fluid and a steady-flow along a rigid tube driven by a constant pressure, the flow $Q[l/min]$ is proportional to the pressure drop between the inlet and outlet $\Delta P = P_2 - P_1[mmHg]$, this proportionality will depend on how difficult it is for the liquid to flow in the tube, the resistance to flow $R[(mmHg \times min)/l]$, and can be expressed as: $Q = \Delta P/R$. This is called **Darcy's law** of flow, and is equivalent to **Ohm's law** for the electrical flow. Hence, the bigger the resistance, the bigger the pressure needed to drive the same flow. This equation can be applied to a network of vessels, such as the vascular bed of an organ or the entire systemic circulation to obtain a general approximation. Actually, assuming axisymmetry, the flow through a cylindrical tube can be estimated by means of the Poiseuille equation, $Q = \frac{\pi \Delta P r^4}{8 \mu L}$, where $r[m]$ is the radius, $L[m]$ the length, and $\mu[kg/(m\ s)]$ the dynamic viscosity of the fluid. It is important to note that according to this equation a small change in vessel radius will have a very large influence on its resistance to flow. From these equations we can observe two points: 1) flow will only occur when a pressure difference exists, and the flow will be directed from high to lower pressure regions; 2) the diameter of the vessels is critical to the total resistance to flow. Hence, it is not surprising that arterial blood pressure is principally regulated by controlling the radii of the vessels within a given tissue or organ system.

The analogy between Darcy's and Ohm's law, can be extended, referring to it more generally of the **electronic–hydraulic analogy**. By using it, the pressure difference is equivalent to the voltage difference, the blood flow to the current flow, and the compliance of the vessels is equivalent to a capacitor. Indeed, the Windkessel effect that takes place in the main arteries can be emulated by an RC circuit [Shi, 2011]. Therefore,

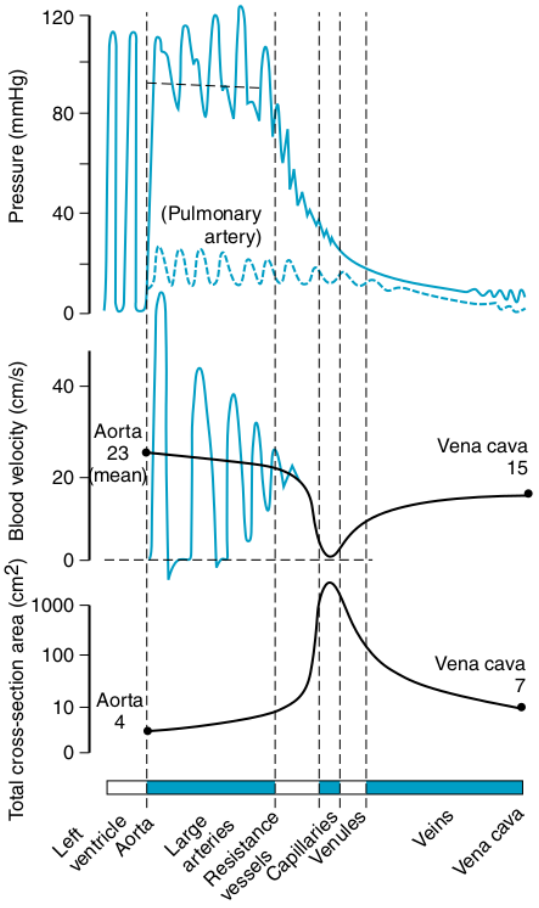

(a)

Fig. 2.4.: The top row shows the pressure oscillations along the vascular tree for the systemic (solid line) and pulmonary circulation (dashed line). We can see how the pressure oscillations, as well as the pressure itself, decrease downward the vascular tree, being the biggest drop at arterioles level. The bottom row shows the total cross-sectional area, we can see how initially it increases from the main arteries to the capillaries, and then it decreases as venules converge to veins. Moreover, we can see how cross-sectional area is a mirror image of the blood flow velocity. Reprint with authorisation from [Herring, 2018].

we can see the vascular system as many blood vessels arranged in series and parallel with respect to the heart, and we can use Kirchhoff's circuit laws to derive the equivalent properties, as we did for our haemodynamic model in Equation 3.10. In general the systemic circulation is divided into specialized, individual circuits, each supplying a specialized tissue or organ, with the arterial supply coming from the aorta. Thus, forming a parallel arrangement. Considering each organ as a resistance, all the elements in parallel experience the same driving pressure. Hence, this arrangement of the vascular system allows to regulate the flow through each organ independently without greatly affecting the total flow or blood pressure.

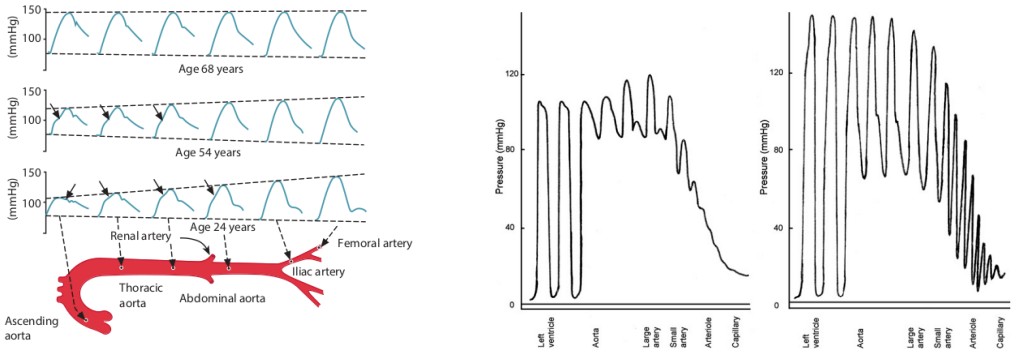

(a) Pulse pressure propagation

(b) Effect of stiffening in pressure oscillations

Fig. 2.5.: a) Pulse pressure wave propagation along the main arteries, reflection, refraction, and interference distort the pressure waveform. In young people it causes an additional diastolic wave in the proximal aorta and an exaggeration of systolic and pulse pressures in the distal arteries. Arrows show systolic inflection, marking the arrival of the reflected wave. Reprint with authorisation from [Herring, 2018] b) Effect of arterial stiffening in the attenuation of pulse pressure. Due to the increased stiffening of the arteries the pulsatile flow is transmitted to the microvasculature. Reprint with authorisation from [ORourke, 2007].

However, the electronic-hydraulic analogy fails to capture spatio-temporal effects such as the ones due to pressure wave propagation [Shi, 2011]. If arteries had rigid walls, blood pressure would rise virtually instantaneously throughout the arterial system during systole. However, arteries are not rigid, so the proximal pressure rise takes a finite time to spread to distal arteries. The pressure pulse travels at around 4–5 m/s in young people, and 10–15 m/s in older people, much faster than the blood velocity (0.2 m/s) in the ascending aorta. The pulse transmission is due to the ejected blood into the proximal aorta pushing to create space and initiating a chain reaction downwards. However, due to the peripheral resistance the amount of ejected blood is more than the one displaced. Hence, the additional blood distends the proximal aorta, which raises the blood pressure. As the displaced blood moves forwards it does partly distend the wall downstream (which raises the pressure there) and partly by displacing the blood ahead. This sequence repeats itself in rapid succession along the arterial tree. The pulse is thus transmitted by a wave of wall distension at 4–15 m/s. Since pulse propagation involves wall deformation, the stiffness of the wall affects the transmission velocity and transmission velocity increases with wall stiffness. The effect of this stiffening in the pressure oscillations along the vascular tree is visible In Figure 2.5b. Moreover, depending on the wall stiffness the pressure wave in a human proximal artery may show two additional features, namely a *diastolic wave* or a *systolic inflection*.

At low propagation velocities the decay of pressure in diastole is interrupted by a transient rise in pressure, called a diastolic or dicrotic wave, caused by wave reflection. This is not present at higher propagation velocities, in which the reflected wave returns to the proximal arteries in time to interact with the initiating wave, as can be seen in

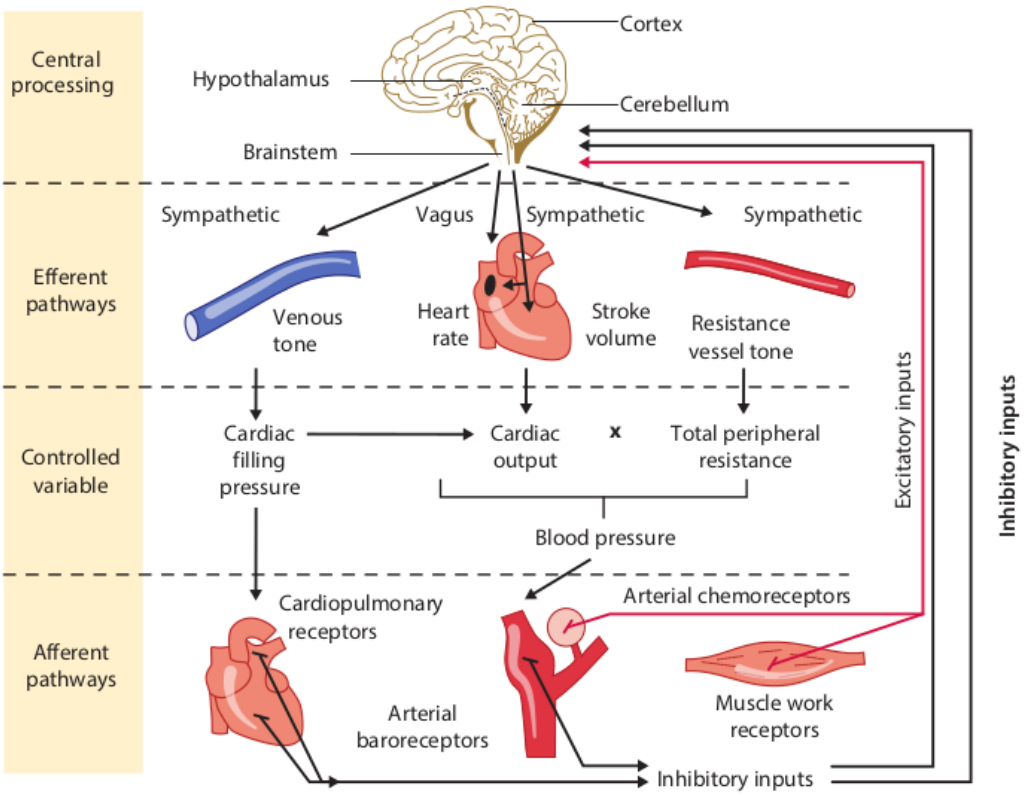

(a)

Fig. 2.6.: Summary of the regulatory mechanisms of the mean blood pressure, which depends on cardiac output (CO) and total peripheral resistance (TPR). Cardiac output depends on a complexity of numerous factors including: preload, contractility, afterload and heart rate. Peripheral resistance is equally complex and controlled by many additional factors including vasomotor tone of arterioles, metabolic activity, and response to blood flow by what is know as myogenic response, which modulates the arterial radii to compensate for pressure changes. Reprint with authorisation from [Herring, 2018].

Figure 2.5a. Thus the reflected wave is added to the late part of the systolic wave, raising the peak systolic pressure and creating a kink or flexion in the systolic wave. Reflected waves are important because they affect cardiac performance. The slow return of the reflected wave augments the diastolic pressure, which boosts coronary artery perfusion. By contrast, the early return of the reflected wave increases systolic pressure (systolic pressure augmentation). Therefore, the left ventricle must eject blood against an increased afterload, which increases cardiac work and O_2 demand.

Sometimes, these propagation effects must be accounted for to calculate the mean blood pressure (MBP). The MBP has an important clinical significance due to its close relationship to tissue perfusion. The two major determinants of MBP are cardiac output and total peripheral resistance, which regulate it through numerous physiological feedback mechanisms, as can be seen in Figure 2.6. However, in routine clinical practice only systolic and diastolic pressures are measured, not the complete pulse pressure waveform,

and usually in the brachial artery rather than aorta. In the aorta, mean pressure is approximately halfway between systolic and diastolic pressures; thus it can be obtained as $MBP = (SBP + DBP)/2$. Nevertheless, in the brachial artery the narrowing of the systolic peak, caused by distal transmission, shifts the time-averaged mean in the diastolic direction and the mean pressure is approximated as: $MBP = SBP + (2 * DBP)/3$.

2.3 The Brain

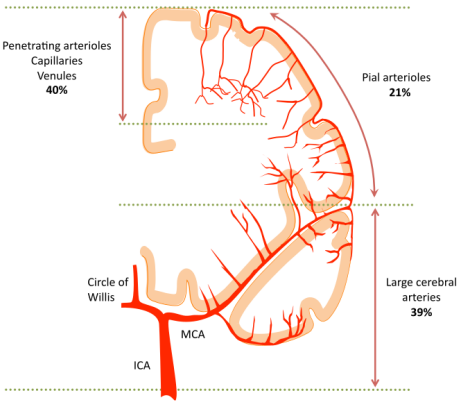

(a) Brain outside-in vascularisation

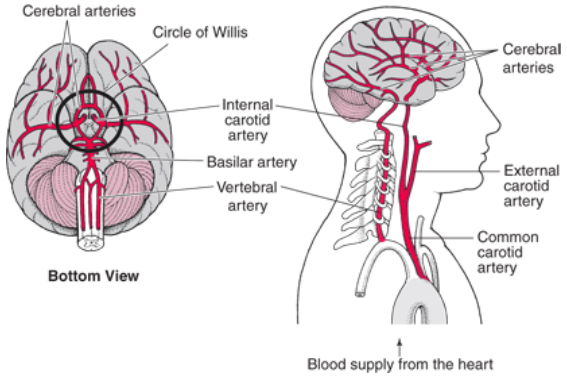

(b) Main arteries of the brain vascular tree

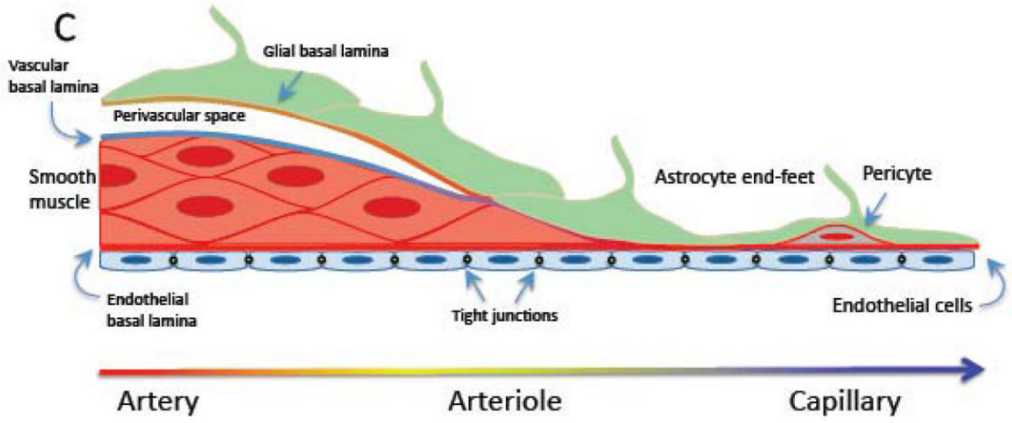

(c) Schematic of the vascular wall, from the large brain arteries until the capillaries

Fig. 2.7.: a) Brain outside-in vascularisation pattern. Arterioles penetrate the brain parenchyma from the pial arteries branching from the large arteries arising from the Circle of Willis. Reprint with authorisation from [Iadecola, 2017] b) Main arteries providing the blood supply to the brain. Details in the text. Image from www.joeniekrofoundation.com/ c) Schematic of the vascular wall anatomy from the large brain arteries to the capillaries. It can be seen that the perivascular spaces disappear at the arterioles and that the pericytes together with the endothelial cells give rise to the blood-brain barrier (BBB). Further details in the text. Reprint with authorisation from [Iadecola, 2013]

The brain is contained within the skull and is covered by three membranous layers, the meninges. From external to internal the meninges include the dura, arachnoid, and pia mater. The arachnoid and the pia are known as leptomeninges, or "thin" meninges, and the space between them is the subarachnoid space (SAS), which is filled with

cerebrospinal fluid (CSF). Many large blood vessels travel in the SAS and trabeculae (strings or sheets of leptomeningeal cells) cross the SAS connecting the arachnoid and pia. Beneath the pia lies the brain.

The brain can be divided in multiple cortical and subcortical structures. However, more generally it can be differentiated in two main tissues, grey matter (GM) and white matter (WM). Grey matter contains numerous cell bodies and relatively few myelinated axons, while white matter contains relatively few cell bodies and is composed mainly of long-range myelinated axons. Hence, white mater modulates the distribution of action potentials, coordinating communication between different brain regions. While, the human brain (1.5 kg) forms only 2% of the total body mass it receives 14% of the cardiac output and accounts for nearly 20% of resting O_2 consumption. Most of the blood goes to the grey matter (40% of brain mass), which has a very high basal blood flow, 100 mL/min/100g, 10 times the whole-body average and the double of the whole brain average, 55 mL/min/100g. Because of its high metabolic activity, grey matter is highly sensitive to hypoxia (deprivation of O_2); consciousness is lost after a few seconds of cerebral ischaemia, and irreversible neuronal damage follows within 4 min. Therefore, the primary task of the cerebral circulation is to maintain O_2 delivery at all costs.

The brain receives its blood supply from two paired arteries: the vertebral arteries, and the internal carotid arteries. These arteries arise in the neck, and ascend to the cranium, as can be seen in Figure 2.7b. The internal carotid arteries branch to form two major cerebral arteries, the anterior and middle cerebral arteries. The right and left vertebral arteries come together at the level of the pons on the ventral surface of the brainstem to form the basilar artery. The confluence of the internal carotid arteries and the basilar artery at the base of the brain forms an anastomotic circle, the Circle of Willis, which presumably improves the chances of any region of the brain to receive blood if one of the major arteries becomes occluded. From the Circle of Willis branches arise which supply the majority of the cerebrum. The main vessels arising from the circle of Wills form a dense, anastomotic network on the brain surface (pial arteries and arterioles), illustrated in Figure 2.7a. Pial arterial branches penetrate into the brain, giving rise to smaller arterioles surrounded by an extension of the subarachnoid space filled with CSF, the perivascular space or Virchow-Robin space, delimited by the vascular basement membrane and the basement membrane of the glia limitans [Dyrna, 2013; Mastorakos, 2019]. The perivascular space has emerged as critically important for removal of waste and unwanted proteins and peptides such as $A\beta$ [Iliff, 2013; Bakker, 2016; Wardlaw, 2020]. These spaces disappear as intracerebral arterioles reach deeper into the brain parenchyma and become smaller (diameter $<100\ \mu m$), as seen in Figure 2.7c. Then, as we reach the capillary level, vessel's basement membrane enters in direct contact with the glial basement membrane and give rise to the blood-brain-barrier (BBB). The capillary endothelial cells and pericytes interact with astrocytes, oligodendrocytes and microglia, to form together the **neurovascular unit**. The neurovascular unit is involved

in the regulation of nutrients, blood supply and waste removal. The goal is to protect the neurons by regulating the composition of the interstitial fluid (ISF). To this end, the capillaries of the BBB are exceptionally impermeable to lipid-insoluble solutes, such as plasma proteins and rely on specific carriers in the endothelial cell membrane to transport essential solutes between the blood and brain parenchyma. The capillaries drain into venules that course towards the cortex to reach the cortical veins and empty into dural venous sinuses, located in the dura matter, finally the sinuses drain into the internal jugular veins. Next to the sinus there are also meningeal lympathic vessels that support the drainage of CSF, although this pathway is poorly understood [Agarwal, 2021].

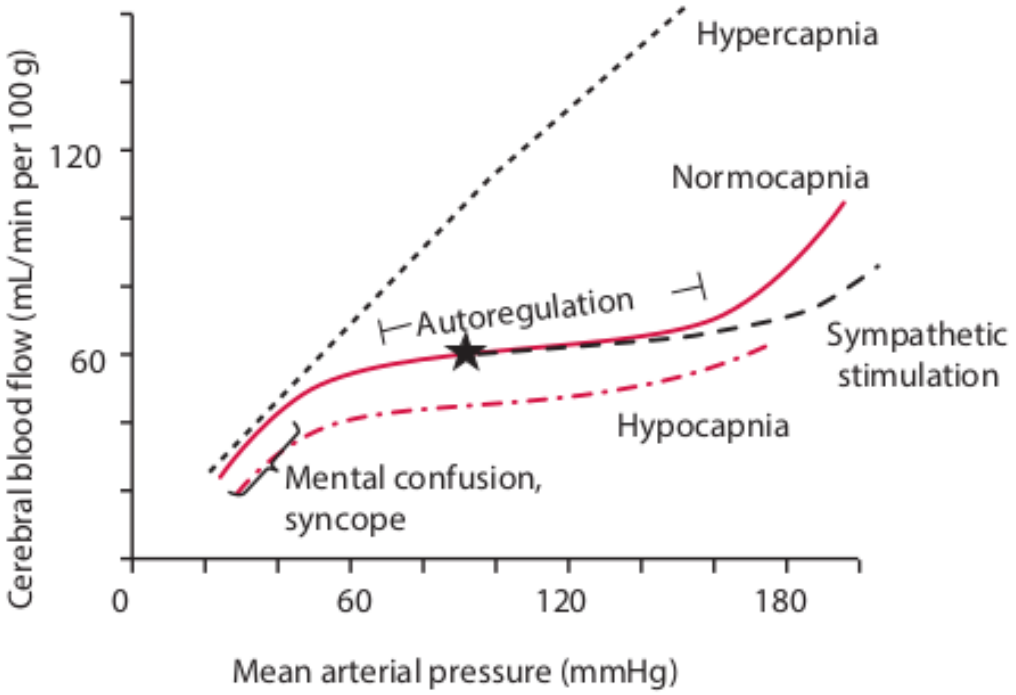

(a)

Fig. 2.8.: Pressure-flow curve of the cerebral autoregulation. This relationship deviates from the expected Poiseuille behavior due to the myogenic response. Inside the physiological limits blood flow is kept constant regardless of pressure changes thanks to the constriction or dilation of the arterioles. Reprint with authorisation from [Herring, 2018].

The blood supply in the brain is highly regulated, and local cerebral perfusion must adapt rapidly to changes in neuronal activity. Thus, cerebral blood flow (CBF) is regulated mainly by intrinsic mechanisms in response to mechanical and chemical signals, namely autoregulation and functional hyperaemia (increase of flow), rather than vasomotor nerves and hormones. For example, cerebral arterioles are unusually sensitive to arterial CO_2. Hypercapnia causes cerebral vasodilatation partly mediated by endothelial nitric oxide, NO, which helps to maintain O_2 supply during asphyxia. Conversely, hypocapnia causes cerebral vasoconstriction. Moreover, the vascular beds present an important autoregulation mechanism, keeping blood flow constant regardless of blood pressure, as

illustrated in Figure 2.8. This phenomenon is due to the vascular resistance changing in opposite direction to pressure (**autoregulation**). For example, a rise in pressure triggers resistance vessel constriction, which prevents flow from rising. Autoregulation is important because it helps to stabilise the blood flow in the brain in situations of fluctuating arterial pressures. However, beyond the physiological limits of autoregulation [60 - 160 mmHg], cerebral blood flow declines or increases steeply.

Thus, the cerebral perfusion has an additional pressure safeguarded, the regulation of other circulations. The brain can safeguard its blood supply by strangling the blood supply to other, less vital tissues, while sparing itself when necessary. The perfusion of the peripheral tissues, except the myocardium, is restricted via sympathetic-mediated vasoconstriction, to maintain arterial blood pressure and hence cerebral perfusion. Moreover, the brain also has control over the cardiac output and can regulate the hormonal activity, for example to induce the kidneys to reduce the overall blood volume.

2.4 CSF circulation and waste clearance

Cerebrospinal fluid (CSF) is a clear, colorless Newtonian fluid, with a viscosity similar to water, low in cells and proteins but generally similar to plasma in its ionic composition. For some time it was considered to be an ultrafiltrate of blood. However, careful analysis of the composition of CSF reveals that is not an ultrafiltrate. Currently, it is clear that CSF is an actively secreted product whose composition is dictated by specific transport mechanisms.

Figure 2.9 shows an schematic representation of the CSF flow. In short, the brain contains four ventricles which form a network of interconnected cavities. Within each cerebral hemisphere there is a relatively large lateral ventricle. The lateral ventricles communicate with the third ventricle, at the diencephalon, through the interventricular foramina (of Monro). The third ventricle in turn communicates with the fourth ventricle, located between the pons and cerebellum, through the narrow cerebral aqueduct (of Sylvius), the fourth ventricle continues caudally as the central canal of the spinal cord. Moreover, there are three apertures in the fourth ventricle through which the ventricular system communicates freely with the subarachnoid space. The median aperture (foramen of Magendie) and the two lateral apertures (foramina of Luschka). From the SAS, the main CSF draining pathway is believed to be through arachnoid (Pacchionian) granulations that drain into the dural venous sinuses. This absorption process is due to the pressure gradient (3–5 mmHg) between the subarachnoid space and the dural venous sinuses. However, the overall contribution of this mechanism of CSF drainage is unknown.

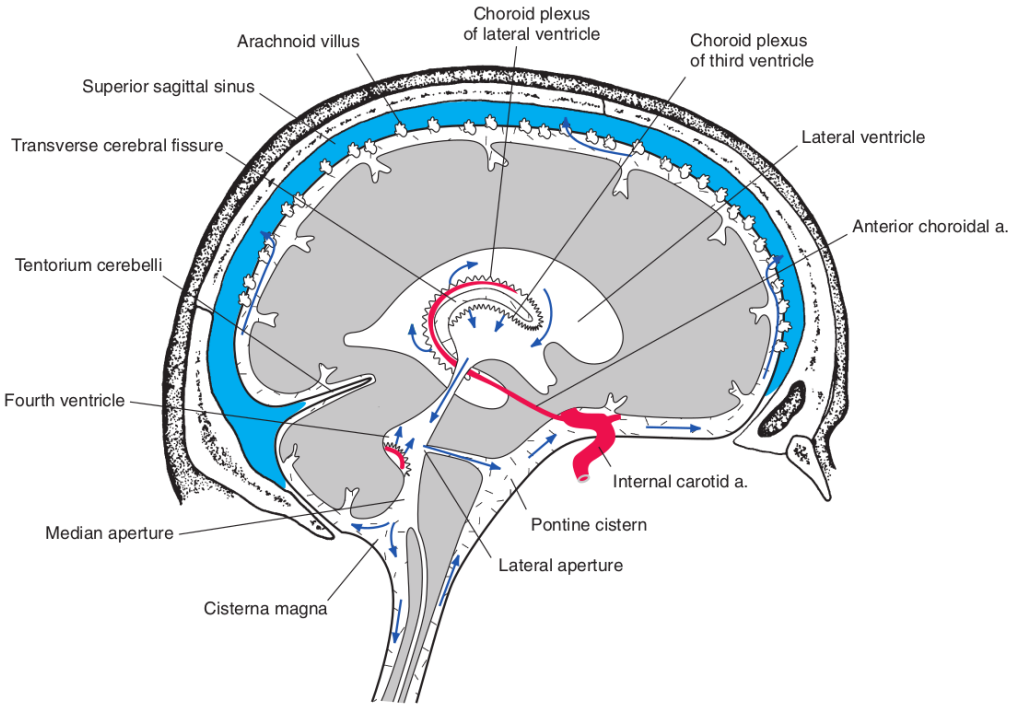

Fig. 2.9.: Path of CSF circulation (blue arrows) from its formation in the ventricles to its absorption into the superior sagittal sinus. Reprint with authorisation from [Vanderah, 2015].

All four ventricles contain strands of a highly specialised tissue, the choroid plexus, that secretes most of the CSF. It is located in the roof of the third and fourth ventricles, and the walls of the lateral ventricles. Functionally the choroid plexus is a three-layered membrane between blood and CSF, the first layer is a fenestrated endothelial capillary wall. Allowing easy movement of substances out of the capillary (in contrast to BBB walls). The second layer consists of scattered pial cells and some collagen. The third layer is the choroid epithelium, derived from the same layer of cells that forms the ependymal lining of the ventricles. The blood is filtered through the fenestrations of the choroidal capillaries, followed by the active transport of substances into the ventricle. Moreover, although CSF is secreted primarily by the choroid plexus, lesser amounts are also secreted by the arachnoid, ependymal, and perivascular spaces of the brain. The vascular supply of the choroid plexus is provided by the anterior and posterior set of choroidal arteries and drained by the choroidal vein. The total process is actually more complicated than this, but out of the scope of this Chapter, see [Vanderah, 2015] for more information.

Given that there is approximately 150 mL of CSF circulating in the ventricles and subarachnoid space, and that the production is about (400 - 600 mL/day), it means that CSF is completely turned over three to four times per day. The rate of formation of new CSF is relatively constant and little affected by systemic blood pressure or intraventricular pressure. However, CSF circulation is a dynamic phenomenon related to the cardiac cycle and respiration. The pulsatile motion generates a small net movement towards

the superior sagittal sinus with each heartbeat. In addition, some CSF moves from the cisterns around the fourth ventricle into the subarachnoid space around the spinal cord. The pulsatile motion of CSF is thought to be due to the contraction and expansion of the ventricular space. This process may be due to blood entering and leaving the brain [Loth, 2001], or the expansion of the choroid plexus of the lateral ventricles [Bering, 1955].

The main role of CSF is to provide mechanical support and homeostatic regulation of the brain's parenchymal interstitial fluid. Mechanically, it has a buoyant effect on the brain and it is a shock absorber. In addition, CSF serves as part of a spatial buffering system required by the fact that the brain lives inside a rigid skull. Hence, according to the Moroe-Kellie doctrine [Wilson, 2016], the total amount of volume inside the skull must be constant at all times. This implies that when the heart pumps arterial blood into the brain with each heartbeat space has to be made for this arterial blood, partly by venous blood leaving, and partly by CSF leaving. Moreover, CSF acts functionally as a drainage system for waste and inflammatory byproducts, regulating the composition of the interstitial fluid, and providing a route through which certain chemical messengers can be widely distributed throughout the nervous system.

The drainage of waste is likely to occur most actively within the perivascular spaces located in sensitive areas of the brain. For example, it has been seen that clearance of waste is accentuated during sleep, described together with an expansion of the interstitial space [Xie, 2013; Iliff, 2013]. Moreover, enlarged perivascular spaces are considered to reflect an accumulation of waste products and are considered as a pathological biomarker [Wardlaw, 2020]. However, the exact mechanisms behind the perivascular flow and its role in waste removal are unknown and a current source of controversy.

Currently there are two main hypothesis. In one hand some researchers support the glympathic hypothesis [Mestre, 2020], which states that the perivascular spaces serve as an entry point for CSF into the brain parenchyma, presumably with the help of the arterial pulsations and/or vasomotion [Mestre, 2018; Veluw, 2020]. Then, the convective flow induced by the arterial pulsations enhances the ISF waste removal towards the perivenous spaces, which efflux into the subarachnoid space. However, it is not clear if convective flow in the extracellular space is possible or not [Pizzo, 2017; Abbott, 2018; Rey, 2018; Tithof, 2019]. The other main hypothesis, considers that the perivascular flow takes place along the arteries towards the SAS space. In this case the ISF waste is drained into the perivascular spaces of the arteries and vasomotion/arterial pulsations drive the flow upwards [Agarwal, 2021].

More information regarding the CSF dynamics and its complex coupling with other cerebral fluids and surrounding tissues can be found in [Sweetman, 2011; Bothwell, 2019; Thomas, 2019; Rey, 2018; Bacyinski, 2017].

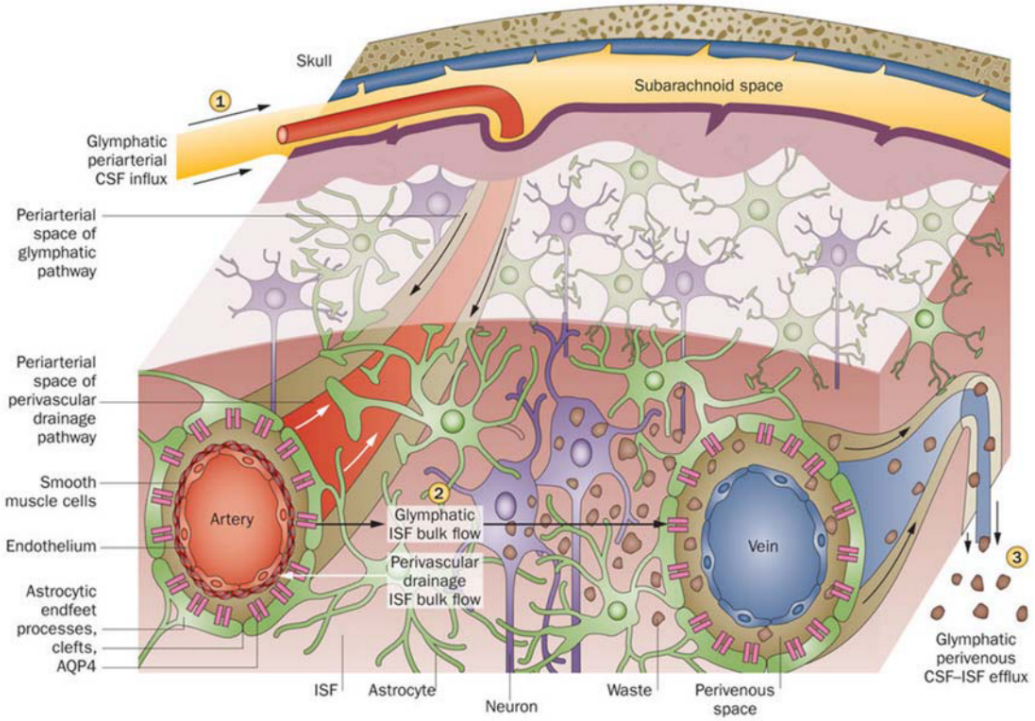

Fig. 2.10.: Schematic of glymphatic (black arrows) and perivascular (white arrows) waste clearance routes. According to the glymphatic model, CSF flows along para-arterial spaces (1), mixes with interstitial fluid (ISF) and solutes (2), and is cleared from the brain along para-venous spaces (3). Efficient glymphatic clearance of waste and solutes is dependent on fluid movement across aquaporin-4 (AQP4) channels located on astrocytic endfeet surrounding the parenchymal vasculature. In contrast, perivascular drainage of ISF and solutes occurs along the middle layers of the basement membrane of arterial smooth muscle cells and flows in a direction opposite to that of glymphatic clearance. Reprint with authorisation from [Bacyinski, 2017].

2.5 Heart & Brain Relationship

Heart and brain have numerous bi-directional physiological feedback mechanisms around blood flow and its regulation, as can be seen in Figure 2.6. From these mechanisms we can observe that impaired cardiac function affects cerebral structure and functional capacity, while neuronal signal modulates the cardiovascular function. Thus, neuro-cardiac feedback signals may promote or aggravate the progression of certain diseases [Doehner, 2018]. However, the diversity of heart-brain interactions makes difficult to make a comprehensive overview. Nevertheless, from the presented mechanisms we can observe that damage to micro and macro vasculature compromises cerebral perfusion and hampers the synchronised movement of CSF and possibly perivascular flow, affecting the drainage of waste products and leading to neuronal and glial degeneration.

Indeed, microvasculature dysfunction has been linked to neurodegeneration through the association of common abnormalities seen on brain imaging and linked to microvessel

damage [Wardlaw, 2019], such as white-matter hyperintensities (WMHs), microinfarcts, or microbleeds [Wardlaw, 2015]. In turn, these abnormalities have been associated to cognitive decline [Debette, 2010] and abnormal blood pressure [Gupta, 2018; Moroni, 2018]. The origin of some of these lesions is due to the brain susceptibility to small ischemic events. Due to the "outside in" vascularisation pattern, the blood flow regulation outside the brain parenchyma must be coordinated with the intracerebral microvasculature, and occlusion of penetrating arterioles or venules cannot be effectively compensated by anastomotic branches, which results in flow reductions sufficient to produce small ischemic lesions [Iadecola, 2013; Roos, 2017].

Another important factor is the elevated endothelial wall stress that may be experienced by the brain microvasculature due to pulsatile flow transmission [Stone, 2015; Toth, 2017]. As presented in Figure 2.5b the pulsatility of blood flow increases with the stiffening of main arteries, which increases with age [ORourke, 2007], and may explain why vascular cognitive impairment is closely related to ageing [Dichgans, 2017]. The decreased attenuation of pressure oscillations leads to a pulsatile flow in the capillary bed instead of a steady-flow. This may increase stress on the capillary endothelial wall and lead to endothelial dysfunction, which hampers cerebrovascular reactivity, affecting the ability of arterioles and capillaries to modify their radii in response to neuronal activity and direct blood flow where needed [Østergaard, 2013]. In turn, impaired blood flow has been associated with increased levels of neuronal oxidative stress, resulting in cerebral inflammation, that can also lead to vascular damage [Iadecola, 2013; Wolters, 2018]. In association studies, carotid arterial stiffness has been negatively associated with cerebral blood flow in older adults [Tomoto, 2021], and cerebral hypoperfusion has been associated with accelerated cognitive decline and increased risk of dementia in the general population [Wolters, 2017].

At the same time, the brain can regulate the cardiac function altering heart's contractility or heart rate depending on its perfusion needs. However, stiffening of the arteries affects cardiovascular coupling; the decreased elasticity of the main arteries rises the systolic pressure, which in turn forces the heart to increase its contractility or heart rate in order to supply the same amount of blood. Therefore, a prolonged hypertension may result in cardiac remodelling processes such as left-ventricular hypertrophy, which has been associated to a lower brain volume [Patel, 2017] and a higher burden of WMHs [Ryu, 2014]. Hence, impaired cardiac function may result in impaired brain perfusion, and may explain the relationship between heart failure (HF) [Doehner, 2018] or atrial fibrillation (AF) [Diener, 2019; Sepehri Shamloo, 2020] with cognitive decline.

Thus, all together highlights that cardiac function and brain status must be studied jointly in order to elucidate the underlying mechanisms connecting cardiovascular function and neurodegeneration.

3 Biophysics-constrained Statistical Learning for Heart & Brain Analysis

Contents

In this chapter we present how to include prior physiological knowledge in multi-organ interactions, focusing on the heart-brain relationship. This work is motivated by epidemiological studies, such as the UK Biobank, which provide joint cardiac and brain imaging information for thousands of individuals. This represents a unique opportunity to study the relationship between heart and brain. Currently, most of research on large multimodal databases has been focusing on studying the associations among the available measurements by means of standard statistical models. However, these approaches do not provide insights about the underlying mechanisms and are often hampered by the lack of prior knowledge on the physiological relationships between measurements. For instance, important indices of the cardiovascular function, such as cardiac contractility, cannot be measured in-vivo. While these non-observable parameters can be estimated by means of mechanistic models, their personalisation is generally an ill-posed problem. Therefore, to jointly study brain and heart, we propose an approach in which the parameter personalisation of a lumped cardiovascular model is constrained by the statistical relationships observed between model parameters and brain-volumetric indices extracted from imaging and clinical information such as age or body surface area, in order to obtain population-wise consistent solutions. This work is currently under review in Medical Image Analysis (MedIA) and a preliminary version was presented at the FIMH conference in 2019 [Banus, 2019].

3.1 Introduction

Heart and brain are linked by pathophysiological and physiological mechanisms sharing several risk factors [Doehner, 2018]. For instance, despite the heterogeneous clinical manifestations of cerebrovascular diseases and cognitive decline, clinical evidence supports a common underlying cardiovascular pathophysiology relating cardiac function and brain damage [Moroni, 2018]. Moreover, there is a variety of heart diseases such as heart failure (HF) [Ois, 2008] or atrial fibrillation (AF) [Benjamin, 2018] that are considered independent risk factors for dementia [Chen, 2018; Alonso, 2016] and have been related to cerebrovascular diseases, doubling the risk of dementia [Azarpazhooh, 2018].

Nevertheless, the lack of databases integrating heart and brain data of the same subjects has prevented to study their relationship in depth, in particular through advanced modelling tools. Current initiatives providing systemic databases of both heart and brain imaging information, such as UK Biobank [Sudlow, 2015] or the Heart-Brain study [Hooghiemstra, 2017], have the potential of improving our understanding by means of large-scale data analysis. From cardiac imaging data it is possible to obtain volumetric indices characterising cardiac function, such as stroke volume (SV), cardiac output (CO), end-diastolic volume (ESV) or end-systolic volume (EDV). From brain imaging we can obtain indices related to the main structures present in the brain, subcortical regions, or pathological indices such as white matter hyperintensities (WMHs). WMHs are a common marker of brain damage associated to dementia, cognitive decline and risk of stroke [Wardlaw, 2015] and can be measured as hyperintense regions in T2-weighted magnetic resonance images (MRI). Although the pathogenesis of WMHs remains unclear, current hypotheses suggest a vascular origin, supported by the association with elevated blood pressure [Modir, 2012; Moroni, 2018], brain hypoperfusion [Jefferson, 2009] and cardiac pathologies such as HF [Alosco, 2013] or AF [Alonso, 2016].

The link between cardiovascular risk factors and brain imaging changes is commonly studied by means of multivariate regression analysis or proportional hazards models [Debette, 2010; Friedman, 2014]. However, there are several descriptors of the cardiac function that are not possible to obtain in-vivo such as cardiac fibre contractility or stiffness among others, thus limiting the hypotheses that can be tested, along with the interpretation of the results. Cardiovascular biophysical models allow to estimate these descriptors through data assimilation procedures and provide mechanistic insights of the cardiac function that can help us to better understand its effects on the brain.

To tackle this problem, we propose an approach in which we combine the personalisation of a biophysical model, deriving non-observable parameters, with statistical learning to link cardiac function to brain damage using indices extracted from imaging data available in UK Biobank. We represent the interaction between the brain state and cardiac function

by constraining the space of feasible solutions of the model. Our approach extends the work described in [Molléro, 2018] and our preliminary work presented in [Banus, 2019] and is based on a group-wise regularisation term parameterised by a covariance matrix that takes into account the relationships between model parameters (e.g. contractility) and external indices not present in the model, such as brain volumetric indices (e.g. WMHs).

First, we applied our framework to a large cohort composed by more than 3400 subjects for which cardiac and brain information is jointly available in the UK Biobank database, identifying statistically significant associations between the personalised model parameters and brain volumetric features that match findings reported in previous clinical studies. Next, we explored the plausibility of the learned relationships by inferring the model parameters in the absence of part of the target clinical features. Finally, we applied the developed framework in a subset of subjects diagnosed with AF, demonstrating the ability of the framework to identify significant differences associated to clinical conditions. To our knowledge, no patient-specific modelling study relating brain damage and cardiovascular parameters has been done before, and this study presents the largest cohort of personalised subjects to date.

The paper is structured as follows. Section 3.2 introduces the context of our work and Section 3.3 introduces the methodological framework, describing the biophysical model, the personalisation approach and how we combine it with group-wise regularisation. Next, in Section 3.4 the framework is applied to brain and heart data, first using the whole cohort and then in a subset of subjects diagnosed with AF. We detail the data preprocessing and inclusion criteria and examine the obtained results and the plausibility of the model based on the learnt relationships. Finally, in Section 3.5 the limitations of our framework and possible future directions are discussed and in Section 3.6 we summarise the conclusions of our work.

3.2 Methodological context

Usually the association between cardiac imaging indices and vascular risk factors (VRFs) such as hypertension, diabetes, smoking, obesity or hyperlipidemia with brain imaging features is studied by means of standard statistical tools such as multivariate regression or survival analysis models. Following these analyses, cardiac output and reduced brain blood flow have been associated to greater WMHs burden [Jefferson, 2009; Bahrani, 2017], while a review of 46 longitudinal studies associated WMHs with a higher risk of dementia [Debette, 2010]. Moreover, based on a meta-analysis of 77 studies VRFs were found to be independently associated with brain imaging changes even before the clinical manifestation of cardiovascular or cerebrovascular diseases [Friedman, 2014]. More

recently, studies based on the UK Biobank have supported these findings. In [Veldsman, 2020] cerebrovascular risk factors were associated with reduced cerebral grey matter and white matter integrity, and in [Cox, 2019] hypertension was independently associated with generalised atrophy of the brain (reduced brain volume and thinner cortex) and a higher burden of WMHs, while increased pulse pressure was related to poorer white matter measures.

The use of cardiovascular models enables to study the effect of cardiac function in the brain from a mechanistic perspective, and allows to introduce prior knowledge on the physiological links between the available measurements. For example, [Scarsoglio, 2017] studied the effect of AF in brain perfusion and determined that the loss of periodicity in the AF beat-series leads to a higher occurrence of hypoperfuse and hypertense events in the distal regions of the cerebrovascular circulation (arterioles and capillaries). Additionally, [Aghilinejad, 2020] determined that the stiffening of the aorta relative to the carotid arteries increased the pulsatility of blood flow in the brain vasculature, leading to increased microvascular damage.

However, personalising a cardiovascular model for a given subject is an inverse problem that implies estimating the model parameters such that generate simulation results as close as possible to the available clinical data. Carrying out the personalisation of such models is complex. This problem is commonly ill-posed and its complexity scales quickly with the number of parameters. Several approaches have been proposed for cardiac-related inverse problems. When sequential data is available, it is common to rely on filtering approaches such as the unscented Kalman filter (UKF) [Pant, 2017] that corrects the model based on the discrepancy between the input data and model's prediction. Other options involve data-driven approaches such as reinforcement learning [Neumann, 2016], gradient-based approaches based on the adjoint method [Delingette, 2012] or gradient-free approaches such as genetic algorithms [Khalil, 2006]. Moreover, multi-fidelity approaches, based for example on evolutionary algorithms [Molléro, 2017] or filtering approaches [Pant, 2014], have been used to combine the computational efficiency of reduced-order models with the accuracy of higher-order models. Personalisation is commonly carried out at most in tens or a few hundreds of subjects [Molléro, 2018]. Hence, typically the approaches are oriented towards obtaining solutions that mimic the observed clinical features but they do not prioritise obtaining homogeneous solutions in groups of subjects. Therefore, due to the ill-posed nature of the problem, a large variability between solutions in similar subjects can be found. This is a problem if we wish to include the estimated parameters in any post-hoc analysis with the other available clinical information, such as brain volumetric indices.

3.3 Methodological framework

3.3.1 Cardiovascular biophysical model

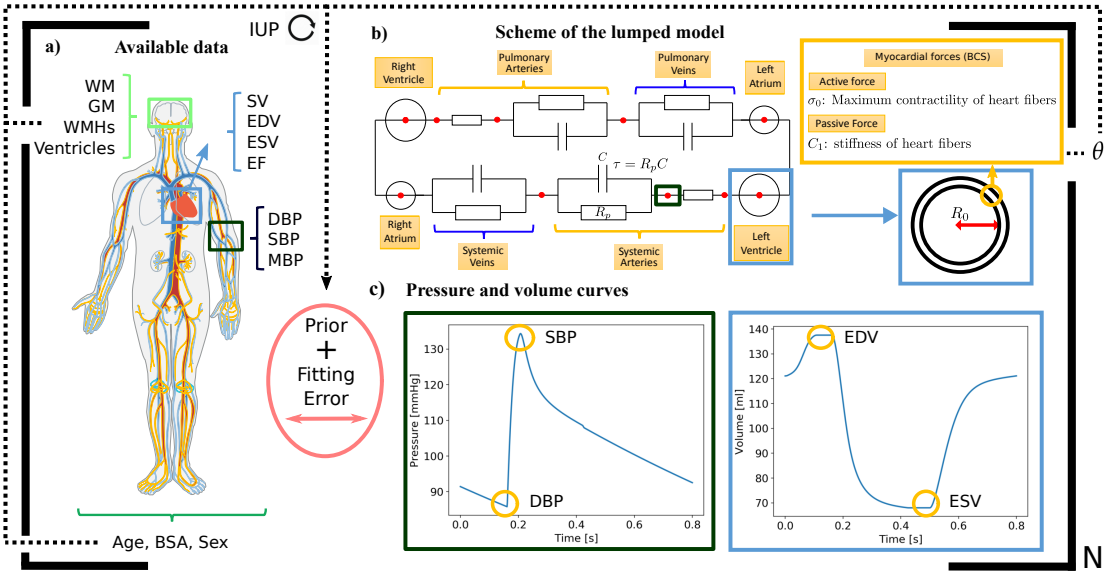

Fig. 3.1.: Graphical scheme of the iterative updated priors (IUP) personalisation approach. Dashed lines represent which information is grouped across the N subjects to define the prior. a) Summary of the available data for each subject, including cardiac data, socio-demographic information, blood pressure measurements and brain volumetric indices. b) Simplified representation of the lumped model showing the parameters used in the personalisation (θ). C characterises the compliance of the main systemic arteries, R_p the peripheral resistance, τ represents the characteristic time of the RC system, R_0 the radius of the left ventricle, σ_0 the contractility of the cardiac fibres and C_1 their stiffness. c) Example of the pressure and volume curves that can be obtained from the model. From these curves we extract scalar indices (e.g. EDV, ESV) to match the available clinical data (target features). Curves have been extracted from the model locations with the corresponding matching frames colours.

In our work the cardiovascular model is the joint contribution of two components: a lumped model simulating the haemodynamics of the vascular system relying on the electronic-hydraulic analogy; and an electromechanical model of the heart (see Figure 3.1). In the lumped model pressure and blood flow curves are simulated at specific locations of the cardiovascular system throughout the cardiac cycle. We can formalise a system of ordinary differential equations (ODEs) that defines the flow-pressure dynamics at each of the represented compartments of the model; the systemic and pulmonary circulations are represented as a three-element Windkessel (RCR) model coupled to a venous return (RC). The modelling of the electromechanical behaviour of the heart is carried out by the Bestel-Clement-Sorine (BCS) model [Chapelle, 2012; Marchesseau, 2013]. The sarcomere contractile forces are modelled as the sum of a passive non-linear elasticity and an active contraction in the fibre's direction. The model is able to replicate the Starling effect and is compatible with the laws of thermodynamics. The 0D reduction of the joint model was derived in [Caruel, 2014]. In short, the ventricle is treated as a 3D symmetric sphere in the 0D model, where the myocardial forces and motion can be described by the inner radius (R_0) of the ventricle. Deformation and stress tensors are also reduced to 0D forms, allowing to characterise the heart contractile (σ_0) and elastic

(C_1) properties of the heart. A scheme of the model is shown in Figure 3.1b. Next, we explore in detail the components of the model:

3.3.1.1 The BCS model: modelling sarcomere contraction

The BCS model describes the mechanical behaviour of the heart as a combination of a passive isotropic stress represented by a viscous pseudo-potential and a hyperelastic potential describing the extracellular matrix, in parallel with an active stress along the fibre direction describing the sarcomere contraction. The model is compatible with the laws of thermodynamics and the active stress part describes the physiological contraction of the sarcomere in a macroscopic scale, this allows to observe phenomena such as the Starling Effect.

The active force in the sarcomere is modelled by an extension of the Huxley's filament model [Huxley, 1957]. It models the kinetics of cross-bridges formations between the actin and myosin filaments at the nanoscopic scale. At the mesoscopic scale, it results in a differential equation which relates the overall active stress in the sarcomere τ_c, the overall stiffness k_c and the strain e_c describing the relative displacement of actin vs myosin filaments:

$$\begin{cases} \dot{k_c} = -(|u|_+ + w\,|u|_- + \alpha \dot{e_c}) k_c + n_0 k_0\,|u|_+\,, & (3.1) \\ \dot{\tau_c} = -(|u|_+ + w\,|u|_- + \alpha \dot{e_c}) \tau_c + \dot{e_c} k_c + n_0 \sigma_0\,|u|_+\,, & (3.2) \end{cases}$$

where n_0 represents the total number of myosin heads, w a variable representing the length-dependence effect, α is a constant related to the cross-bridge destruction during contraction, k_0 and σ_0 are respectively the maximum stiffness and contraction. u is a variable that controls the reaction rate during contraction and relaxation related to calcium kinetics, it depends on the depolarisation T_d and repolarisation T_r times of the sarcomere. If u is positive we use $|u|_+$ and $|u|_-$ if it is negative. They respectively represent the rate of force build-up during contraction k_{ATP} and relaxation k_{RS}.

$$u = \begin{cases} k_{ATP} & \text{when } T_d \leq t \leq T_r, \\ -k_{RS} & \text{otherwise}, \\ |u|_+ = \max(u, 0), & \\ |u|_- = -\min(u, 0). & \end{cases} \tag{3.3}$$

3.3.1.2 Overall constitutive law

The active force is applied along the fibre direction, it consists of a contractile element in parallel with a viscous component μ and in series with a linear elastic element, made of a spring E_s. As derived in [Caruel, 2014], the stress σ_{1D} along the fibre direction is given by:

$$\begin{cases} \sigma_{1D} = E_s \dfrac{e_{1D} - e_c}{(1+2e_c)^2}, & (3.4) \\ (\tau_c + \mu \dot{e_c}) = E_s \dfrac{(e_{1D} - e_c)(1+2e_{1D})}{(1+2e_c)^3}, & (3.5) \end{cases}$$

where $e_{1D} = \underline{\tau_1} \cdot \underline{\underline{e}} \cdot \underline{\tau_1}$ is the strain in the fibre direction τ_1 ($\underline{\underline{e}}$ is the Green-Lagrange strain tensor).

For the passive component describing the extracellular matrix properties an isotropic hyperelastic Mooney Rivlin material is used. The strain energy is given as:

$$W_e = C_1(I_1 - 3) + C_2(I_2 - 3) + \frac{K}{2}(J-1)^2, \tag{3.6}$$

where I_1, I_2 and J are the invariants of the Cauchy-Green deformation tensor, C_1, C_2 are parameters of the material and K is the bulk modulus. The material parameters influence mainly the EF and the maximum pressure while K acts mainly during the relaxation phase.

3.3.1.3 Haemodynamic Model

The mechanical equations are coupled to a basic circulation model implementing the 4 phases of the cardiac cycle. For a given ventricle we note define P_{at} the pressure in the atrium, P_{ar} the pressure in the artery and P_v the pressure in the ventricle, the phases of the cardiac cycle are the following:

- *Diastolic Filling*: $P_v \leq P_{at}$, the atrial valve is open and the ventricle is filled up with blood.

- *Isovolumetric contraction*: Contraction starts, P_v rises. $P_{at} \leq P_v \leq P_{ar}$ and all the valves are closed.

- *Systolic Ejection*: $P_v \geq P_{ar}$, the arterial valve opens and blood is ejected into the artery.

- *Isovolumetric relaxation*: Contractile forces disappear, P_v decreases so: $P_{at} \leq P_v \leq P_{ar}$, all the valves are closed.

We use the haemodynamic model introduced by [Chapelle, 2012] which links the blood flow q to the ventricular, atrial and arterial pressures with the following equations:

$$q = \begin{cases} K_{at}(P_v - P_{at}), \text{ if } P_v \leq P_{at} \\ K_{iso}(P_v - P_{at}), \text{ if } P_{at} \leq P_v \leq P_{ar} \\ K_{ar}(P_v - P_{ar}) + K_{iso}(P_{ar} - P_{at}), \text{ if } P_v \geq P_{ar}, \end{cases} \tag{3.7}$$

where K_{at}, K_{iso} and K_{ar} are regularisation constants. They have to be chosen such that K_{iso} is much smaller than K_{at} and K_{ar} in order to keep blood flow during isovolumetric phases negligible.

Here the mechanical behaviour of the atrium is modelled by a time varying elastance E_{last}; this elastance is related to the P_{at} by:

$$P_{at} = E_{last}(V_{at} - V_{at\_0})(1 - qK_{at}), \tag{3.8}$$

$$E_{last} = \begin{cases} E_{at}Lower \left(1 + \frac{\frac{E_{at}Upper}{E_{at}Lower} - 1}{1 + e^{-r1\left(t - \frac{P_{at\_t2} + P_{at\_t1}}{2}\right)}} \right) \text{ if } P_{at\_t1} < t \leq P_{at\_t2}, \\ E_{at}Lower \left(1 + \frac{\frac{E_{at}Upper}{E_{at}Lower} - 1}{1 + e^{r2\left(t - \frac{P_{at\_t2} + P_{at\_t3}}{2}\right)}} \right) \text{ if } P_{at\_t2} < t \leq P_{at\_t3}, \\ E_{at}Lower \text{ if } otherwise, \end{cases} \tag{3.9}$$

where V_{at} represents the blood volume in the atrium and V_{at_0} the initial blood volume at the beginning of the cardiac cycle. E_{last} is characterised by three times, P_{at_t1}, P_{at_t2}, and P_{at_t3}. Which are the times at which elastance starts to increase, reaches its maximum E_{at_Upper} and returns to its base value E_{at_Lower} respectively. This allows to simulate a pressure bump at the beginning of the cardiac cycle that accounts for the contraction of the atrium.

The pressure of the artery P_{ar} (cardiac afterload) is modelled with the 3-parameters Windkessel model [Westerhof, 2009] and coupled to the ventricular outflow q through the equations:

$$R_p C_{ar} \dot{P_{ar}} + P_{ar} - P_{ven} = (R_p + Z_c)q + R_p Z_c C_{ar} \dot{q}, \tag{3.10}$$

where R_p is the peripheral resistance, Z_c is the Characteristic impedance, C_{ar} is the arterial compliance and P_{ven} is the venous pressure after the capillaries.

3.3.1.4 Reduced Equations for the 0D model

The 0D model of the heart is derived from the described 3D model by [Caruel, 2014]. The reduction of the equations is done following a set of assumptions: the ventricle is considered as a sphere, the material is incompressible, and the electrical activity is synchronous and homogeneous over the sphere. These assumptions allow to characterise the myocardial forces and motions by the radius of the ventricle R_0. The complete system of simplified equations is the following:

$$
\begin{cases}
\dot{k_c} = -(|u|_+ + w\,|u|_- + \alpha \dot{e_c}) k_c + n_0 k_0\,|u|_+ & \text{(a)} \\
\dot{\tau_c} = -(|u|_+ + w\,|u|_- + \alpha \dot{e_c}) \tau_c + \dot{e_c} k_c + n_0 \sigma_0\,|u|_+ & \text{(b)} \\
(\tau_c + \mu \dot{e_c}) = E_s \dfrac{(e_{1D} - e_c)(1 + 2e_{1D})}{(1 + 2e_c)^3} & \text{(c)} \\
\sigma_{1D} = E_s \dfrac{e_{1D} - e_c}{(1 + 2e_c)^2} & \text{(d)} \\
e_{1D} = \dfrac{C - 1}{2} & \text{(e)} \\
C = (1 + \dfrac{y}{R_0})^2 & \text{(f)} \\
\sigma_{passive} = 4(1 - C^{-3})(c_1 + c_2 C) & \text{(g)} \\
\sigma_{viscosity} = \eta(1 + 2C^{-6})\dot{C} & \text{(h)} \\
\Sigma_{sph} = \sigma_{1D} + \sigma_{passive} + \sigma_{viscosity} & \text{(i)} \\
\rho d_0 \ddot{y} = P_v (1 + \dfrac{y}{R_0})^2 - \dfrac{d_0}{R_0}(1 + \dfrac{y}{R_0}) \Sigma_{sph} & \text{(j)} \\
q = 4\pi R_0^2 (1 + \dfrac{y}{R_0})^2 \dot{y} = & \\
\quad \begin{cases}
K_{at}(P_v - P_{at}), \text{ if } P_v \leq P_{at} \\
K_{iso}(P_v - P_{at}), \text{ if } P_{at} \leq P_v \leq P_{ar} \\
K_{ar}(P_v - P_{ar}) + K_{iso}(P_{ar} - P_{at}), \text{ if } P_v \geq P_{ar},
\end{cases} & \text{(k)} \\
R_p C_{ar} \dot{P_{ar}} + P_{ar} - P_{ven} = (R_p + Z_c) q + R_p Z_c C_{ar} \dot{q}, & \text{(l)} \\
C_{ven} \dot{P_{ven}} + q = (P_{at} - P_{ven}) / R_{ven}, & \text{(m)}
\end{cases}
$$

Equations (a), (b), (c) and (d) are the same sarcomere and visco-elastic equations than Equations 3.2 & 3.5, but here are calculated once for the whole sphere. C in equations (e), (f), (g) and (h) denotes a component of the simplified Cauchy-Green deformation tensor which depends only on $y = R - R_0$. $\sigma_{passive}$ is the stress due to the passive law and $\sigma_{viscosity}$ is the stress due to an additional viscous damping, η, both expressed as a simple function of C (see [Caruel, 2014] for the full derivations). In equation (i) Σ_{sph} is the sum of all the stresses applied to the sphere. Equation (j) is the resulting equation of motion which is coupled to the haemodynamic model (k) and the Windkessel equation (l). The three of them give raise to a system of equations that needs to be solved at each iteration.

Moreover, assuming synchronous and homogeneous electrical activation means that the whole ventricle is depolarised simultaneously. During isovolumetric contraction this leads to a rising rate of ventricular pressure which is very close to the rate of force

build-up k_{ATP} of the active stress τ_c. And equivalently, the rate of ventricular pressure decay during isovolumetric relaxation is closely related to k_{RS}. Nevertheless, in the 3D model pressure's rise and decay rates are also very dependent on the time that takes for the ventricle to be fully depolarised. This time corresponds approximately to the QRS duration. In order to correct this discrepancy between the models the control variable u is used to take into account the QRS duration, QRS_d. To this goal, a variable f_{depo} is defined, which takes into account the fraction of the ventricle which is currently depolarised. This is modelled as a piecewise linear function of time which depends on T_d, T_r and QRS_d. Therefore, the values of $|u|_+$ and $|u|_-$ are adapted to depend on the value of f_{depo} as described in Equation 3.11.

$$
\begin{aligned}
f_{depo} &= \begin{cases} \dfrac{t - T_d}{QRS_d}, \text{ if } T_d \leq t \leq T_d + QRS_d \\ 1, \text{ if } T_d + QRS_d \leq t \leq T_r \\ (1 - \dfrac{t - T_r}{QRS_d}), \text{ if } T_r \leq t \leq T_r + QRS_d \\ 0, \text{ otherwise} \end{cases} \\
|u|_+ &= k_{ATP}.f_{depo} \\
|u|_- &= k_{RS}.(1 - f_{depo}),
\end{aligned} \tag{3.11}
$$

The model is implemented in C and the system of equations is solved by using the forward Euler method with a dt of 1 ms. The 0D model is also available in CellML through the software OpenCOR. The default values for the model parameters can be found in Table 3.1.

3.3.2 Biophysics-based statistical learning

In general the mechanistic model, ψ, consists of a set of ordinary differential equations with n_ψ parameters (e.g. maximum contraction of the heart fibres or its stiffness), while the state variables of the model are denoted by O (e.g. arterial or venous pressures). Formally, during the personalisation stage, a subset of n_t state variables or *target features* from the data, $\hat{O} = (\hat{O}_1, \hat{O}_2, ..., \hat{O}_{n_t})$ are used to optimise a subset θ of the n_ψ model parameters. We denote $O(\theta)$ the set of state variables generated by the model for a given set of θ. The goal is to find θ^* such that $O(\theta^*)$ best approximates the target features $\hat{O}$. This optimisation procedure can be expressed as in Equation 3.12:

$$
\begin{aligned}
\frac{dO}{dt} &= \psi(\theta, t), \\
\hat{O} &\leftarrow O(\theta^*)
\end{aligned} \tag{3.12}
$$

Tab. 3.1.: Default values of the cardiovascular model's parameters. The varying parameters are set in bold.

Left heart	Value	Right heart	Value	Concept
$Heart\ period\ [s]$	0.8	$Heart\ period\ [s]$	0.8	Heart period
$\alpha\ [a.u]$	1.5	$\alpha\ [a.u]$	1.5	Cross-bridge destruction upon rapid length changes
$w\ [a.u]$	1	$w\ [a.u]$	1	Length-dependent relaxation
$n_0\ [a.u]$	1	$n_0\ [a.u]$	1	Length-dependent fraction of myosin heads
$k_0\ [Pa]$	$1 \cdot 10^5$	$k_0\ [Pa]$	$1 \cdot 10^5$	Sarcomere stiffness
$\boldsymbol{\sigma_0\ [Pa]}$	$\mathbf{6.4 \cdot 10^4}$	$\sigma_0\ [Pa]$	$6.4 \cdot 10^4$	Maximum sarcomere active stress (Contractility)
$k_{ATP}\ [s^{-1}]$	30	$k_{ATP}\ [s^{-1}]$	30	Speed of sarcomere force build-up (ATP rate)
$k_{rs}\ [s^{-1}]$	30	$k_{rs}\ [s^{-1}]$	30	Speed of sarcomere force decrease (Relaxation rate)
$APD\ [s]$	0.30	$APD\ [s]$	0.30	Action potential duration
$AV\ delay\ [s]$	0.12	$AV\ delay\ [s]$	0.12	Atrioventricular delay
$QRS\ duration\ [s]$	0.085	$QRS\ duration\ [s]$	0.085	QRS duration
$\boldsymbol{R_0\ [m]}$	**0.028**	$R_0\ [m]$	0.028	Ventricular resting radius
$d_0\ [m]$	0.014	$d_0\ [m]$	0.007	Ventricular wall thickness
$\rho\ [kg.m^{-3}]$	1070	$\rho\ [kg.m^{-3}]$	1070	Myocardial mass density
$E_s\ [Pa]$	$3 \cdot 10^7$	$E_s\ [Pa]$	$3 \cdot 10^7$	Ventricular elastance
$\mu\ [Pa.s]$	70	$\mu\ [Pa.s]$	70	Active viscous damping
$\boldsymbol{c_1\ [Pa]}$	**1000**	$c_1\ [Pa]$	1000	Mooney-Rivlin material parameter (Stiffness)
$c_2\ [Pa]$	1000	$c_2\ [Pa]$	1000	Mooney-Rivlin material parameter (Stiffness)
$\eta\ [Pa.s^{-1}]$	100	$\eta\ [Pa.s^{-1}]$	100	Global damping
$P_{at\_t1}\ [s]$	0.005	$P_{at\_t1}\ [s]$	0.005	Start of atrial systole
$P_{at\_t2}\ [s]$	0.1	$P_{at\_t2}\ [s]$	0.1	Time peak of atrial systole
$k_{at}\ [m^3.s^{-1}.Pa^{-1}]$	$9 \cdot 10^{-6}$	$k_{at}\ [m^3.s^{-1}.Pa^{-1}]$	$9 \cdot 10^{-6}$	Atrioventricular valve resistance
$k_{ar}\ [m^3.s^{-1}.Pa^{-1}]$	$1.3 \cdot 10^{-5}$	$k_{ar}\ [m^3.s^{-1}.Pa^{-1}]$	$1.3 \cdot 10^{-5}$	Arterial valve resistance
$k_{iso}\ [m^3.s^{-1}.Pa^{-1}]$	$1 \cdot 10^{-37}$	$k_{iso}\ [m^3.s^{-1}.Pa^{-1}]$	$1 \cdot 10^{-37}$	Atrioventricular valve leakage
$\boldsymbol{\tau\ [s]}$	**0.8**	$\tau\ [s]$	0.8	Windkessel time constant ($\tau = R_p C_{ar}$), where, C_{ar} is the aortic compliance
$\boldsymbol{R_p\ [Pa.m^{-3}.s]}$	$\mathbf{2.5 \cdot 10^7}$	$R_p\ [Pa.m^{-3}.s]$	$1 \cdot 10^7$	Peripheral resistance
$Z_c\ [Pa.m^{-3}.s]$	$5 \cdot 10^6$	$Z_c\ [Pa.m^{-3}.s]$	$5 \cdot 10^5$	Proximal resistance
$dt\ [s]$	$1 \cdot 10^{-5}$	$dt\ [s]$	$1 \cdot 10^{-5}$	Time-step
$V0_{at}\ [m^3]$	0	$V0_{at}\ [m^3]$	0	Initial atrial volume
$E_{at}\ Upper\ [Pa.m^{-3}]$	$2.2 \cdot 10^7$	$E_{at}\ Upper\ [Pa.m^{-3}]$	$2.2 \cdot 10^7$	Maximum atrial elastance
$E_{at}\ Lower\ [Pa.m^{-3}]$	$1 \cdot 10^7$	$E_{at}\ Lower\ [Pa.m^{-3}]$	$1 \cdot 10^7$	Minimial atrial elastance
$P_{at\_t3}\ [s]$	0.2	$P_{at\_t3}\ [s]$	0.2	End of atrial systole
Systemic veins	**Value**	**Pulmonary veins**	**Value**	**Concept**
$R_{ven}\ [Pa.m^{-3}.s]$	$2.5 \cdot 10^7$	$R_{ven}\ [Pa.m^{-3}.s]$	$5 \cdot 10^6$	Venous resistance
$C_{ven}\ [m^3.Pa^{-1}]$	$5 \cdot 10^{-6}$	$C_{ven}\ [m^3.Pa^{-1}]$	$5 \cdot 10^{-5}$	Venous compliance
$P_{ven}\ [Pa]$	3200	$P_{ven}\ [Pa]$	1700	Venous pressure

We carried out the personalisation through the evolutionary strategy CMA-ES (covariance matrix adaptation evolution strategy), which is a gradient-free approach based on maximum likelihood estimate of the parameters [Hansen, 2016]. At each iteration CMA-ES evaluates several candidate solutions and assigns to each one a score, in this case the personalisation error. Based on the score ranks, a subset of best performance solutions is used to update the sampling distribution of the parameter-space. This allows CMA-ES to explore the parameter-space while being robust to possible divergences leading to non-valid sets of parameters, in which the score can be arbitrary high. At the same times it makes CMA-ES well suited to parallel environments, since we can evaluate several solutions independently.

We denote as $S(\theta, \hat{O}, Tol)$ the error function that we want to minimise, defined as the L_2 distance between $O(\theta)$ and $\hat{O}$. Since each target feature has different range of values to

compare the different outputs for each feature f a tolerance interval (Tol) is defined, which can be formalised as:

$$S(\theta, \hat{O}, Tol) = \sum_{f=1}^{n_t} \frac{(O_f(\theta) - \hat{O}_f)^2}{Tol_f} \tag{3.13}$$

Following the method of iterative updated priors (IUP) [Molléro, 2018] group-wise constraints can be introduced during the optimisation process to obtain consistent solutions at population level, tackling the identifiablity problem. In the IUP method a regularisation term, $R(\theta, \mu, \Sigma)$, is used to reduce the variability in the estimation of the parameters. This regularisation constraints the directions in which the parameter-space is explored by leveraging on the relationships among model parameters. Formally, the estimated regularisation term is parameterised by an expected value μ and by a covariance matrix Σ encoding the relationship across parameters:

$$R(\theta, \mu, \Sigma) = (\theta - \mu)^T \Sigma^{-1} (\theta - \mu). \tag{3.14}$$

Therefore, the error function becomes:

$$S(\theta, \hat{O}, \mu, \Sigma, Tol) = S(\theta, \hat{O}, Tol) + \gamma R(\theta, \mu, \Sigma), \tag{3.15}$$

where γ defines the relative weight of the regularisation term. This term is updated at each IUP iteration using the obtained mean value of the fitted parameters and the estimated covariance in the previous iteration.

The regularisation term $R(\theta, \mu, \Sigma)$ can be extended to incorporate features not present in the cardiovascular model. The extended feature space corresponds to the concatenation of the model parameters, θ, with *external features*, ϕ, which represent other available subject's information such as volumetric indices extracted from brain scans, or weight and height as in [Molléro, 2018]. In this work, we incorporated volumetric features extracted from brain images such as whole brain and ventricle volumes, WMHs features, as well as age and body surface area (BSA). Let μ_ϕ and Σ_ϕ denote the mean of the external features and their covariance respectively. Then, $\Sigma_{i,\phi}$ corresponds to the cross-covariance between the external features and the model parameters. Therefore, the error function to be minimised in Equation 3.15 becomes:

$$S(\theta, \hat{O}, \mu^*, \Sigma^*, Tol) = S(\theta, \hat{O}, Tol) + \gamma R(\theta, \mu^*, \Sigma^*), \tag{3.16}$$

$$\mu^* = \begin{bmatrix} \mu_i \\ \mu_\phi \end{bmatrix}, \ \Sigma^* = \begin{bmatrix} \Sigma_i & \Sigma_{i,\phi} \\ \Sigma_{\phi,i} & \Sigma_\phi \end{bmatrix}. \tag{3.17}$$

Equation 3.16 now accounts for a covariance term constraining the parameters according to the extended set of features.

By default CMA-ES initially samples solutions according to a standard multivariate Gaussian distribution, which is updated at each sampling iteration based on the best-performance solutions of the previous one, parameters are supposed to have similar sensitivity to properly explore the parameter-space in all directions. To promote this behaviour, we introduced for each subject s a mean and a covariance hyper-parameters, m_{si} and C_{si} respectively, which are updated at each IUP iteration. These additional hyper-parameters allow to account for the different sensitivity of the model parameters during optimisation, and promote a more accurate exploration of the parameter space through sampling. Both mean and covariance are computed using the sampled solutions of CMA-ES, $\hat{x}_s$, at the iteration in which we get the optimal set of parameters θ_s^*. The individual mean and covariance are used to scale the solutions, $\hat{x}_s$, into the actual model's parameter range, according to $\theta_s = \hat{x}_s * C_{si}^{1/2} + m_{si}$.

A scheme illustrating the personalisation of the cardiovascular lumped model with subject's brain and heart data is shown in Figure 3.1; pseudo-codes for the IUP and the scaled CMA-ES are shown in Algorithm 1 and Algorithm 2 respectively.

3.4 Application to brain and heart data

3.4.1 Clinical data and pre-processing

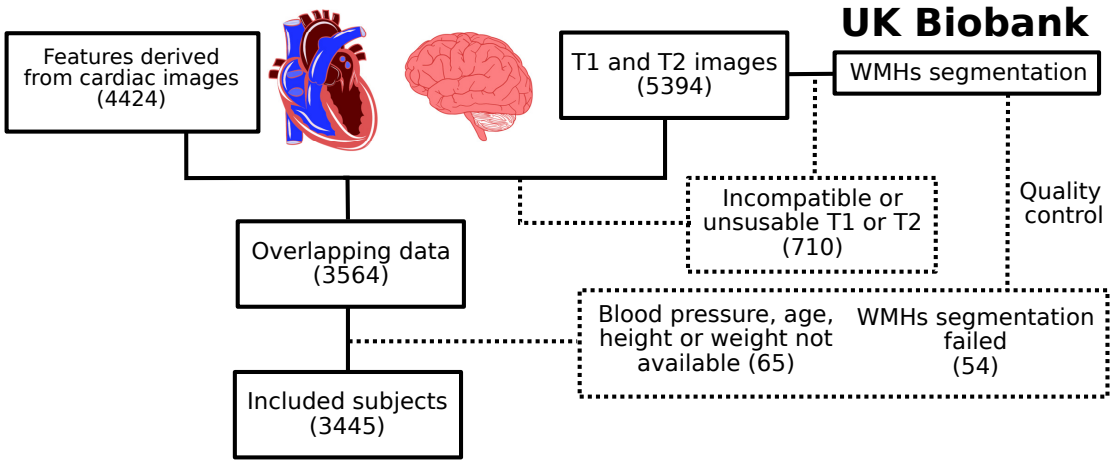

Fig. 3.2.: Schematic representation of the inclusion criteria used in our study.

Algorithm 1 IUP pseudo-code.

Inputs:
  N subjects with n_t target features ($\hat{O}$) and n_e external features (ϕ)
  $k \leftarrow$ IUP iterations
  $Tol \leftarrow$ Tolerance interval
  $CMA_{options}$
Returns:
  $\theta^*, \mu^*, \Sigma^*, C, m$
Initialise:
  $\Sigma_\phi, \mu_\phi \leftarrow$ external features
  $i \leftarrow 0$

while $i < k$ **do**
  if $i == 0$ **then**
    Initialise parameter prior covariance (Σi) and mean (μ_i) as null values
  end if
  $\mu_i^*, \Sigma_i^* \leftarrow$ Extend prior terms as in Equation 3.17
  for $s \leftarrow 1$ **to** N **do**
    $\theta_{si}^*, C_{si}, m_{si} \leftarrow$ Scaled-CMA($CMA_{options}$, Tol, μ_i^*, Σ_i^*, C_{si}, m_{si})
  end for
  $\mu_{i+1} \leftarrow$ mean of the $\{\theta_{si}^*\}_{s=1}^N$
  $\Sigma_{i+1} \leftarrow$ covariance of the $\{\theta_{si}^*\}_{s=1}^N$
  $i \leftarrow i + 1$
end while

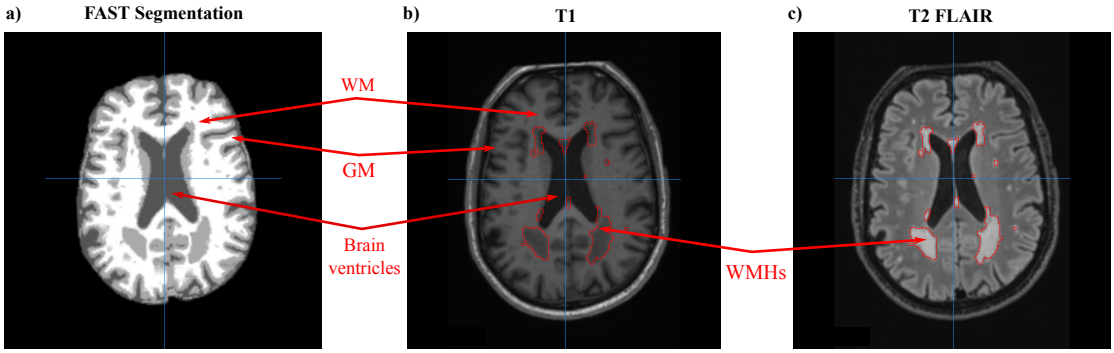

Fig. 3.3.: Example of the available brain volumetric information for each subject. a) Segmentation of the main brain tissues, white matter (WM), grey matter (GM) and brain ventricles using the FAST algorithm of FSL [Zhang, 2001]. Image processing was carried out using the pipeline described in [Alfaro-Almagro, 2018]. b) T1 sequence and c) T2 FLAIR MRI sequence with WMHs segmentation overlaid, carried out using the LPA toolbox for SPM

The UK Biobank database provides demographic information (e.g. age, sex, height or weight) and clinical measurements such as brachial blood pressures (both diastolic and systolic; DBP and SBP respectively), image-derived features from both brain and cardiac MRI, clinical diagnoses and several MRI modalities of the brain.

For our analysis we selected a subset of subjects for which brain T1 and T2 FLAIR MRI modalities were labelled as usable for segmentation and all cardiac-image derived indices

Algorithm 2 Scaled CMA optimization pseudo-code.

Inputs:
  Tol
  μ^*, Σ^*, C_s, m_s
  $CMA_{options}$
Returns:
  θ^*, C_s, m_s
Initialise:
  $S_s^{best} \leftarrow inf$
while $j < CMA_{iterations}$ **do**
  if m_s is null **then**
    Initialise subjects covariance (C_s) and mean (m_s) with parameters default values
  end if
  $\hat{x}_s \leftarrow$ sample from CMA ($CMA_{options}$)
  $\theta_s = \hat{x}_s * C_s^{1/2} + m_s$
  $S_s = S(\theta_s, \hat{O}_s, \mu^*, \Sigma^*, Tol)$ Evaluate solutions
  if $min(S_s) < S_s^{best}$ **then**
    $S_s^{best} = \min(S_s)$
    $\theta_s^{best} \leftarrow \theta_s$
    $\theta_s^* = \arg\min_{S_s}(\theta_s)$
  end if
  if $S_s^{best} < C_{th}$ **then**
    break
  end if
end while
$m_s \leftarrow$ mean of θ_s^{best}
$C_s^{1/2} \leftarrow$ square root of the covariance of θ_s^{best}

were available, for a total of 3564 subjects (see Figure 3.2). The cardiac indices were extracted from the segmentation of the left ventricle in short-axis cine images, including SV, EDV, ESV, CO and EF. Using T1 and T2 FLAIR MRI, WMHs were segmented using the lesion prediction algorithm (LPA) [Schmidt, 2017], available in the lesion segmentation toolbox (LST) of SPM[1]. From the resulting segmentations we extracted the total volume of WMHs and number of lesions. Other volumetric indices such as the total grey matter (GM), white matter (WM) and brain ventricles volumes were obtained from the T1 MRI according to the protocol described in [Alfaro-Almagro, 2018]. All brain-related volumes (including WMHs) were normalised by head size. The WMHs total volume and number of lesions presented a positive skewed distribution; in order to obtain a more suitable distribution for our statistical approach we used the Box-Cox transformation to normalise the distributions.

According to [Ribaldi, 2018] the obtained WMHs volumes using the LPA are comparable to the ones obtained through manual segmentation. Nevertheless, for each subject the segmentation of WMHs was visually assessed and the non-acceptable ones were excluded.

[1] https://www.fil.ion.ucl.ac.uk/spm

Moreover, subjects for which one of the demographic features of interest (age, sex, height or weight) or blood pressure were not available were also discarded. The final number of available subjects was 3445. Height and weight were used to compute the body surface area (BSA) of each subject according to Mosteller formula [Mosteller, 1987]: $BSA = \sqrt{\frac{Weight[kg]*Height[cm]}{3600}}$. Summary statistics of the dataset are provided in Table 3.2, and Table 3.3 provides the corresponding data-field codes from the UK Biobank.

Tab. 3.2.: Statistics of the analysed UK Biobank dataset, including AF and control subjects. Bold features are significantly different between AF and a randomly sampled representative control group (two-sample t-test, $p \leq 0.05$) when Bonferroni correction is not applied. The control group was sampled to match on Age, Sex and BSA. The volume of WMHs and the number of WMHs were normalised using the Box-Cox transformation.

	UK Biobank	**Atrial Fibrillation**	**Sample Control**
Subjects (M/F)	1555/1890	45/14	42/17
	Mean ± Std	**Mean ± Std**	**Mean ± Std**
Age $(Years)$	61.07 ± 7.12	65.79 ± 6.86	64.54 ± 4.62
BSA (m^2)	1.88 ± 0.21	2.02 ± 0.20	1.97 ± 0.17
DBP $(mmHg)$	75.49 ± 12.10	75.67 ± 12.29	77.64 ± 12.69
SBP $(mmHg)$	132.09 ± 18.77	133.15 ± 19.52	139.12 ± 20.34
MBP $(mmHg)$	94.35 ± 13.12	94.83 ± 13.30	98.13 ± 13.84
SV (ml)	77.58 ± 17.70	76.08 ± 20.65	77.1 ± 18.77
EDV (ml)	138.95 ± 32.6	152.86 ± 32.84	142.96 ± 33.23
ESV (ml)	61.37 ± 19.85	76.72 ± 25.81	65.79 ± 19.46
EF $(\%)$	56.21 ± 6.24	50.28 ± 10.16	54.23 ± 7.74
WM (mm^3)	711,454 ± 40,719	701,887 ± 43,838	711,360 ± 46,615
GM (mm^3)	801,685 ± 46,702	763,876 ± 48,842	788,936 ± 43,348
Ventricles (mm^3)	42,807 ± 17,612	55,103 ± 21,930	45,925 ± 16,705
WMHs $(a.u)$	7.5 ± 2	8.64 ± 2.12	7.51 ± 1.91
# WMHs $(a.u)$	3.27 ± 0.85	3.73 ± 0.83	3.41 ± 0.79

We used as target features EDV, SV, EF, MBP and DBP. ESV was discarded from the volumetric features since it did not provide additional information concerning the selected features. While, among the available pressure information MBP and DBP were used since we did not have pressure information at the aorta level, and unlike SBP, both MBP and DBP exhibit similar values in the main systemic arteries [Muiesan, 2014]. Based on previous experience [Molléro, 2018] and on the available data, the most sensitive parameters were selected to enter the personalisation procedure: the contractile and elastic behavior of the left ventricles (σ_0, R_0, C_1) and parameters related to the systemic vasculature properties (R_p, τ). Moreover, heart rate information obtained during the cardiac MRI was used to determine the heart period of the model for every subject. For the volumetric features (SV, EDV) we set a tolerance interval of 10 ml, 200 Pa for pressures (MBP, DBP), and 5% for the EF, based on the clinical uncertainty of these values. This tolerance interval was used to assess the convergence of the model. As initial values for the varying parameters we used the model default values (see Table 3.1). After personalisation we used the Spearman's rank coefficient to study the associations

Tab. 3.3.: UK Biobank data-fields corresponding to the used data. In all the cases the data timepoint was 2.0, corresponding to the first imaging visit.

Data	Code
Sex	31
Age attended centre	21003
Standing Height	50
Weight	21002
DBP automated	4079
SBP automated	4080
Left ventricle SV	22423
Left ventricle EDV	22421
Left ventricle ESV	22422
Left ventricle EF	22420
Volume WM normalized	25007
Volume GM normalized	25005
Volume Ventricles normalized	25003

Tab. 3.4.: List of considered cardiovascular diseases, their correspondent ICD10 codes, and number of cases in the available dataset.

Disease	Code	Cases
Stroke	I60, I61, I63, I64	7
Hyperlipidemia	E78	183
TIA	G45	13
Myocardial infarction	I21, I22, I23	37
Atrial fibrillation	I48	59
Heart failure	I50	15
Peripheral vascular disease	I73, I74	9
Venous thromboembolism	I26, I80, I81, I82	24
Aortic stenosis	I350	0
Hypertension	I10, I11, I12, I13, I14, I15	396
Atherosclerosis	I70	4
Aortic aneurysms	I71	1
Other aneurysms	I72	1
Other cerebrovascular	I62, I65, I66, I67, I68, I69, G46	11

between the estimated model parameters and the external features. The number of IUP iterations and the hyper-parameters of the CMA-ES algorithm were determined empirically as: population size (20), number of iterations (100), initial variance (0.1)

and 5 IUP iterations. We applied the framework to the available UK Biobank cohort and used the results to assess the model plausibility, next we applied the framework to a subgroup of subjects diagnosed with AF.

3.4.2 UK Biobank

We run our framework in the whole available cohort (3445 individuals) and studied the associations between external features, target features and varying model parameters, as well as the parameter's distribution at each IUP iteration, convergence rate and error between the target features and the simulations. We also considered five regularisation levels $\gamma = (0.1, 0.5, 1, 2, 10)$, and the presence or not of the external features in the regularisation term.

3.4.2.1 Model plausibility

To assess the influence of the external features included in the covariance matrix of our prior we simulated a scenario in which only DBP and MBP were available while inferring all the varying parameters, i.e. where the volumetric information was missing (SV, EDV, EF). Hence, we selected a subset of 100 random subjects and run one IUP iteration using as regularisation term the final prior learnt in the whole cohort with and without external features. Then, we assessed the difference between the values of the estimated parameters for these subjects with respect to the ones obtained when all the target features were available, and the missing target features were compared to the model's simulations. We measured the differences using the Mahalanobis distance, $D_M(x, y) = \sqrt{(x-y)^T \Sigma^{-1} (x-y)}$, where Σ represents respectively the covariance matrix of the missing target features when compared to the simulated ones, and the covariance matrix of the estimated parameters with all the target features when the model's parameters are compared.

In Figure 3.4a we observe the distance between the missing target features (EDV, EF, SV) and the ones simulated by the model. We observe that while regularisation helps to reduce the error for values of $\gamma \leq 1$, the tendency changes when $\gamma > 1$. The use of external features in the prior reduces this discrepancy, although not significantly. Figure 3.4b demonstrates that with an increased regularisation the distance between the parameter's values estimated using a subset of the target features and the ones obtained using all of them is reduced. Moreover, in this case the difference is significant. Hence, the presence of the external features allows to learn a more meaningful representation of the parameter-space. Based on these observations, the results of the following sections were obtained by setting $\gamma = 1$ and using external features.

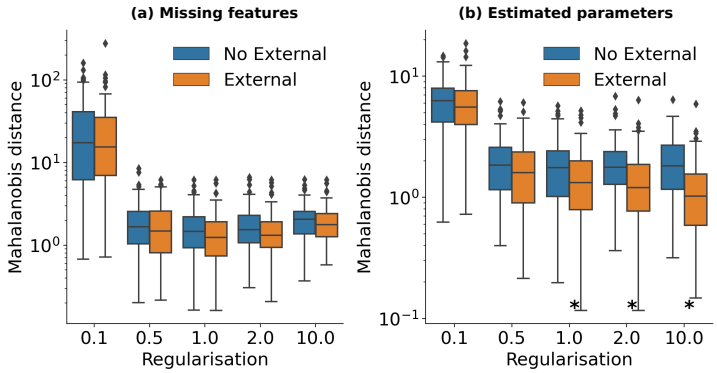

Fig. 3.4.: Mahalanobis distances between: a) missing features and simulated results of the model. b) the estimated parameters with missing features and the estimated parameters with all target features. * denotes that distributions are significantly different according to Wilcoxon rank-sum test using a significance level of $\alpha = 0.05$. The y-axis is represented in log-scale.

3.4.2.2 Analysis of brain-cardiac relationship in the UK Biobank

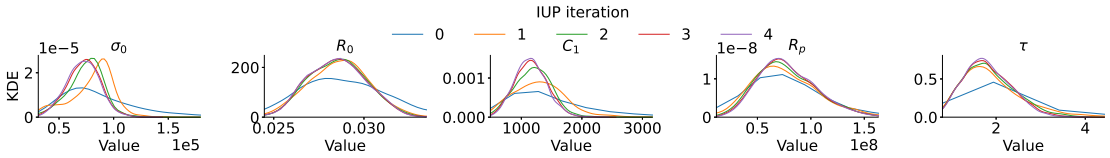

Fig. 3.5.: Kernel density estimates (KDE) of the fitted parameters at each IUP iteration with external constraints and $\gamma = 1$. Note that the distributions are not enforced to be Gaussian, each solution is independently sampled using CMA-ES and certain directions are penalised by the regularisation.

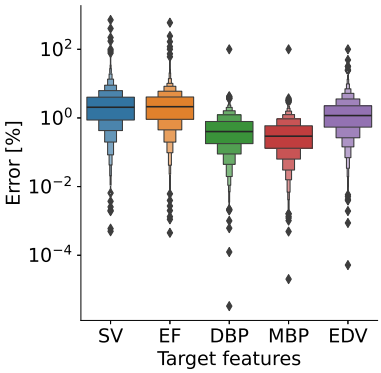

Fig. 3.6.: Absolute reconstruction errors as a percentage of the target features values. The y-axis is represented in log-scale.

Figure 3.5 shows the parameters distribution at each IUP iteration. We can observe how at each IUP iteration the distribution of the estimated parameters shrinks with increasing regularisation, reducing the number of outliers and extreme values. The regularisation term penalises the exploration of certain directions in the parameter-space based on the available information. At the same time, the median absolute error as a percentage of the target features stays around 5% as can be seen in Figure 3.6. Moreover, the majority of the studied subjects (90.39%) reached convergence according to our tolerance interval,

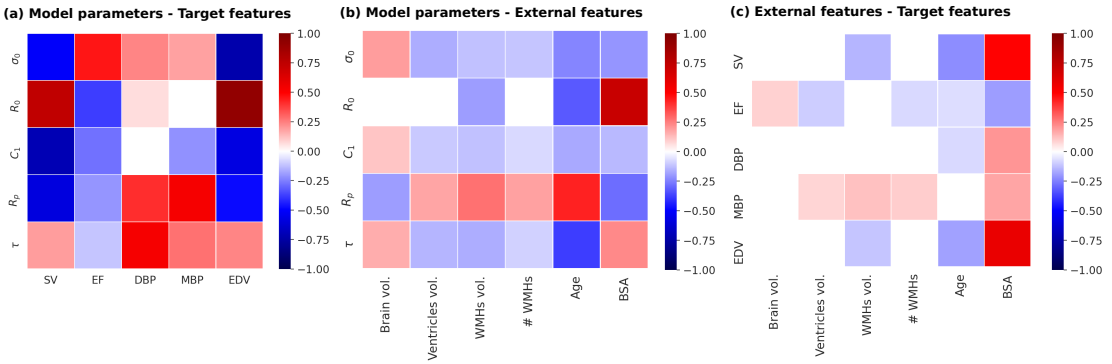

Fig. 3.7.: Correlations heatmap between features and model parameters. The associations have been assessed by means of Spearman's rank correlation coefficient and corrected for multiple comparison using the Bonferroni's method. Non-significant correlations are considered as 0 (white). a) Associations between target features and model parameters b) relationships between the model parameters and the external features c) correlations between target features and external features.

Tol. Finally, Figure 3.7 shows the Spearman's rho correlations among the external features, the model's parameters and the target features. Several observations can be made from the figure:

1. Model parameters - Target features: We observe how the radius of the left ventricle, R_0, is strongly correlated with the end-diastolic volume, slightly less with the stroke volume, and negatively with the EF. The peripheral resistance, R_p, is correlated with the pressure indices, DBP and MBP, and inversely related to the end-diastolic volume and the stroke volume. The compliance of the main arteries, τ, is closely related to the diastolic pressure, and affects in the opposite way the systolic pressure, affecting the relationship between the mean and the diastolic pressure. The contractility σ_0 is strongly correlated with the EF and inversely with the end-diastolic volume and the stroke volume, while the stiffness of the heart, C_1, affects negatively the EF, the end-diastolic volume and the stroke volume.

2. External features - Target features: The relationship between target features and external features is mostly negligible. We only observe a strong positive associations between the heart volumetric indices (EDV, SV) with BSA, and a negative one with respect to age.

3. Model parameters - External features: We observe how the left ventricle contractility, σ_0, is positively correlated with brain volume and negatively with the rest of volumetric indices, such as ventricles volume and WMHs. The same behaviour is observed in the relationships of C_1. The radius of the left ventricle, R_0, is inversely related to age, WMHs volume and positively with BSA; for the remaining indices it does not show any significant association. The peripheral resistance, R_p, shows a positive association with WMHs volume, number of WMHs, brain

ventricles volume and age and negative with brain volume and BSA. The main arteries characteristic time, τ, which is proportional to the arterial compliance, shows the opposite relationships.

The results show an expected association between larger heart ventricles, R_0, and greater blood volumes such as the end-diastolic volume [Jegier, 1963]. Also we observe how an increase in peripheral resistance, R_p, leads to an increase in afterload (DBP and MBP) and a reduction of preload (EDV). Unlike the peripheral resistance, R_p, the arterial compliance, τ, shows a different strength of association with both MBP and DBP. Hence, τ modifies the dependence of the mean pressure on the diastolic pressure and increases the relative importance of the systolic pressure, which indicates the opposite effect of τ in SBP. Indeed, an increase in peripheral resistance can be associated to higher DBP, while a decrease in arterial compliance leads to high SBP, both effects have been associated to a higher burden of WMHs [Modir, 2012; Moroni, 2018]. The reduction of the left ventricle radius, R_0, has been associated to age [Akasheva, 2015], as well as to the increase of peripheral resistance and arterial stiffening [Jani, 2006]. The association between contractility, σ_0, and EF was also expected [Downey, 2001], since contractility modulates the SV by changing the ESV, which modifies the EF. However, we observed a negative association between σ_0 and SV, while we would expect a positive one. This can be explained by the fact that other parameters, such as the left ventricle radius, (R_0), also affect the estimation of the SV and are inversely related to σ_0. Nevertheless, the main role of σ_0, the modulation of the EF, is still consistent with the expected model behavior and prior knowledge.

3.4.2.3 Uncertainty Analysis

For each individual considered in this analysis we assessed the uncertainty in the parameter's estimation using the covariance and the mean of the sampling distribution of the CMA-ES obtained at the last iteration of the IUP algorithm. In addition, we performed a sensitivity analysis to assess how this uncertainty propagates to the target features, and how it affects the relationship between the external features and the estimated parameters. The adopted procedure is as follows. For each subject we sampled 100 solutions, computed the fitting errors and assessed the correlations between the model parameters and the external features. The parameter's uncertainty was quantified by the standard deviation as a percentage of the mean value, while the fitting errors by the absolute error as a percentage of the target values. Table 3.5 summarises the obtained results. The median uncertainty in the parameters estimation is around 5% for every parameter and the highest upper quartile is close to 10%. Based on the estimated uncertainty of the fitting errors, we observe how solutions sampled around the selected hyper-plane in the parameter-space lead to reasonable solutions, the highest upper quartile for the mean error is below 7.5%, and below 5% for the standard deviation. Finally, Figure 3.8 shows

the average correlations between the model parameters and the external features and their standard deviation. We can see how the average results match the ones presented in Figure 3.7b, while the standard deviation of the relationships is low, showing their stability.

Tab. 3.5.: We sampled 100 solutions for every subject by using their respective sampling distribution obtained by the CMA-ES optimisation at the last IUP iteration. Fitting errors quantified by means of the absolute error as a percentage of the target features. The target features are: stroke volume (SV), ejection fraction (EF), mean blood pressure (MBP), diastolic blood pressure (DBP) and end-diastolic volume (EDV). The uncertainty in the parameter's estimation is assessed by means of the standard deviation as percentage of the mean value. The standard deviation and the mean were obtained from the sampling distribution of the CMA-ES. The sampled parameters are: contractility (σ_0), ventricle radius (R_0), stiffness (C_1), peripheral resistance (R_p) and arterial compliance (τ). All the results are reported using the median and the interquartile range.

Fitting errors			Parameters uncertainty	
Target feature	Mean	Standard Deviation	Parameter	Standard Deviation
SV	4.39 (2.49-7.35)	2.44 (1.36-4.41)	σ_0	4.53 (2.48-7.79)
EF	3.97 (2.26-6.35)	1.91 (1.06-3.25)	R_0	0.81 (0.41-1.50)
MBP	0.85 (0.48-1.50)	0.54 (0.29-1.02)	C_1	5.44 (2.86-9.62)
DBP	1.02 (0.58-1.73)	0.61 (0.34-1.11)	R_p	6.25 (3.34-10.86)
EDV	3.18 (1.84-5.48)	2.01 (1.11-3.57)	τ	4.32 (2.39-7.10)

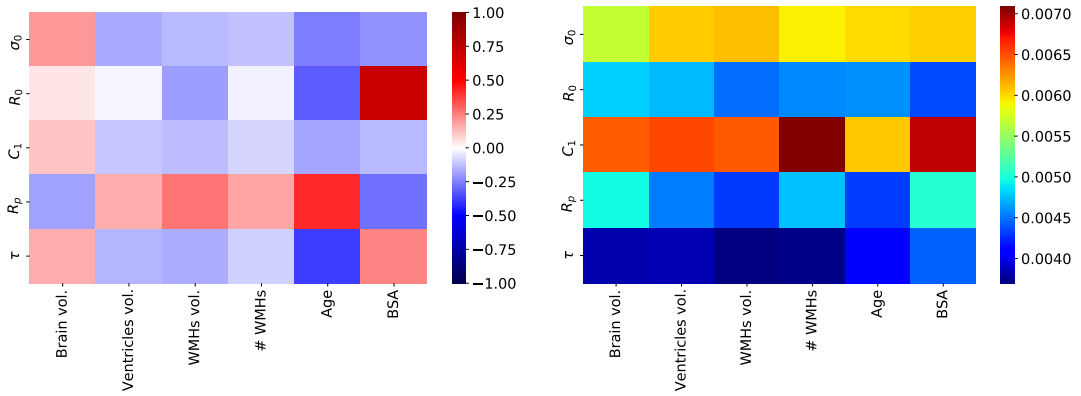

(a) Mean **(b) Standard Deviation**

Fig. 3.8.: We sampled 100 solutions for every subject by using their respective sampling distribution obtained by the CMA-ES optimisation at the last IUP iteration. a) Average correlations between model parameters and external features b) Standard deviation of the correlations. The average correlation matches the one presented in Figure 3.7b and the low variability seen in the standard deviation highlights the robustness of the estimated associations.

.

3.4.3 AF subgroup analysis

Considering the dataset obtained after the pre-processing steps described in Section 3.4.1 we obtained 59 subjects diagnosed with AF. We analysed two aspects of this subgroup with respect to the population of healthy controls: 1) if there are significant differences in the correlations between the model parameters and the external features, and 2) if there are significant differences between the estimated model parameters between groups. Compatibly with the experiments shown in the previous section, we assessed these aspects through bootstraping of 100 training sets, composed by the 59 AF subjects and by a random control group matched with the AF sub-cohort without significant differences in age, sex and BSA, adding up to 118 subjects per training set. Each control group was sampled without replacement from the subset of subjects without any of the cardiovascular diseases listed in Table 3.4 ($n = 2892$). Through this approach we can take into account the variability present in the whole personalisation process and in the healthy population. Furthermore, we assessed the significance for the differences between AF and controls, we created a sampling population composed of all the solutions obtained in the 100 training sets. Then, we estimated a null distribution of differences between randomly sampled groups with sample size corresponding to the ones of AF and controls groups respectively. This distribution allows us to quantify the distribution of the observed difference when the underlying difference between the groups is actually zero. Hence, we statistically assessed the significance of the observed difference between the AF and the control groups by comparison with the null distribution using a significance level of $\alpha = 0.05$. The results presented in Table 3.6 show that there is a significant difference in their contractility, σ_0, while other parameters such as the peripheral resistance, R_p, or the left ventricle size, R_0, are close to significance.

Tab. 3.6.: Results from the bootstrap analysis used to compare the AF and the control groups. The null-distribution for the difference was obtained by sampling with replacement 10,000 times two random groups with samples sizes matching those of of AF and control groups. We evaluated if the difference between the AF group and the control groups was significant according to a significance level of $\alpha = 0.05$. The significant features are set in bold.

Parameter	σ_0	R_0	C_1	R_p	τ
p-value	**0.03**	0.15	0.12	0.086	0.96

Moreover, the results from the 100 training sets allowed us to obtain an empirical distribution of the correlations between cardiac and external parameters. We assessed the differences between controls and AF groups using the Wilcoxon rank-sum test and considered them significant when one of the distributions was significantly greater or smaller than 0. All the tests were performed using a significance level of $\alpha = 0.05$ adjusted using Bonferroni correction for 30 comparisons in total, accounting for the comparisons between the model parameters (5) and their association with the external features (6).

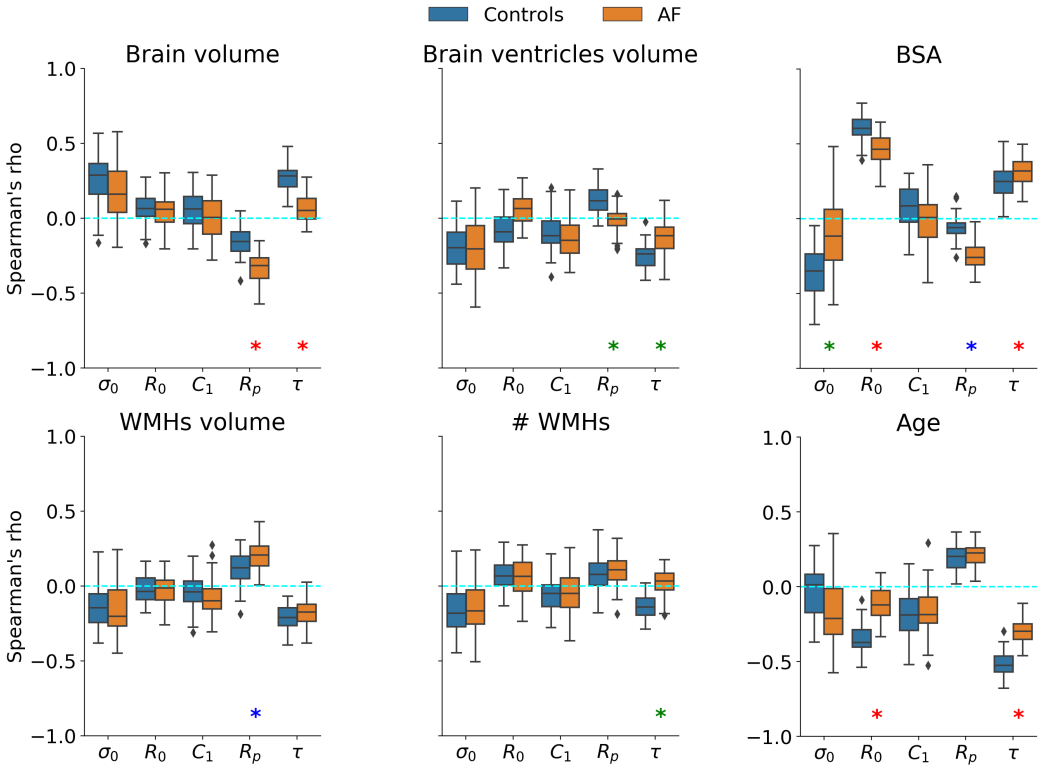

Fig. 3.9.: Comparison of the bootstrap distributions of the Spearman's rank correlation coefficient obtained at regularisation $(\gamma) = 1$ between the personalised model parameters and the external features. Blue box-plots correspond to control groups and orange to AF subjects. $*$ denotes that the correlations are significantly different according to the Wilcoxon rank-sum test. In red both group correlations are significantly greater or smaller than 0 and there is change in the magnitude of the association. In blue the control group is not significantly greater or smaller than 0 and the AF group it is, so it represents a new association. In green we denote the opposite case, representing lost associations. All tests performed with a 5% significance level adjusted using Bonferroni correction.

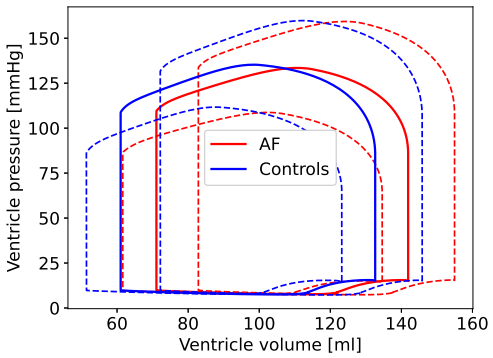

Fig. 3.10.: Pressure-volume (PV) loop comparison between AF (orange) and controls (blue). Solid lines (PV) represent the average loop and dashed lines the standard deviation.

Figure 3.9 reports the empirical distribution of correlations obtained from the analysis performed in the AF subset. When distributions were statistically different we considered three different scenarios:

1. Change in magnitude (red): the control and AF distributions are significantly different from 0;

2. AF association (blue): only the AF group is significantly different from 0;

3. Control association (green): only the control group is significantly different from 0.

In the control group we can observe a pattern of associations similar to the one found in the whole-cohort analysis: brain volume is correlated with the contractility, σ_0, and the arterial compliance, τ, while it is inversely associated to the peripheral resistance, R_p. The inverse pattern is seen in the other brain indices (volume and number of WMHs and ventricles volume) and age. On the other hand, the BSA is associated to the left ventricle radius, R_0, and with lower contractility. In the AF group the differences are mainly found in the associations involving the aortic compliance, τ, and the peripheral resistance, R_p. Compared to the control groups τ loses its association with whole brain volume, ventricles volume, and with the number of WMHs. At the same time, the association between R_p and the total volume of WMHs becomes significant, the one with brain volume gets stronger, while the relationship with brain ventricles volume is lost. Furthermore, the association between age and the size of the left ventricle, R_0, is lost and the one with the arterial compliance decreases in magnitude. Regarding BSA we observe how the association with the left ventricle size gets weaker, the one with the arterial compliance stronger, a new one with peripheral resistance appears and the one with the contractility, σ_0, disappears. Figure 3.10 illustrates the differences in the modeled PV loop between the average AF subject and the average control subject. In the AF subjects it can be appreciated an increased end-diastolic volume and decreased end-systolic pressure volume relationship, indicating a decreased contractility, σ_0, increased afterload, and a dilated ventricle.

The observed differences between AF and control subjects may be the result of several pathological processes. Recently some studies have proposed different mechanisms through which AF may promote cognitive decline and induce brain morphological changes [Dagres, 2018; Sepehri Shamloo, 2020]. AF could lead to the formation of small thrombus which in turn can result in small brain silent infarcts. In addition, the increase in beat-to-beat variability may reduce the cardiac output (CO) leading to impaired brain perfusion. Impaired brain perfusion has been linked to increased WMHs and reduced cortical volumes [Alosco, 2013; Jefferson, 2009]. The impaired altered beat-to-beat variability may stress the autoregulatory mechanisms of the vascular system, inducing endothelial dysfunction and vascular remodelling processes [Xia, 2017]. These processes commonly lead to the thickening of the arterioles and occlusion of capillaries which increase the peripheral resistance, R_p, and subsequently triggers the stiffening, τ, of large arteries [Dabrowska, 2020; Laurent, 2015]. Indeed, a mechanistic approach already related AF to hypoperfuse events in the distal circulation [Scarsoglio, 2017].

These processes may explain the changes in the associations between R_p, τ and the brain volumetric indices. The increased peripheral resistance may result in an increased afterload that leads to increased atrial and ventricular filling pressures, which in turn can induce an enlargement of the chambers. This finding is supported by the known role of cardiac remodelling as a risk factor for AF [Seko, 2018; Lau, 2012], and could explain the changes in the associations of R_0 with age and BSA, as well as between σ_0 and BSA.

3.5 Discussion

To our knowledge this study presents the largest cohort of personalised subjects, 3445, being specifically focused on obtaining homogeneous solutions that enable to use the obtained model parameters in post-hoc analyses. The results presented in Section 3.4.2.2, in which we observe the lack of associations between the target features and brain features, highlight the need of combining statistical learning with biophysical models to better understand the underlying physiology in medical data analysis. Moreover, from the uncertainty analysis presented in Section 3.4.2.3 we can conclude that the solutions are stable and meaningful. However, due to the available data, the used cardiovascular features are mostly global features while other studies [Müller, 2014] suggest that brain indices such as WMHs are due to more localised vascular impairments. Hence, brain blood flow characterisation would be useful to estimate more relevant parameters, at least from the main cerebral vessels, which could be obtained from MR angiography images. Moreover, in our model there is no difference between "upper" and "lower" body circulation. Studies analysing the influence of AF in the brain, such as [Scarsoglio, 2017], have differentiated between those circulations. In the future the current biophysical model could be adapted to incorporate a bifurcation towards the upper body circulation. This would allow us to use pulse wave velocity (PWV) measurements at the carotid level to obtain patient-specific solutions in which we could estimate the brain blood flow perfusion. In turn, this would also allow to study the effect of the relative stiffening of the aorta compared to the carotid. Which, according to [Aghilinejad, 2020], is key to attenuate blood flow pulsatility in the brain microvasculature. Another issue to consider is that in our haemodynamic model wave propagation effects are neglected. If continuous blood pressure measurements were available at different locations we could replace the 0D haemodynamic component of our model by a 1D model while keeping a reasonable computational cost. Moreover, the use of continuous measures would allow to use other personalisation approaches such as Kalman filter [Pant, 2017] which can handle uncertainty in the parameter's estimation. Furthermore, currently the covariance matrix of our regularisation term is computed empirically. It would be interesting to explore its parametrisation by means of a kernel or multiple kernels. For example, future work may focus on the study of the relative influence of the features by means of automatic

relevance determination (ARD). Moreover, multiple kernels, one for the external features and another for the model parameters, could be used. However, these approaches would increase the complexity of the problem, since we would need to estimate the kernel hyper-parameters on top of the subject's personalisation.

3.6 Conclusion

We presented a novel statistical learning framework to integrate prior physiological knowledge through biophysical modelling. Its behaviour was exemplified with personalised lumped cardiovascular models on heart and brain data of 3445 subjects. This was achieved by constraining the available parameter-space during parameter optimisation with external brain features in a regularisation term. The presence of the external features allowed to learn a more meaningful representation of the parameter-space enabling to study the interaction of brain features with cardiac model parameters and illustrating the potential use of the framework to estimate cardiac model parameters using a limited amount of clinical information. Additionally, the presented approach can be seen as a parameter selection approach, as demonstrated in [Molléro, 2018], where they shown how the IUP algorithm can select linear subspaces in which non-observable parameters get close to constant values. The identification of non-observable parameters coupled with human modelling expertise can help in the selection of a reduced subset of observable cardiovascular parameters for personalisation. Moreover, the use of this approach provides a generative model that allows to analyse the interaction between external features and non-observable parameters such as the aortic compliance, τ, or the peripheral resistance R_p, which we found to be related with brain-volumetric features. Using the same framework we assessed a clinical subgroup in which we found meaningful clinical relationships, linking AF with WMHs and heart remodelling. These results, along with the small associations between cardiac target features and brain indices, illustrate the potential of combining statistical learning with biophysical modelling. Future work will go towards incorporating brain blood flow characterisation and the assessment of its spatial patterns.

4 Cardiac Imputation Method for Incomplete Datasets

Contents

In this chapter we present a work based on the results obtained with the personalised biophysical cardiac model, described in Chapter 3. The use of mechanistic models in clinical and pathological studies involving several organs and systems is limited by the lack of multi-modal patient data representing different anatomical and physiological processes. For example, neuroimaging datasets do not provide a sufficient representation of heart features for the modeling of cardiovascular factors in brain disorders. To tackle this problem we introduce a probabilistic framework for joint cardiac data imputation and personalisation of cardiovascular mechanistic models, with application to brain studies with incomplete heart data. Our approach is based on a variational framework for the joint inference of an imputation model of cardiac information from the available features, along with a Gaussian Process emulator that can faithfully reproduce personalised cardiovascular dynamics. This work was presented at the MICCAI conference in 2020 [Banus, 2020].

4.1 Introduction

Heart and brain are characterised by several common physiological and pathophysiological mechanisms [Doehner, 2018]. The study of this multi-organ relationship is of great interest, in particular to better understand neurological diseases such as vascular

dementia or Alzheimer's disease. The development of computational models simulating heart and brain dynamics is currently limited by the lack of databases containing information for both organs. Neuroimaging datasets often provide a limited number of cardiac-related measurements, usually restricted to brachial diastolic and systolic blood pressure (DBP, SBP) [Epstein, 2013]. These quantities provide a limited assessment of the cardiac function, thus compromising the possibility of further analysis of cardiovascular factors in brain disorders.

On the contrary, the availability of a rich set of cardiac information in heart studies allows the use of cardiovascular models to estimate descriptors of the cardiac function that are not possible to measure in-vivo, such as contractility or stiffness of the heart fibres. These models optimise the parameters through data-assimilation procedures to reproduce the observed clinical measurements [Molléro, 2017], but usually do not include neurological factors. The ability to jointly account for cardiovascular descriptors and brain information is key to gather novel insights about the relationship between heart dynamics and brain conditions.

Most of current studies relating heart and brain are based on statistical association models, such as based on multivariate regression [Cox, 2019]. While this kind of analysis allows to easily formulate and test association hypotheses, it usually offers a limited interpretation of the complex relationship between organs. This issue is generally addressed by mechanistic modelling, allowing deeper insights on physiological and biomechanical aspects. These models allow for example to describe the brain vasculature, and to quantify physiological aspects such as blood flow auto-regulation effects in the brain [Acosta, 2018], up to the simulation of the whole-body circulation with detailed compartmental components [Blanco, 2015]. Although these approaches offer a high level of interpretability, they are usually severely ill-posed and require large data samples and arrays of measurements to opportunely tune their parameters.

To bridge the gap between data-driven and mechanistic approaches to heart-brain analysis, we propose to learn cardiovascular dynamics from brain imaging and clinical data by leveraging on large-scale datasets with missing cardiac information. This is achieved through an inference framework composed of two nested models accounting respectively for the imputation of missing cardiac information conditioned on the available cardiac and brain features, and for a Gaussian Process emulator that mimics the behavior of a lumped cardiovascular model. This setting allows to formulate a probabilistic end-to-end generative model enabling imputation of missing measurements and estimation of cardiovascular parameters given a subset of observed heart and brain features.

Results on real data from the UK Biobank show that our framework can be used to reliably estimate and simulate cardiac function from datasets in which we have minimal cardiovascular information, such as SBP and DBP only. Moreover, the proposed frame-

work allows novel exploration of the joint heart-brain relationship through the simulation of realistic cardiac dynamics corresponding to different scenarios of brain anatomy and damage.

4.2 Methods

4.2.1 Problem statement

We denote by ν the vector representing brain image-derived phenotypes (IDPs) and clinical information such as age or body surface area (BSA), and by x the vector of cardiac IDPs and blood pressure measurements. The vector x can be represented as $x = \{\hat{x}, x_{obs}\}$ where $\hat{x}$ represents the unobserved information we wish to impute and x_{obs} the observed one. Moreover, we assume that for each observation x a corresponding set of parameters y of the associated lumped model is available. We would like to learn a generative model in which we assume that the unobserved measurements are generated by a latent random variable z conditioned on the variables ν. Hence, our generative process can be seen as sampling from a distribution $p(z|\nu)$ and then obtaining $\hat{x}$ with probability $p(\hat{x}|z, \nu)$. Due to the association between cardiac IDPs, x, and lumped model parameters y, we also assume that the latter are dependent from ν through z. Our graphical model is shown in Figure 4.1, while the evidence lower bound (ELBO) of the joint data marginal $p(y, \hat{x}|x_{obs}, \nu)$ writes as:

$$
\begin{aligned}
\log p(y, \hat{x}|x_{obs}, \nu) &= \int \log p(y, \hat{x}|x_{obs}, z, \nu) p(z|\nu) dz \\
&\geq \mathbb{E}_{q_\phi(z|x_{obs},\nu)} \log p(y, \hat{x}|x_{obs}, z, \nu) \\
&- KL(q_\phi(z|x_{obs}, \nu)||p_\theta(z|\nu)) \\
&= \mathbb{E}_{q_\phi(z|x_{obs},\nu)} \log p_\omega(y|x_{obs}, z) \\
&+ \mathbb{E}_{q_\phi(z|x_{obs},\nu)} \log p_\theta(\hat{x}|\nu, z) \\
&- KL(q_\phi(z|x_{obs}, \nu)||p_\theta(z|\nu)) \equiv \mathcal{L}(\theta, \phi, \omega; x_{obs}, \nu)
\end{aligned}
\tag{4.1}
$$

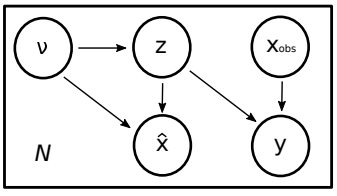

Fig. 4.1.: Graphical model of our framework. From a latent variable z we generate the unobserved features $\hat{x}$ conditioned on the variables ν and we estimate y via Gaussian process regression. During inference x_{obs} and ν are used to estimate the approximated posterior $q_\phi(z|x_{obs}, \nu)$.

The approximation of the posterior distribution by $q_\phi(z|x_{obs}, \nu)$ defines the optimisation of the ELBO through variational inference. The variational distributions $q_\phi(z|x_{obs}, \nu)$ and $p_\theta(\hat{x}|\nu, z)$ are parameterised respectively with parameters ϕ and θ. The term $\log p_\omega(y|x_{obs}, z)$ in the ELBO denotes the emulator which approximates the mechanistic behavior of the lumped model via Gaussian Process regression parameterised by ω. The choice of a GP as emulator is motivated by the uncertainty of the data, hence it is desirable to obtain a distribution of interpolating functions rather than a single deterministic function. Moreover, GPs have already been proved to be valid emulators of 1D mechanistic vascular models [Melis, 2017]. The GP allows to sample functions $f(x)$ from a given prior parameterized by a mean $\mu(x)$ and covariance $\Sigma(x)$, i.e: $f(x) \sim \mathcal{N}(\mu(x), \Sigma(x))$ to obtain the marginal $y \sim \mathcal{N}(\mu(x), \Sigma(x) + \sigma^2 I)$. The prior mean $\mu(x)$ is here set to 0 and we use a radial-basis function (RBF) kernel for the covariance:

$$k^j(x_i, x_i') = \alpha_j^2 exp\left(-\frac{(x_i - x_i')^2}{2\beta_i^2}\right), \tag{4.2}$$

Since our data is multi-dimensional, $k^j(x_i, x_i')$ is the kernel for the j^{th} target and the i^{th} predictor. The hyper-parameters of the kernel $\omega = \{\alpha, \beta\}$ represent the output amplitude α and length scale β of the sampled functions. The goal during training is to learn the hyper-parameters that maximise the marginal likelihood of the observed data y .

The second term of the ELBO is related to the imputation of $\hat{x}$. The term $\log p_\theta(\hat{x}|\nu, z)$ denotes the log-likelihood of the imputed features, which can be seen as the reconstruction error. The last term $KL(q_\phi(z|x_{obs}, \nu)||p_\theta(z|\nu))$ is the Kullback–Leibler divergence between variational approximation and prior for z, that can be expressed in a closed form given that both distributions are Gaussians. The imputation scheme is equivalent to a conditional variational autoencoder (CVAE) which has become a popular approach to feature imputation [Ivanov, 2019]. Fast and efficient optimisation in our model is possible by means of stochastic gradient descent thanks to the closed form for data fit and KL terms, the use of the reparametrisation trick and Monte Carlo sampling.

4.2.2 Data processing and cardiovascular model

From UK Biobank we selected a subset of 3445 subjects for which T1, T2 FLAIR magnetic resonance images (MRI) and several brain and cardiac IDPs were available. Among the brain IDPs we used total grey matter (GM), total white matter (WM) and ventricles volumes. We used T1 and T2 FLAIR images to obtain the number of white matter hyperintensities (WMHs) and their total volume relying on the lesion prediction algorithm (LPA), available from the lesion segmentation toolbox (LST) [Schmidt, 2017] of SPM [1].

[1] https://www.fil.ion.ucl.ac.uk/spm

WMHs are a common indicator of brain damage of presumably vascular origin [Wardlaw, 2015]. We combined WM and GM volumes into a single measurement that we denoted as brain volume. The WMHs total volume and number of lesions presented a skewed distribution, and were Box-Cox transformed prior to the analysis. Regarding the cardiac IDPs we selected stroke volume (SV), ejection fraction (EF) and end-diastolic volume (EDV) for the left ventricle. All brain-related volumes were normalized by head size. Besides IDPs, we had access to blood pressure measurements (DBP, SBP) and socio-demographic features such as age and body surface area (BSA). We used DBP and SBP to compute MBP as $MBP = DP + (SP - DP)/3$. Next, we used the lumped cardiovascular model derived in [Caruel, 2014] to obtain additional indicators of the cardiac function. In particular we estimated the compliance of the main systemic arteries (τ), peripheral resistance (R_p) , the radius of the left ventricle (R_0), contractility of the cardiac fibres (σ_0) and their stiffness (C_1). The parameters of the model were selected based on the available clinical data. To obtain the target values for the emulator, the data-assimilation procedure was carried out according to the approach presented in [Banus, 2019; Molléro, 2018].

4.2.3 Experiments

The data was split in two sets: one containing the full-information (2309 subjects), and one in which cardiac IDPs ($\hat{x}$) and the estimated model parameters (y) were removed (1136 subjects, Table 1). The quality of imputation was compared to conventional methods such as mean, median and k-nearest neighbors (KNN) imputation. We subsequently assessed the relationship learnt by our model between brain features and cardiovascular parameters through simulation. Starting from the mean values of each parameter we sampled along the dimension of the different conditional variables ν that we used to parameterize the prior. This procedure allowed us to assess their influence in the inferred simulation parameters.

Tab. 4.1.: Variables used in our framework. Mean blood pressure (MBP), diastolic blood pressure (DBP), stroke volume (SV), end-diastolic volume (EDV), ejection fraction (EF), heart fibres contractility (σ_0), ventricle size (R_0), heart fibres stiffness (C_1), peripheral resistance (R_p) and aortic compliance (τ)

Input (x_{obs})	Condition (ν)	Imputed ($\hat{x}$)	Predicted (y)
MBP	Brain volume	SV	σ_0
DBP	Ventricles volume	EDV	R_0
	WMHs volume	EF	C_1
	Num. WMHs		R_p
	BSA		τ
	Age		

4.3 Results

4.3.1 Data imputation and regression

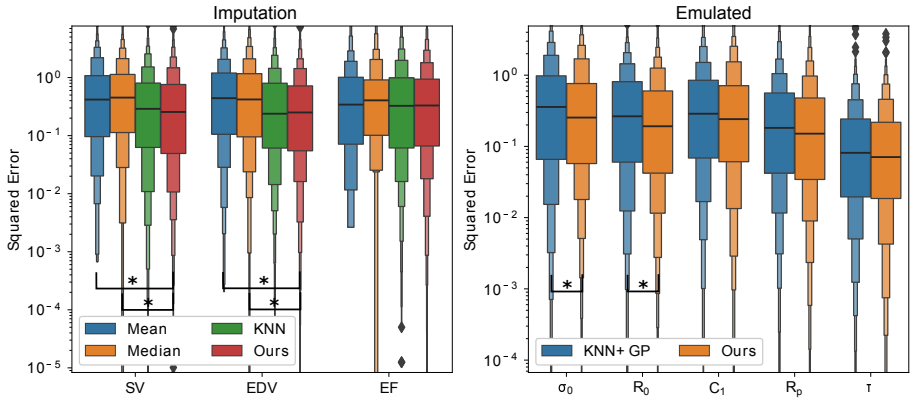

Fig. 4.2.: Mean squared error (MSE) a) of the imputation of missing cardiac measurements ($\hat{x}$) b) of the estimated parameters of the emulated cardiovascular lumped model (y). * denotes that the MSE distributions are significantly different with respect to our method according to the Wilcoxon rank-sum test using a significance level of $a = 0.05$, Bonferroni corrected by multiple comparison. The y-axis is represented in log-scale.

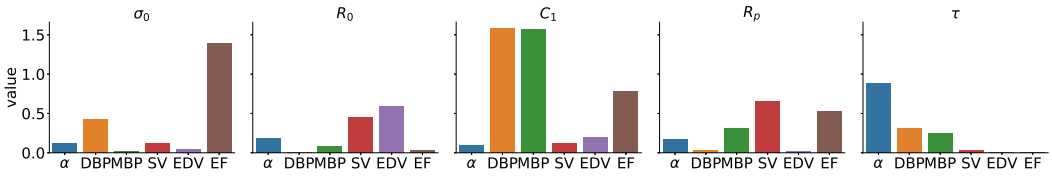

Fig. 4.3.: Automatic relevance determination (ARD) of each predictor for each target feature. SV, stroke volume; EDV, end-diastolic volume; EF, ejection fraction; DBP, diastolic blood pressure; MBP, mean blood pressure; σ_0, fibres contractility; R_0, left ventricle size; C_1, fibres stiffness; R_p, peripheral resistance; τ, arterial compliance.

We assessed the performance of our model by measuring the mean squared error (MSE) on the testing data, for both the imputation of missing cardiac information and the emulation of the lumped model parameters. The results in Figure 4.2a show that our method gives significantly better estimates than mean and median imputation, and comparable predictions to KNN, for which the optimal number of neighbors was optimized through 10-fold cross-validation and corresponds to $K = 10$. At the same time the emulator consistently gives low errors for the parameters' estimation (Figure 4.2b). In Figure 4.3 we present the most relevant predictors for each emulated feature based on their β values, the left ventricle contractility, σ_0, is mostly dependent on the ejection fraction, while the size of the left ventricle, R_0, is related to the end-diastolic and stroke volumes. The stiffness of the left ventricle fibres, C_1, is mainly predicted using the blood pressures (MBP, DBP) and the ejection fraction, while the compliance of the main arteries, τ, is mainly predicted by the blood pressures. Finally, the peripheral resistance,

R_p, is predicted based on the ejection fraction, the stroke volume and the mean blood pressure.

4.3.2 Cardiovascular dynamics simulation and model plausibility

In the left column of Figure 4.4 we observe the change in the predicted parameters of the cardiovascular model as we sample along the range of values of the different conditional variables, ν. The right column of Figure 4.4 shows the pressure-volume (PV) loops generated by the lumped model using the inferred parameters. The simulated PV loops highlight meaningful relationships:

- An increase in the volume of WMHs is associated to decreased SV and EDV, together with a smaller reduction of ESV, leading to a decrease of EF which is related to reduced contractility.

- Similar dynamics are associated to brain volume loss.

- The number of WMHs exhibits different dynamics than WMHs volume, associated to the increase in afterload and the increase of EDV.

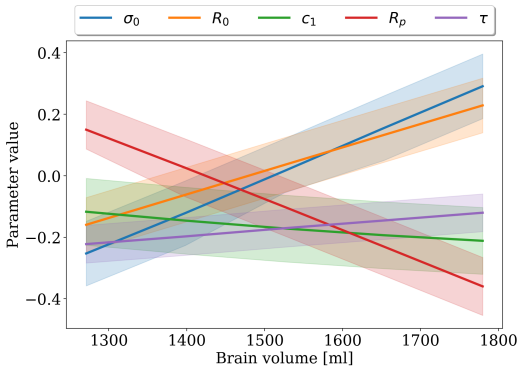

(a) Model parameters as brain volume changes

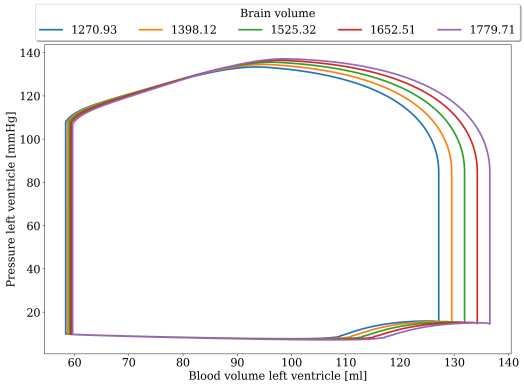

(b) Evolution of PV loop as brain volume changes

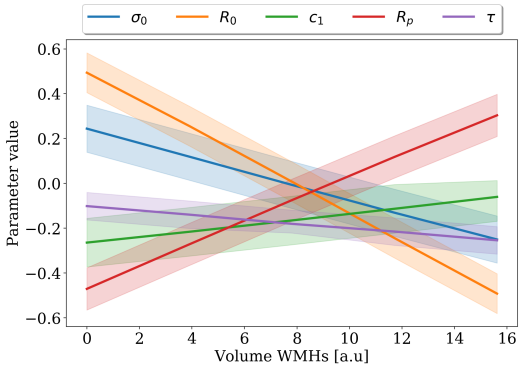

(c) Model parameters as WMHs volume changes

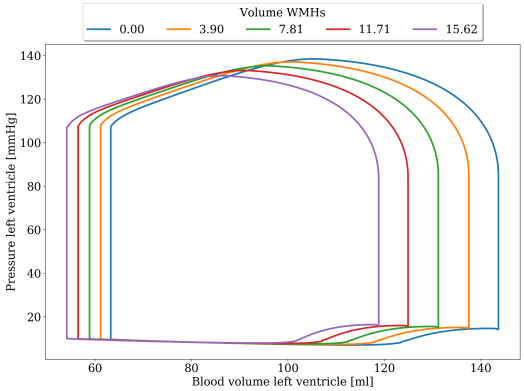

(d) Evolution of PV loop as WMHs volume changes

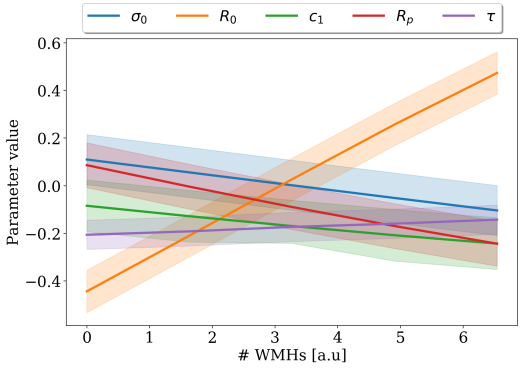

(e) Model parameters as number of WMHs changes

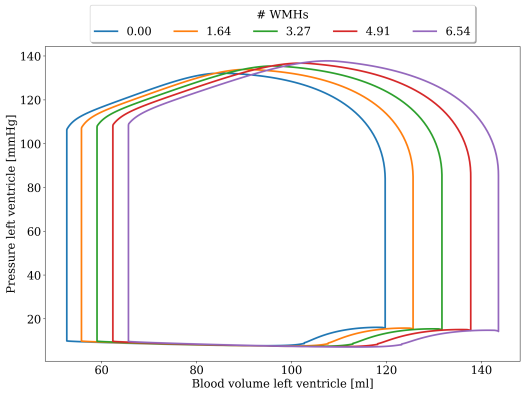

(f) Evolution of PV loop as number of WMHs changes

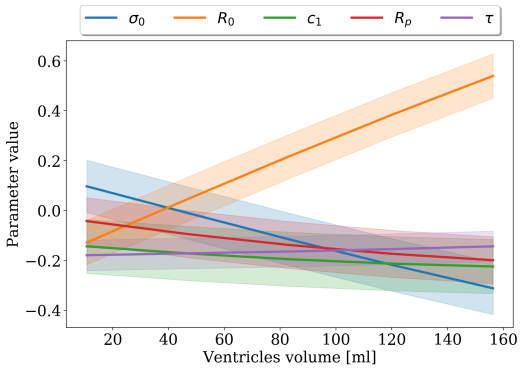

(g) Model parameters as ventricles volume changes

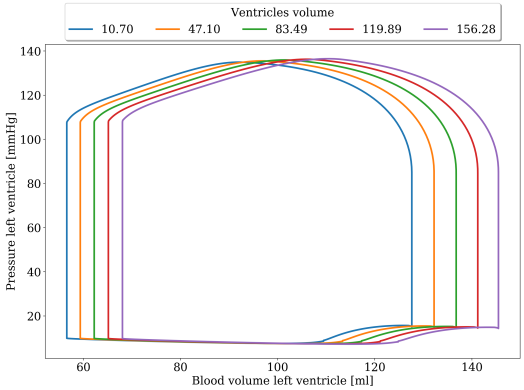

(h) Evolution of PV loop as ventricles volume changes

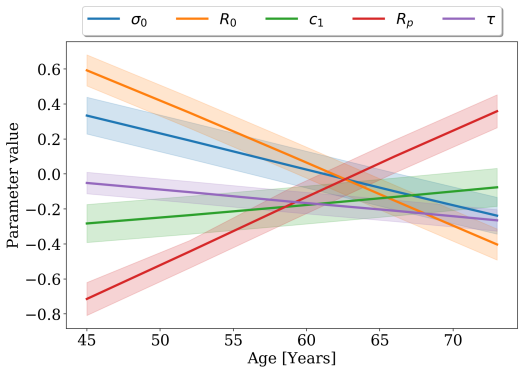

(i) Model parameters as age changes

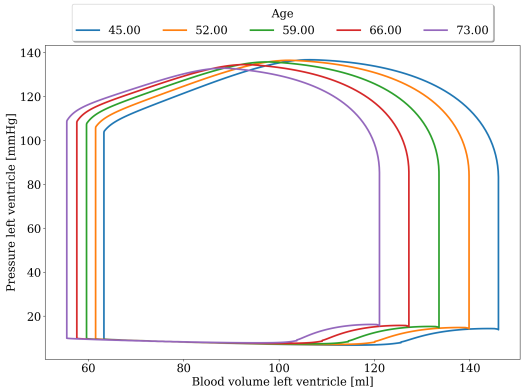

(j) Evolution of PV loop as age changes

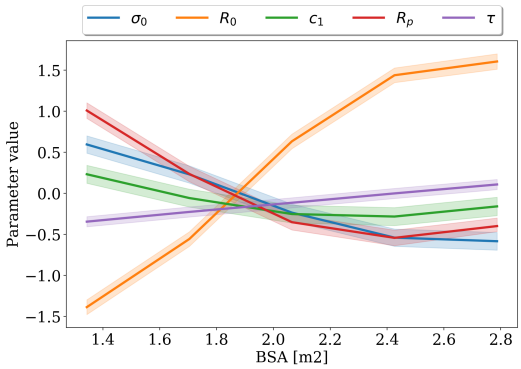

(k) Model parameters as BSA changes

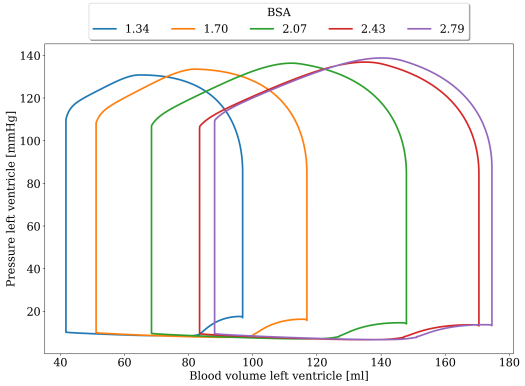

(l) Evolution of PV loop as BSA changes

Fig. 4.4.: In the left column we can observe the inferred model parameters and their respective confidence interval as we sample along the dimension of the different conditional variables, ν, while keeping the other elements of the generative framework constant. The right column presents the pressure-volume (PV) loops generated by the the cardiovascular lumped model given the mean inferred parameters. BSA, body surface area; WMHs, white matter hyperintensities.

From the plots showing the estimation of the parameters we can observe the ones driving the observed dynamics. For example, WMHs and brain volumes changes are mainly driven by the joint evolution of peripheral resistance (R_p), contractility (σ_0) and size of the left ventricle (R_0). The changes in the number of WMHs are related to heart-remodelling changes, driven by R_0 and by a decrease of σ_0 and the ventricular stiffness c_1. The relationship between R_0 and BSA is something we expected due to the linear relationship between cardiac output and body dimensions [Jegier, 1963]. The reduction of R_0, the loss of contractility σ_0 [Akasheva, 2015], arterial stiffening, and the increase in peripheral resistance as we get older are also in line with expected physiological responses [Kohn, 2015]. Overall, in the simulated dynamics we can identify several physiological responses in line with the clinical literature, suggesting that our model is capable of learning a feasible evolution of cardiovascular dynamics. Moreover, our model may be useful to give insights in currently controversial topics such as concerning the pathogenesis of WMHs. Our results suggest that the evolution of cardiac function with respect to brain and WMHs volumes is similar to the one due to aging, while the effect

induced by the number of WMHs is similar to the one related to ventricles enlargement. In both cases the changes in R_0, σ_0 and C_1 suggest that the increase in number of WMHs and the enlargement of brain ventricles are associated with heart-remodelling processes, such as loss of contractility or decrease in compliance. These findings are in line with clinical observations [Jefferson, 2009] relating lower cardiac output with higher burden of WMHs and reduced brain volume.

4.4 Conclusion

We presented a generative model that enables the analysis of complex physiological relationships between heart and brain in datasets where we have minimal available features. The framework allows to emulate a lumped cardiovascular model through data-driven inference of mechanistic parameters, and provides us a generative model to explore hypothetical scenarios of heart and brain relationships. In the future, the model will allow to potentially transfer the knowledge learned in UK Biobank to datasets where we have a minimal number of cardiac information, to explore the relationship between brain conditions and cardiovascular factors in specific clinical contexts, such as in neurodegeneration. Our approach could also be extended to account for deep learning architectures, and the framework could be further improved by jointly accounting for multiple outputs, which are currently modelled independently, or by including spatial information from imaging data, beyond the modelling of scalar volumetric features. Furthermore, while the cardiovascular features considered in this study are rather general, more complex features will allow to study more realistic cardiovascular models. For example, while the mechanistic model used in this study does not simulate cerebral blood flow, previous studies suggested that WMHs may be due to local vascular impairment [Müller, 2014]. Hence, by selecting appropriate clinical features we could constrain the imputation by means of any biophysical model representing the desired aspect of systems biology. This could represent an innovative tool in real world scenarios, for which multi-modal patient data is often limited or not available.

5 Alzheimer's Disease Progression Model including Heart & Brain

Contents

In this chapter we present a use case applying the developed cardiac data imputation and mechanistic model personalisation, described in Chapter 3 and Chapter 4. We used the probabilistic imputation framework to jointly impute additional cardiac data and estimate the parameters of the cardiovascular model based on the heart-brain dynamics learned in the UK Biobank. Using these additional descriptors of the cardiac function, together with the neurophysiological information and brain imaging biomarkers of the ADNI dataset, we estimated a disease-specific time-scale that allowed to analyse the role of cardiac function in AD, and assess the potential of the cardiac model parameters to identify population at risk of dementia.

5.1 Introduction

Vascular pathologies such as small vessel disease (SVD) are extremely frequent in aging and very commonly mixed with dementia [Wardlaw, 2019; Azarpazhooh, 2018]. Up to 70% of the Alzheimer's disease (AD) cases present a vascular component [Kapasi, 2017], highlighting the fact that mixed pathologies are the rule not the exception. Moreover, there is growing evidence showing association between cardiac diseases, such as heart failure (HF) [Doehner, 2018] or atrial fibrillation (AF) [Diener, 2019; Sepehri Shamloo,

2020], to cognitive decline. The presence of co-morbidities suggests the existence of a common underlying mechanism of degeneration.

Brain multimodal imaging can be used to estimate morphological features such as the volumes of grey and white matter. Moreover, it is also possible to obtain markers of vascular disease such as white matter hyperintensities (WMHs) or microbleeds, which are associated to small vessel disease and cognitive decline [Wardlaw, 2015]. In addition, vascular risk factors such as hypertension, specifically in mid-life, are among the largest risk factors for dementia, and are potentially modifiable. A study in the 'British birth cohort 1946' found that mid-life hypertension is associated to late-life increase in WMHs, and to a decrease of the brain volume [Lane, 2019]. At the same time the increase of WMHs and the decrease of GM volume have been linked to brain hypoperfusion [Jefferson, 2009].

These results suggest that cardiovascular risk factors and imaging biomarkers can help to better understand the progression of neurodegenerative diseases, such as AD, and describe its trajectory over time. A study on ADNI[1] [Mueller, 2005] suggested that changes in vascular biomarkers and decreased cerebral blood flow (CBF) occur before detectable changes in AD-specific biomarkers such as $A\beta$ and tau cerebrospinal fluid (CSF) [Iturria-Medina, 2016]. However, even in longitudinal studies, establishing the trajectories for different biomarkers is complicated since subjects may be located at considerably different stages of the disease and it is not possible to track them for long periods of time. Jack et al. [Jack, 2013] presented an hypothetical model of the temporal evolution of AD biomarkers relative to the onset and progression of clinical symptoms. This model describes amyloid abnormalities followed by tau and eventually cognitive decline. Recently, Sweeney et al. [Sweeney, 2018] updated the timeline of Jack et al. [Jack, 2013] considering the contribution of vascular effects, and suggesting that CBF and blood-brain barrier (BBB) functioning are altered prior to cognitive decline, brain atrophy and amyloid/tau abnormalities.

Longitudinal disease progression modeling (DPM) approaches have been proposed for the data-driven estimation of the disease timeline. In particular, a disease-specific time-scale is obtained based on the subjects measurements of the different biomarkers and their longitudinal evolution [Lorenzi, 2019; Abi Nader, 2020; Marinescu, 2019; Koval, 2017]. However, the extension of DPM to account for cardiac related measurements is limited by the lack of relevant biomarkers for the cardiac function. In databases focused on neurodegenerative diseases, cardiac-related measurements are usually limited to brachial diastolic and systolic blood pressures (DBP, SBP) [Epstein, 2013]. The lack of cardiac-related measurements hampers the development of computational models studying heart and brain interactions. In particular, it would be interesting to use mechanistic models

[1] Alzheimer's Disease Neuroimaging Initiative

whose parameters represent non-observable descriptors of the cardiac function linked to physiological properties, such as cardiac contractility. In-silico mechanistic studies have described potential mechanisms through which AF [Scarsoglio, 2017] or arterial stiffening [Aghilinejad, 2020] could affect the brain perfusion explaining their association with cognitive decline. Hence, the study of cardiac function in neurodegenerative diseases through cardiovascular mechanistic models together with DPM could identify parameters with the potential to be used as early dementia biomarkers. However, patient-specific estimations of these parameters are obtained through data-assimilation procedures in order to reproduce the observed clinical measurements [Molléro, 2017]. Hence, the study of heart-brain interactions through these models is only possible nowadays in large-scale epidemiological studies such as the UK Biobank [Sudlow, 2015], containing joint cardiac and brain imaging information.

The imputation framework presented in Chapter 4 [Banus, 2020] provides the opportunity to estimate cardiac volumetric features and cardiovascular model parameters based on the available socio-demographic and brain imagining information in the ADNI dataset. This information can be subsequently used to enrich DPM to account for the dynamics of cardiovascular factors along with standard dementia biomarkers. In what follows, the proposed imputation framework was trained using UK Biobank data (i.e., with heart and brain data) and is used to obtain an estimation of the cardiac function for every individual in the ADNI dataset (i.e., with limited heart data) without data-assimilation procedures. We used the imputed cardiac biomarkers together with the available clinical scores and brain morphological features to estimate a disease-specific time-scale using the DPM framework proposed in [Lorenzi, 2018]. The obtained disease evolution suggests an early impairment of the cardiac function, prior to brain morphological abnormalities and cognitive scores. The estimated evolution also correlates well with CSF biomarkers and is capable to stratify subjects by disease-stage. These findings suggest the potential use of cardiovascular model parameters as biomarkers to identify individuals at risk or early-stages of dementia.

5.2 Methods

Our study is based on data from two multi-centric studies, UK Biobank and ADNI. The following sections describe in the detail the data processing pipeline and the main approach used in this work to model the joint pathological evolution between cardiac indicators and AD biomarkers.

5.2.1 Data processing

The UK Biobank data was processed according to the methods described in Chapter 3. In short, we selected (3445) subjects, for which cardiac and brain magnetic resonance imaging (MRI) data were available. Firstly, we used the available pre-computed imaging features extracted from the cardiac and brain images. Brain imaging features include white matter (WM), grey matter (GM) and ventricles volumes. All volumes were normalized by head size, and we combined WM and GM volumes into a single measurement that we denoted as brain volume. Subsequently, the total number and volume of WMHs was obtained after processing the brain MRI data using the lesion prediction algorithm (LPA), available from the lesion segmentation toolbox (LST) [Schmidt, 2017] of SPM [2]. WMHs total volume and number of lesions were Box-Cox transformed prior to the analysis. The cardiac features we employed from the UK Biobank data consisted on stroke volume (SV), ejection fraction (EF) and end-diastolic volume (EDV) for the left ventricle. Moreover, we had access to diastolic and systolic blood pressure measurements (DBP, SBP) and socio-demographic features such as age, weight and height. DBP and SBP were used to compute mean blood pressure (MBP) as $MBP = DP + (SP - DP)/3$. Body surface area (BSA) was computed using height and weight of each subject according to Mosteller's formula [Mosteller, 1987]: $BSA = \sqrt{\frac{Weight[kg]*Height[cm]}{3600}}$. This data is used to personalise the cardiovascular biophysical model [Caruel, 2014], as described in Chapter 3. In particular we estimated the compliance of the main systemic arteries (τ), peripheral resistance (R_p), the radius of the left ventricle (R_0), contractility of the cardiac fibres (σ_0) and their stiffness (C_1). The parameters of the model were selected based on the available clinical data.

Concerning ADNI, we used data from ADNI3, since the imaging protocols for both T1 and T2 FLAIR acquisitions were similar to the ones used in UK Biobank. The imaging features were derived by processing the MRI data using the UK BIobank pipeline [Alfaro-Almagro, 2018]. Age at the imaging visit was estimated using the birth date and the date of the imaging exam. WMHs information was obtained accordingly with the UK Biobank processing, using the parameters of the Box-Cox transformation previously estimated. Blood pressure and socio-demographic features were pre-processed as described in the previous paragraph for the UK Biobank data. We considered 809 subjects in total, partitioned in 457 cognitively normal (CN), 261 with mild-cognitive impairment (MCI) and 91 with AD. 470 of them had only one visit available, 269 had two visits, while three or more visits were available for 70 subjects. Table 5.1 provides a summary of the baseline population statistics, and Table 5.2 details the number of subjects for which PET and CSF information was available stratified by diagnosis. It can be easily noticed the relatively low number of samples, in particular for AD subjects.

[2] https://www.fil.ion.ucl.ac.uk/spm

Tab. 5.1.: Statistics of the UK Biobank and of the ADNI dataset by group at baseline (Mean ± Std). Bold features indicate that they have been imputed in the ADNI dataset. CN, cognitively normal; MCI, mild-cognitive impairment; AD, Alzheimer's disease.

	UK Biobank	ADNI		
Subjects	3445	CN (457)	MCI (261)	AD (91)
Age $(Years)$	61.07 ± 7.12	73.34 ± 7.43	75.01 ± 8.08	77.26 ± 8.10
BSA (m^2)	1.88 ± 0.21	1.90 ± 0.24	1.91 ± 0.23	1.87 ± 0.22
DBP $(mmHg)$	75.49 ± 12.10	75.17 ± 9.29	74 ± 9.16	73.2 ± 9.76
SBP $(mmHg)$	132.09 ± 18.77	134.68 ± 16.74	135.28 ± 17.72	134.43 ± 19.08
MBP $(mmHg)$	94.35 ± 13.12	95.01 ± 10.15	94.43 ± 10.39	93.61 ± 10.95
SVI (ml/m^2)	41.48 ± 2.73	35.87 ± 2.88	35.31 ± 3.17	34.23 ± 3.39
EDVI (ml/m^2)	73.92 ± 4.04	66.52 ± 4.40	66.26 ± 4.89	65.28 ± 5.60
ESVI (ml/m^2)	32.92 ± 9.34	30.19 ± 2.24	30.55 ± 2.26	30.66 ± 2.69
EF $(\%)$	56.21 ± 6.24	54.37 ± 1.83	53.81 ± 1.76	53.40 ± 1.57
WM (mm^3)	711,454 ± 40,719	703,630 ± 52,161	697,927 ± 53,236	682,294 ± 56,570
GM (mm^3)	801,685 ± 46,702	736,172 ± 57,540	709,381 ± 59,882	660,774 ± 56,178
Ventricles (mm^3)	42,807 ± 17,612	58,823 ± 25,539	69,292 ± 27,921	89,927 ± 33,839
WMHs $(a.u)$	7.5 ± 2	10.52 ± 2.75	11.53 ± 3.13	13.14 ± 2.75
# WMHs $(a.u)$	3.27 ± 0.85	2.90 ± 0.85	3.17 ± 0.89	3.46 ± 0.65

Tab. 5.2.: Available CSF and PET biomarkers.

Diagnosis	AV45	FDG	$A\beta 40$	$A\beta 42$	$A\beta 42/A\beta 40$	Tau	pTau
AD	54	62	35	35	35	35	34
CN	263	17	202	202	202	202	200
MCI	137	193	105	105	105	105	105

5.2.2 Cardiac data imputation

The parameters of a mechanistic model are usually estimated through data-assimilation procedures such that the model reproduces the available clinical observations. For example, the contractility or size of the left ventricle are tuned such that simulation results match the measured stroke volume (SV) or the end-diastolic volume (EDV). Due to the limited cardiac data available in the ADNI dataset, we used the method presented in Chapter 4 [Banus, 2020] to simultaneously estimate the missing cardiac volumetric biomarkers together with the parameters of the mechanistic model.

The method consists of a joint generative model in which we assume that there is a common latent variable that is influenced by the brain status and connects the missing cardiac information and the parameters of the mechanistic cardiovascular model. Therefore, based on the mean and diastolic brachial blood pressures, the brain volumetric features, and demographic information (e.g., age, body surface area), we imputed the

most likely stroke volume, end-diastolic volume and ejection fraction. Next, the imputed additional cardiac information together with the available blood pressures are used to estimate the parameters of the biophysical model. In practice, the joint model consists of a conditional variational autoencoder (CVAE) for the imputation, and a Gaussian Process (GP) regression for the emulation of the mechanistic model. This framework was trained in UK Biobank data, and the joint optimisation allows to constrain the imputation to plausible values with respect to the dynamics described by the mechanistic model.

5.2.3 Disease progression modeling

Using the additional cardiac information derived from the imputation framework, and the cognitive scores and brain volumetric features available in ADNI , we estimated a disease specific time-scale with the disease progression model (DPM) described in [Lorenzi, 2019]. The disease evolution is obtained by temporally re-aligning data from different subjects based on the estimated temporal trajectories of every biomarker. The temporal trajectories of each biomarker are defined as monotonic increasing or decreasing trends, based on prior clinical knowledge, in order to constrain the problem. For example, brain volume is imposed to be monotonically decreasing, while the brain ventricles size is assumed to be monotonically increasing throughout disease progression. The ensemble of these constraints controls the data-driven estimation of the biomarker progression from healthy to pathological stages. Technically, the temporal trajectories of each biomarker are defined as monotonic and time-reparameterised Gaussian Processes, allowing to temporally re-align the observations of each individual into a common disease specific time-scale. The resulting subject-specific temporal alignment identifies the *disease stage* associated to a given individual based on his/her measurements.

5.3 Results

5.3.1 Imputed data

In Figure 5.1 we can observe a subset of available and imputed data in ADNI, stratified by diagnosis group; the figure illustrates the features for which there is a significant group-wise difference according to a Wilcoxon rank-sum using a significance level of $\alpha = 0.05$, Bonferroni corrected. In Figure 5.1a we observe a decrease in total brain volume, as well as an increase in ventricles volume and in the total number and volume of WMHs associated to the disease progression, while the age of the controls is significantly lower with respect to the MCI and AD subjects. Concerning the imputed data shown in Figure 5.1b we see a significant reduction of EF and left ventricle contractility, σ_0, between controls and AD, as well as a significant decrease in the SVI in AD patients.

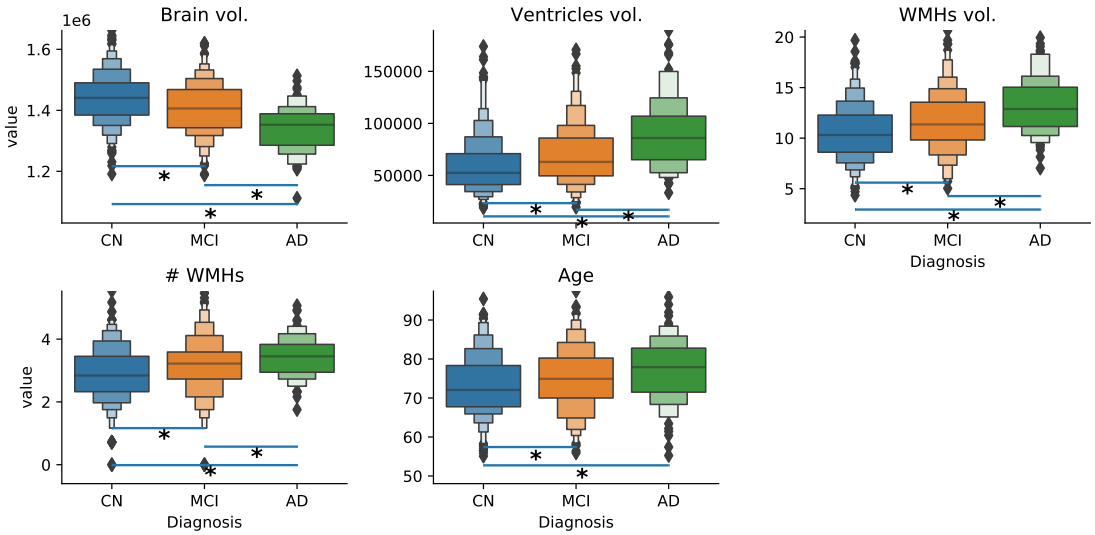

(a) Observed data

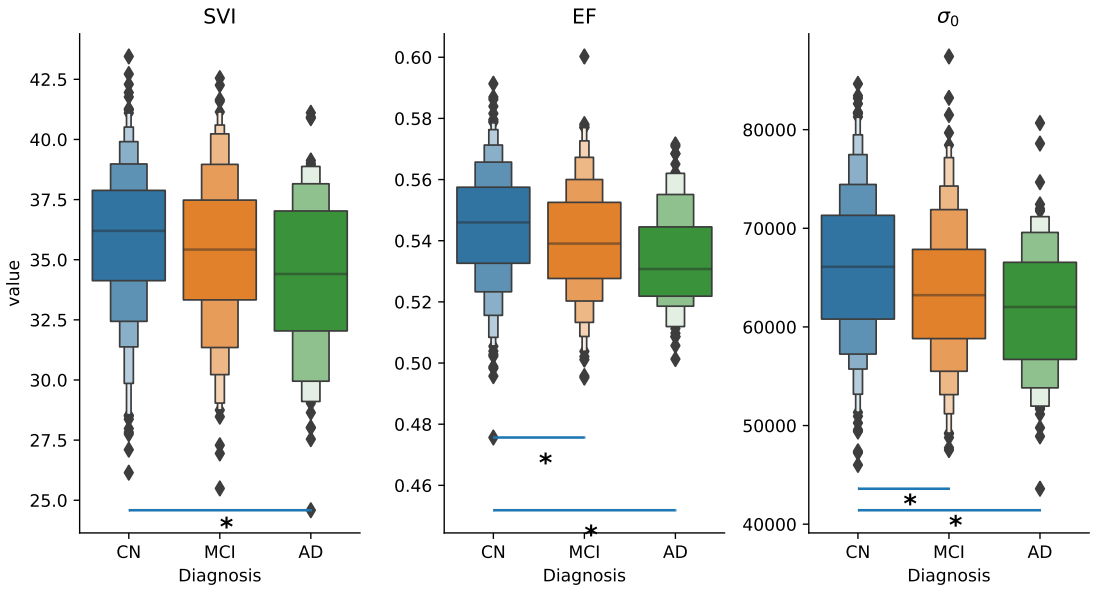

(b) Imputed data

Fig. 5.1.: Features that present significant differences between clinical groups, indicated by $*$. a) Observed and b) imputed data [Banus, 2020]. WMHs, white matter hyperintensities; SVI, stroke volume index; EF, ejection fraction; σ_0, left ventricle contractility.

Tab. 5.3.: Linear association between data and cognitive scores. We used ordinary least squares (OLS) regression and the data was normalised to 0 mean and unit variance for better interpretability. Bold features indicate a significant statistical association for which the slope is different from 0 (Wald test). The significance level was set to $\alpha = 0.05$ corrected by Bonferroni factor of 54.

Cognitive Score	Feature	Slope	Intercept	Correlation	p-val	Std. error
CDRSB	$\boldsymbol{\sigma_0}$	-0.10	0.10	-0.18	<1e-6	0.02
	C_1	0.00	-0.00	0.01	0.89	0.02
	R_p	0.04	-0.04	0.07	0.06	0.02
	τ	-0.02	0.02	-0.03	0.40	0.02
	EF	-0.10	0.11	-0.19	<1e-6	0.02
	EDVI	-0.04	0.05	-0.08	0.02	0.02
	SVI	-0.09	0.10	-0.17	<1e-6	0.02
	ESVI	0.03	-0.03	0.06	0.09	0.02
	CI	-0.05	0.05	-0.09	0.01	0.02
	DBP	-0.03	0.03	-0.05	0.12	0.02
	MBP	-0.02	0.03	-0.05	0.18	0.02
	SBP	-0.01	0.01	-0.02	0.48	0.02
	PP	0.00	-0.00	0.01	0.88	0.02
	Brain volume	-0.20	0.22	-0.38	<1e-6	0.02
	Ventricles volume	0.18	-0.20	0.35	<1e-6	0.02
	WMHs	0.15	-0.16	0.28	<1e-6	0.02
	# **WMHs**	0.10	-0.11	0.20	<1e-6	0.02
ADAS11	$\boldsymbol{\sigma_0}$	-0.04	0.45	-0.22	<1e-6	0.01
	C_1	-0.01	0.10	-0.05	0.16	0.01
	$\boldsymbol{R_p}$	0.02	-0.24	0.12	<1e-4	0.01
	τ	-0.01	0.17	-0.08	0.02	0.01
	EF	-0.04	0.45	-0.22	<1e-6	0.01
	EDVI	-0.02	0.24	-0.12	<1e-4	0.01
	SVI	-0.04	0.44	-0.22	<1e-6	0.01
	ESVI	0.01	-0.12	0.06	0.09	0.01
	CI	-0.03	0.29	-0.15	<1e-5	0.01
	DBP	-0.01	0.10	-0.05	0.18	0.01
	MBP	-0.00	0.02	-0.01	0.79	0.01
	SBP	0.01	-0.07	0.03	0.33	0.01
	PP	0.01	-0.14	0.07	0.05	0.01
	Brain volume	-0.07	0.81	-0.40	<1e-6	0.01
	Ventricles volume	0.06	-0.70	0.35	<1e-6	0.01
	WMHs	0.05	-0.63	0.31	<1e-6	0.01
	# **WMHs**	0.04	-0.44	0.22	<1e-6	0.01
MMSE	$\boldsymbol{\sigma_0}$	0.05	-1.53	0.16	<1e-6	0.01
	C_1	0.01	-0.24	0.02	0.48	0.01
	R_p	-0.03	0.82	-0.08	0.02	0.01
	τ	0.02	-0.56	0.06	0.10	0.01
	EF	0.05	-1.43	0.15	<1e-4	0.01
	EDVI	0.03	-0.77	0.08	0.02	0.01
	SVI	0.05	-1.42	0.15	<1e-4	0.01
	ESVI	-0.01	0.38	-0.04	0.27	0.01
	CI	0.03	-0.74	0.08	0.03	0.01
	DBP	0.02	-0.48	0.05	0.16	0.01
	MBP	0.01	-0.25	0.03	0.46	0.01
	SBP	-0.00	0.07	-0.01	0.84	0.01
	PP	-0.01	0.37	-0.04	0.28	0.01
	Brain volume	0.11	-3.06	0.31	<1e-6	0.01
	Ventricles volume	-0.11	2.99	-0.31	<1e-6	0.01
	WMHs	-0.08	2.27	-0.23	<1e-6	0.01
	# **WMHs**	-0.05	1.45	-0.15	<1e-6	0.01

The association of brain volumetric data and the imputed cardiac features with the cognitive scores (ADAS11, CRSB, and MMSE) was assessed through ordinary least squares (OLS) regression analysis. Figure 5.2 presents some of the most significant associations of the imputed parameters with ADAS11. We can observe a positive association with the peripheral resistance, R_p, and a negative correlation with the cardiac index (CI), the ejection fraction (EF) and the left ventricle contractility, σ_0. The complete set of relationships can be seen in Table 5.3. The results highlight a significant association between the three cognitive scores and all brain volumetric features (GM, WM, ventricles and WMHs volumes) and to the cardiac indicators of contractility, σ_0, ejection fraction, and stroke volume index.

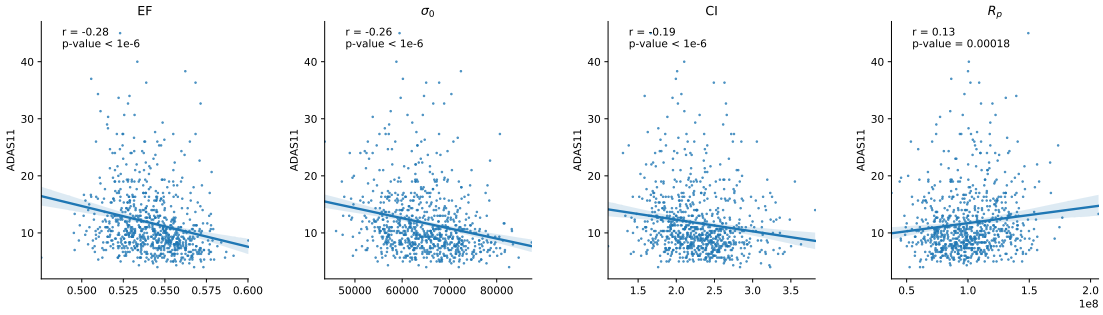

Fig. 5.2.: Correlations between imputed cardiovascular model parameters and ADAS11 cognitive score. EF, ejection fraction; σ_0 left ventricle contractility; CI, cardiac index; R_p, peripheral resistance.

5.3.2 Disease evolution

Figure 5.3 shows the trajectories of biomarkers along the estimated time-scale associated to the disease evolution along with their confidence intervals (in red). Each colored segment represents an individual, where the color represents (controls in orange, MCI in green, and AD subjects in blue). We can see how the brain volume or the cardiac contractility decrease early, while cognitive scores such as ADAS11 or CDRSB change late. The timepoint at which each biomarker is associated with maximum rate of change can be identified by quantifying the temporal derivative of the progression. Based on these timepoints, we can rank the biomarkers relatively to each other and obtain a disease evolution timeline, as shown in Figure 5.4a. The error lines around each dot indicate the uncertainty in the timepoint estimation, while the size of the dot indicates the magnitude of the change. It is worth nothing that biomarkers with small change in magnitude usually present high uncertainties, mostly because the associated progression is flat, as can be seen in Figure 5.3k for the SBP. On the other hand, biomarkers with large magnitude changes and low uncertainties present trajectories in which we can appreciate their transition towards pathological stages, as can be seen in the trajectories of the left ventricle contractility (Figure 5.3p) or ADAS11 (Figure 5.3a).

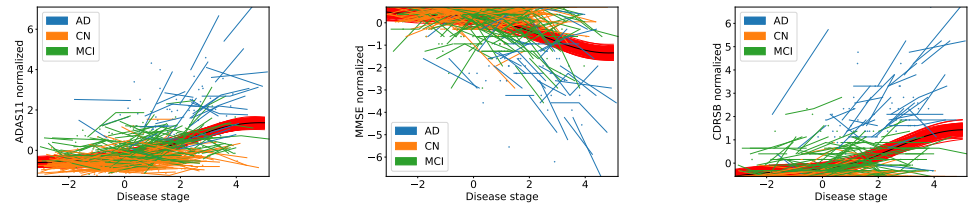

(a) ADAS11 (b) MMSE (c) CDRSB

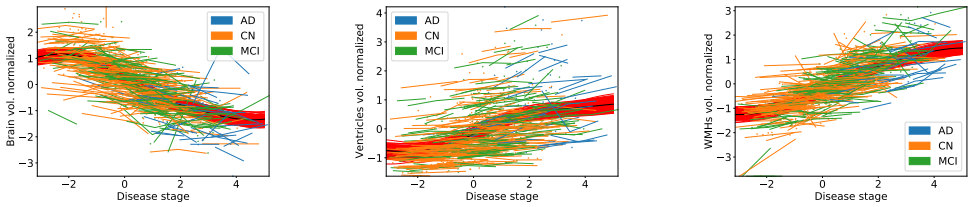

(d) Brain volume (e) Ventricles volume (f) WMHs volume

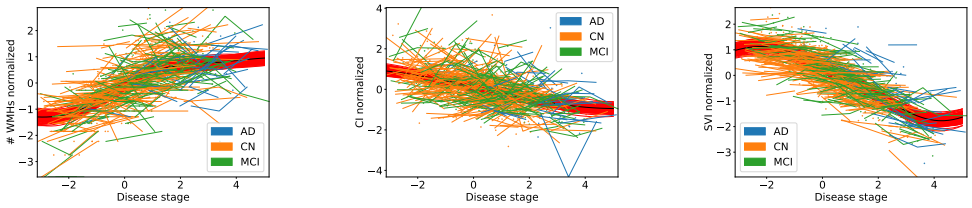

(g) Num. WMHs (h) CI (i) SVI

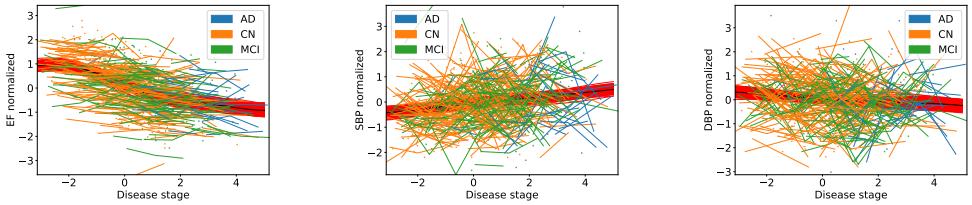

(j) EF (k) SBP (l) DBP

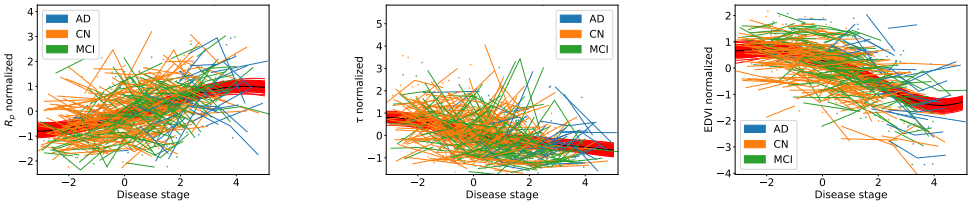

(m) R_p (n) τ (o) EDVI

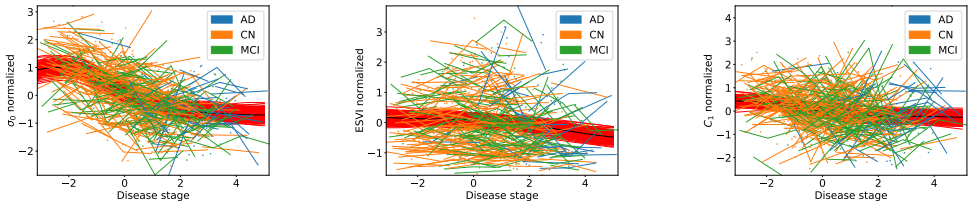

(p) σ_0 (q) ESVI (r) C_1

Fig. 5.3.: Progression of the biomarkers. ADAS, Alzheimer's disease assessment scale; MMSE, mini-mental state examination; CRSB, Clinical dementia rating scale-sum of boxes; WMHs, white matter hyperintensities; CI, cardiac index; SVI, stroke volume index; EF, ejection fraction; SBP, systolic blood pressure; DBP, diastolic blood pressure; R_p, peripheral resistance; τ, compliance main arteries; EDVI, end-diastolic volume index; σ_0, left ventricle contractility; ESVI, end-systolic volume index; C_1, left ventricle stiffness.

The disease evolution timeline depicted in Figure 5.4a shows changes in arterial compliance, τ, cardiac contractility, σ_0, and cardiac stiffness C_1, located early together with changes in EF and the number of WMHs. They are followed by brain morphological changes such as brain volume and brain ventricles volume. The transition from MCI to AD is mostly characterized by changes in cardiac volumes (e.g., CI, SVI, EDVI) and in the peripheral resistance, R_p. Finally, the cognitive indicators (e.g., ADAS, CDRSB and MMSE) appear late, in the AD stage.

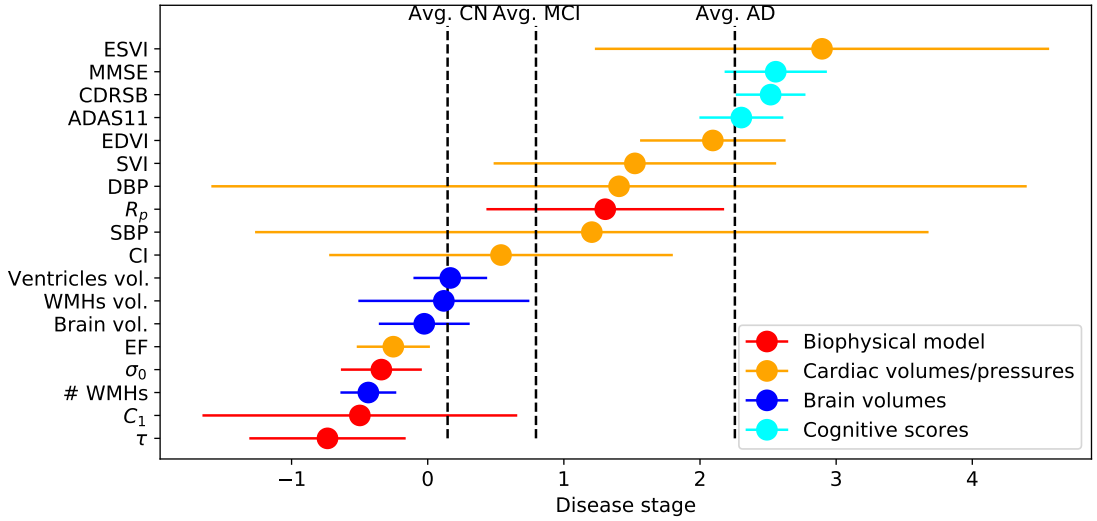

(a) Disease evolution timeline

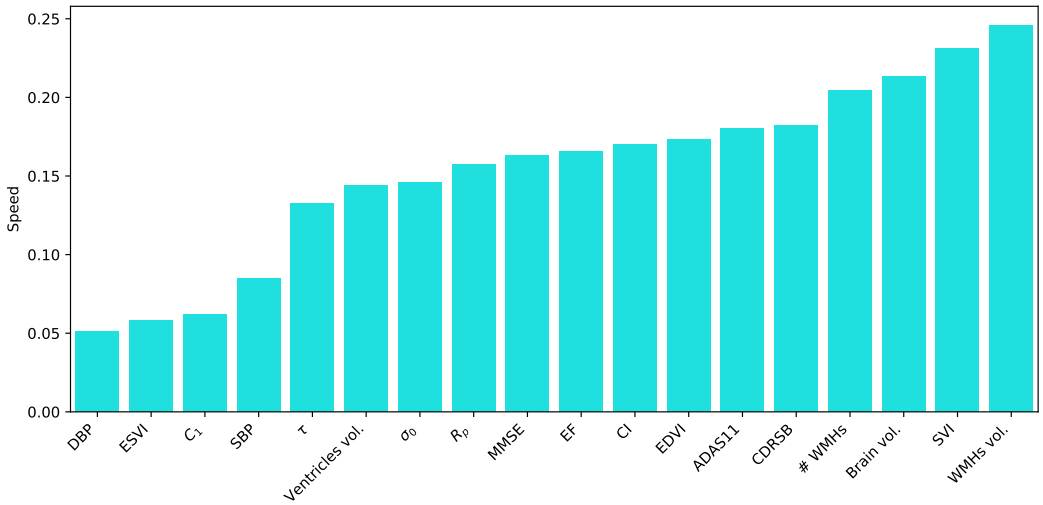

(b) Biomarkers sorted by magnitude of change

Fig. 5.4.: a) Positional diagram based on the moment at which the rate of change of each biomarker is maximum, indicated by the dot. The error lines indicate the uncertainty in the estimation. The size of the dot is proportional to the magnitude of change. The dotted lines represent the average disease stage associated to each of the clinical groups (CN, MCI, AD). The biomarkers in red are the parameters of the cardiovascular model, the biomarkers in blue are the brain morphological features, in yellow the heart volumes and blood pressures, and in cyan the cognitive scores. b) Biomarkers ordered by magnitude change.

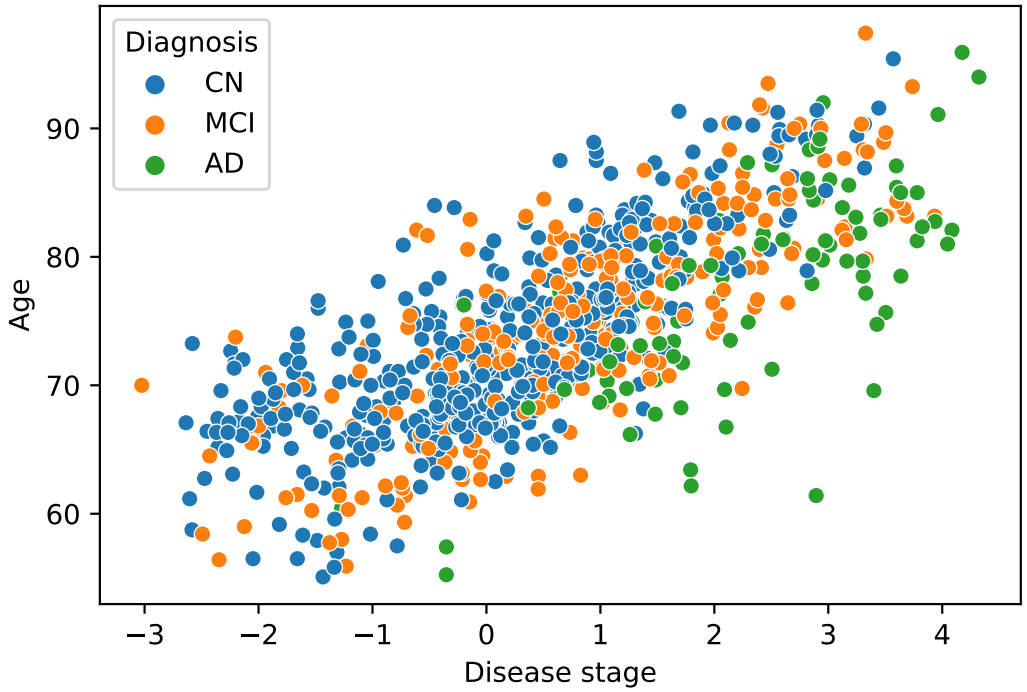

(a) Age vs disease stage

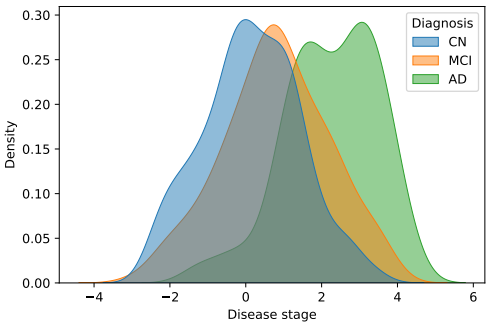

(b) Disease stage distribution

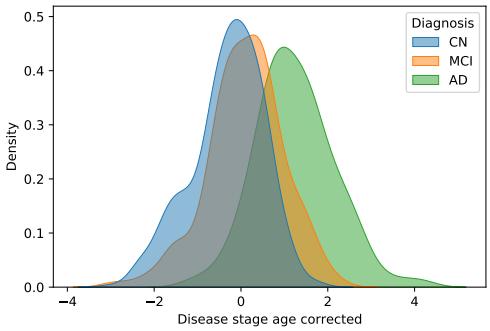

(c) Disease stage after regressing out age

Fig. 5.5.: a) Age vs estimated disease stage b) Disease stage distribution stratified by diagnosis c) Distribution of disease stage after regressing out age.

Figure 5.5b displays the distribution of the estimated disease stage for each clinical group. We can see how, in general, AD subjects are re-positioned later in the time-scale, controls are early and MCI partially overlap between the two groups. Figure 5.5a shows a high correlation between the estimated disease stage and age. Therefore, we regressed out age from the estimated disease stage to assess its effect. As can be seen in Figure 5.5c, the distributions of the age-corrected disease stage stratified by clinical group presents a similar pattern as the one observed before age correction. This result highlights that the estimated disease stage contains disease-specific information regardless of subject's age.

5.3.3 Relationship of estimated disease stage with CSF/PET biomarkers

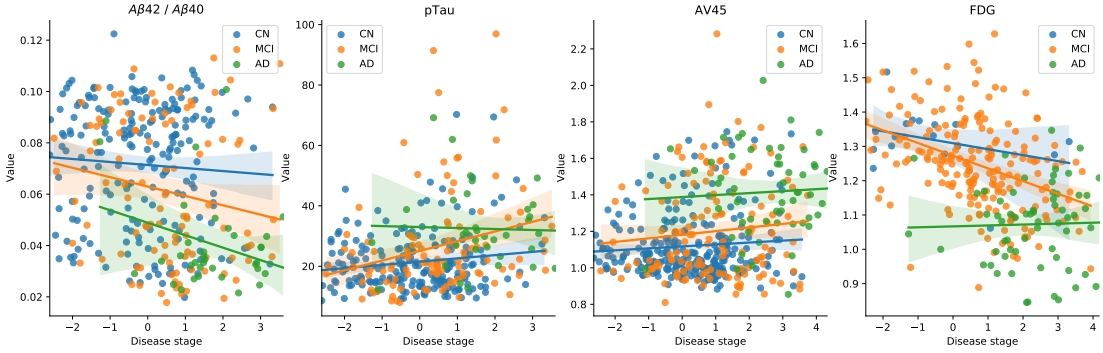

(a) Disease stage

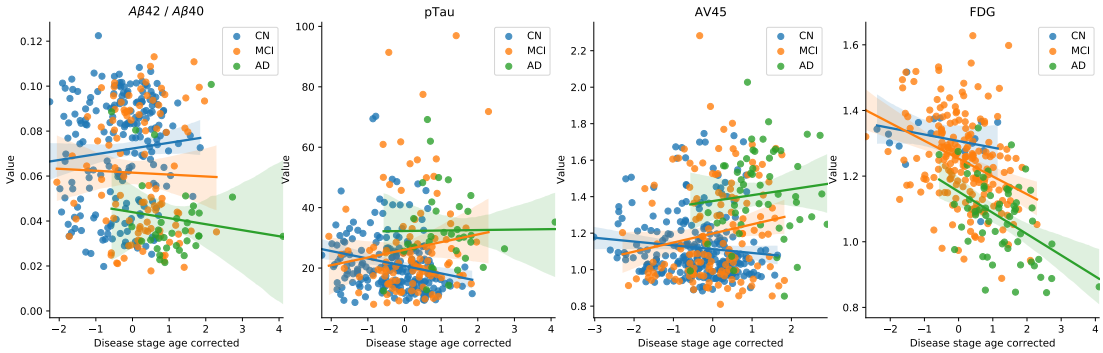

(b) Disease stage after regressing out age

Fig. 5.6.: Correlations of the CSF and PET biomarkers with a) disease stage b) disease stage after regressing out age.

The association between CSF/PET biomarkers and the estimated disease stage was studied by means of ordinary least squares (OLS) regression. The significance was assessed through a two-sided Wald test in which the null hypothesis is that the slope is 0, the significance level was set to $\alpha = 0.05$ Bonferroni corrected. Figure 5.6a represents the correlation between a subset of CSF/PET biomarkers and the estimated disease stage, while Figure 5.6b illustrates their correlations with the residual after age regression. The complete set of correlations between CSF/PET biomarkers and the estimated disease stage before and after age corrections is available at Table 5.4. We can see how the disease stage is significantly associated to AV45, FDG, $A\beta42$, $A\beta42/A\beta40$, Tau and pTau. When we correct by age the disease stage is no longer significantly associated to Tau biomarkers, but becomes significantly associated to $A\beta40$. When stratified by diagnosis the disease stage is significantly associated with FDG at the MCI stage, while when corrected by age it is associated to FDG at MCI and AD stages, and to $A\beta40$ in the CN group.

Tab. 5.4.: Correlations between the time shift and the residual after age regression with CSF and PET biomarkers. We used ordinary least squares (OLS) regression and the data was normalised to 0 mean and unit variance for better interpretability. Bold features indicate a significant statistical association for which the slope is different from 0 (Wald test). The significance level was set to $\alpha = 0.05$ corrected by Bonferroni factor of 28.

		Disease stage					Disease stage age corrected				
Diagnosis	Feature	Slope	Intercept	Correlation	p-val	Std. error	Slope	Intercept	Correlation	p-val	Std. error
All	**AV45**	**0.25**	**-0.02**	**0.26**	**<1e-6**	**0.04**	**0.21**	**0.01**	**0.22**	**<1e-6**	**0.04**
	FDG	**-0.45**	**0.12**	**-0.47**	**<1e-6**	**0.05**	**-0.51**	**0.18**	**-0.53**	**<1e-6**	**0.05**
	Aβ40	-0.03	-0.01	-0.03	0.55	0.06	**-0.23**	**0.00**	**-0.22**	**4e-5**	**0.05**
	Aβ42	**-0.20**	**-0.05**	**-0.19**	**5e-4**	**0.06**	**-0.21**	**0.00**	**-0.20**	**1e-4**	**0.05**
	Aβ42/Aβ40	**-0.25**	**-0.06**	**-0.24**	**<1e-5**	**0.05**	-0.14	0.00	-0.14	1e-3	0.06
	Tau	**0.28**	**0.07**	**0.27**	**<1e-6**	**0.05**	0.10	-0.00	0.10	0.08	0.06
	pTau	**0.27**	**0.07**	**0.25**	**<1e-6**	**0.06**	0.09	-0.00	0.09	0.11	0.06
CN	AV45	0.07	-0.24	0.08	0.20	0.05	-0.09	-0.28	-0.10	0.09	0.05
	FDG	-0.17	0.59	-0.32	0.21	0.13	-0.13	0.64	-0.26	0.32	0.13
	Aβ40	-0.02	0.08	-0.02	0.77	0.08	**-0.29**	**0.00**	**-0.25**	**4e-4**	**0.08**
	Aβ42	-0.07	0.17	-0.07	0.35	0.08	-0.09	0.18	-0.08	0.24	0.08
	Aβ42/Aβ40	-0.07	0.20	-0.06	0.37	0.07	0.09	0.27	0.09	0.20	0.07
	Tau	0.10	-0.15	0.12	0.10	0.06	-0.19	-0.25	-0.22	1.5e-3	0.06
	pTau	0.12	-0.15	0.14	0.05	0.06	-0.18	-0.26	-0.21	3e-3	0.06
MCI	AV45	0.12	0.06	0.10	0.24	0.11	0.21	0.08	0.17	0.05	0.11
	FDG	**-0.36**	**0.27**	**-0.38**	**<1e-6**	**0.06**	**-0.36**	**0.28**	**-0.34**	**<1e-6**	**0.07**
	Aβ40	0.04	-0.05	0.04	0.69	0.11	-0.06	-0.05	-0.05	0.64	0.12
	Aβ42	-0.10	-0.14	-0.09	0.34	0.11	-0.03	-0.13	-0.03	0.79	0.12
	Aβ42/Aβ40	-0.20	-0.17	-0.18	0.07	0.11	-0.03	-0.14	-0.03	0.79	0.12
	Tau	0.34	0.16	0.27	5e-3	0.12	0.19	0.09	0.14	0.16	0.13
	pTau	0.36	0.22	0.26	7e-3	0.13	0.19	0.15	0.13	0.20	0.15
AD	AV45	0.07	0.91	0.05	0.70	0.17	0.13	0.84	0.11	0.44	0.17
	FDG	0.03	-0.96	0.03	0.84	0.13	**-0.42**	**-0.39**	**-0.46**	**<1e-4**	**0.10**
	Aβ40	0.26	-0.52	0.24	0.16	0.18	-0.24	-0.06	-0.24	0.17	0.17
	Aβ42	-0.05	-0.78	-0.07	0.68	0.12	-0.08	-0.72	-0.13	0.46	0.11
	Aβ42/Aβ40	-0.27	-0.73	-0.30	0.08	0.15	-0.10	-0.81	-0.12	0.49	0.14
	Tau	0.18	0.63	0.11	0.54	0.29	0.02	0.74	0.01	0.94	0.27
	pTau	-0.04	0.66	-0.03	0.87	0.22	0.01	0.62	0.01	0.95	0.20

5.4 Discussion

In this work, we investigated the imputation of missing cardiac information that was not available in the brain-focused ADNI dataset, including in-silico parameters of a mechanistic model reflecting cardiac physiological properties. We found significant differences between groups (e.g., controls, MCI and AD) in the brain imaging features and the cardiac imputed biomarkers, in particular in the left ventricle contractility and ejection fraction. Moreover, we presented for the first time a data-driven model of Alzheimer's disease evolution which includes cardiac information. The estimated disease stage for every subject is correlated with CSF/PET biomarkers, in particular to FDG at MCI and AD stage.

The disease evolution presented in Figure 5.4 suggests that cardiac biomarkers may change early in the disease progression, prior to brain morphological changes and to

cognitive performance. These results are in agreement with the hypothetical disease evolution proposed by Sweeney et al. [Sweeney, 2018] in which vascular alterations can be detected prior to brain abnormalities. Indeed, previous studies have shown that the control of hypertension in mid-life reduces the risk of dementia [Lane, 2019; Ding, 2020].

Interestingly, the total number of WMHs is located very early in the timeline, even before the total volume of WMHs. Recently, different studies [Dagres, 2018; Sepehri Shamloo, 2020] suggested mechanisms through which atrial fibrillation (AF) and heart arrhythmias could contribute to cognitive decline. AF could lead to thrombus formation resulting in silent infarcts. Additionally, the increase in beat-to-beat variability may lead to a decrease in the cardiac output and the consequent reduction in cerebral blood flow. These processes would eventually lead to brain morphological changes, such as the reduction of brain volume or the increase in lateral ventricle volume, explaining associations found in clinical studies in which brain morphological changes were associated to reduced cerebral blood flow [Jefferson, 2009]. Eventually, the accumulation of brain damage accelerates cognitive decline and finally results in the worsening of the cognitive scores.

Therefore, the obtained timeline matches with the suggested mechanisms in which heart arrhythmias, and in particular AF, have been linked to cognitive decline [Diener, 2019]. Moreover, temporal trends reported by the Framingham Heart Study showed a decline in the risk of dementia associated with AF and heart failure over three decades (1970s - 2010s), possibly due to the improved treatment of risk factors in individuals with cardiac diseases [Satizabal, 2016; Dagres, 2018].

Nevertheless, we acknowledge that the conclusions drawn from the estimated timeline need to be corroborated by further validation. Our work presents some limitations. Since cardiac data was not actually available in ADNI, our study was based on a model trained in the complete heart-brain UK Biobank dataset. Despite the clinical plausibility of the found associations, the lack of ground truth information in ADNI prevents the quantitative assessment of the imputation accuracy, which might be biased towards the UK Biobank data. Moreover, due to the limited availability of CSF/PET biomarkers in ADNI3, they have not been included in the disease progression modelling. However, this point can be addressed in the near future as soon as new timepoints are available. Finally, it could be possible to extend the current analysis to ADNI2 data, but the MRI protocol acquisition differences may include another source of non-quantifiable bias in the data imputation.

5.5 Conclusions

We estimated a data-driven model of the progression of AD accounting for joint cardiac information and brain morphological changes in the ADNI dataset, presenting minimal cardiac information. This work allowed to explore the influence of the cardiac function in Alzheimer's Disease and the potential role cardiovascular modelling to obtain early biomarkers for dementia. Our results suggest that cardiovascular mechanistic modelling may be of help to identify subjects with higher risk of dementia, and potentially enable the intervention at early stages of the disease. Several indicators of the cardiac function are modifiable, and therefore are potential targets to reduce or slow down the cognitive decline. We believe this work can encourage future dementia studies to consider the inclusion of cardiac imaging protocols. Nevertheless, the proposed methodology allows to take advantage of already available data and suggest potential lines of research, such as the study of the potential effect of drugs modifying cardiac function in disease evolution, or the inclusion of more detailed mechanistic models to obtain more specific biomarkers.

6 Conclusions

Contents

The main objective of this thesis was to assess the influence of cardiac function in neurodegeneration using biophysical personalised models to better understand the underlying physiological pathways between cardiovascular disease and cognitive decline. To this end, we explored how to study the heart-brain interactions in large-scale epidemiological datasets with available imaging data for both organs. Next, we tackled the problem of limited multi-organ datasets. Most frequently, pathological studies on neurodegenerative disease have limited cardiac information. Thus, we developed a probabilistic imputation framework to estimate the parameters of the cardiovascular model conditioned on the available brain information. Lastly, we used a disease progression modelling approach to study the role of cardiac function in Alzheimer's disease. The obtained results highlight the potential of cardiac model parameters as biomarkers to identify population at risk of dementia and potentially improve the subject selection for neuroprotective trials, or the patient's treatment in clinical routine practice.

In the following, we summarise the main contributions of this PhD and detail the perspectives which could be topic of future research.

6.1 Main contributions

6.1.1 Introduction of prior knowledge in multi-organ analysis

In **Chapter 3** we explored how to introduce prior biophysical knowledge in the analysis of multi-organ interactions, in particular in the analysis of the heart and brain relationship. That was done by constraining the parameter-space of the cardiac model during its personalisation using the relationship between brain features and cardiovascular model parameters. The final associations between the obtained in-silico parameters and the available brain imaging information are in line with clinical observations, such as the association between the decrease of arterial compliance and a higher burden of WMHs. Moreover, the relationships between the model parameters and the target clinical features validated the personalisation solutions, replicating physiological mechanisms, such as the increase of ejection fraction with increased contractility. In addition, we analysed a pathological population subgroup, diagnosed with atrial fibrillation, with respect to a healthy control group matched in age, sex and body surface area. We found differences associated to their impaired cardiac function, such a decreased contractility. Moreover, to the best of our knowledge this study currently represents the largest cohort of personalised subjects in a cardiovascular model (i.e., n = 3445). This work lead to a journal article currently under review in Medical Image Analysis (MedIA) and a preliminary version presented at the peer-reviewed conference FIMH in 2019 [Banus, 2019].

6.1.2 Imputation of missing data based on cardiac dynamics

In **Chapter 4** we introduced a novel methodological approach to impute missing cardiac data in datasets with limited cardiac information. We leveraged on the dynamics learned in the previous chapter to train a probabilistic imputation framework that estimates the most plausible cardiovascular model parameters conditioned on the available brain information. The model is a combination of a conditional variational autoencoder (CVAE), which imputes the missing cardiac data, and a Gaussian process (GP) regression that emulates the cardiovascular model. The experimental results on the UK Biobank dataset show that our model allows accurate imputation of missing cardiac features in datasets containing minimal heart information, e.g. systolic and diastolic blood pressures only, while jointly estimating the emulated parameters of the lumped cardiovascular model. Moreover, it allows a novel exploration of the heart-brain joint relationship by simulating the evolution of the biophysical parameters conditioned on the brain imaging features. The learned relationships were in line with the expected clinical associations, such as an increase in peripheral resistance with a higher burden of WMHs, or a decrease of the cardiac contractility with decreased brain volume. Therefore, this framework allow us to use the learned dynamics to impute additional cardiac data in datasets with limited information and study the heart-brain relationship in pathological studies. This work was presented at the peer-reviewed conference MICCAI in 2020 [Banus, 2020].

6.1.3 Biophysical parameters as biomarkers for risk stratification

In **Chapter 5** we used the developed model personalisation and imputation framework, together with disease progression modelling, to estimate the long-term evolution of Alzheimer's Disease biomarkers, including the imputed parameters corresponding to the biophysical cardiovascular model. This allowed to study the role of the cardiac function in AD, and assess the potential of cardiovascular model parameters as biomarkers to identify population at risk of dementia. The estimated data-driven timeline was in line with previously proposed hypothetical disease evolutions. Our findings support that vascular changes may appear before brain abnormalities associated to neurodegeneration, and AD-specific biomarkers. Thus, the parameters of mechanistic models have the potential to be used as non-specific biomarkers to identify population at risk. We hope that these preliminary results encourage the inclusion of cardiac imaging techniques in future neurodegenerative studies.

6.2 Perspectives and future applications

6.2.1 Analysis of wave propagation effects

In our work we used a 0D (i.e. lumped) model whose haemodynamic component relies on the electronic-hydraulic analogy. However, these models do not account for spatio-temporal effects such as the pulse pressure wave propagation in the distal arteries. Nevertheless, as noted in the physiological section of Chapter 2, the stiffening of the main arteries leads to increased pulse pressure and non-attenuated pulsatile flow in the microvasculature, which can result in microvascular damage. Indeed, as introduced in the clinical context, there is a large number of clinical evidence relating arterial stiffening with impaired cerebral blood flow and brain vascular lesions associated to microvasculature damage. Therefore, it would be interesting to apply the developed tools in this PhD with a 1D model that accounts for pressure wave propagation effects. This would enable to study the role of the arterial stiffening in neurodegeneration.

6.2.2 Multi-organ analysis

Recent studies have pointed out that high salt diet (HSD) mediates cognitive impairment through tau phosphorilaton, independently of blood perfusion [Faraco, 2019]. The mechanisms by which HSD leads to tau phosphorylation starts in the small intestine, where HSD induces an increase in the circulating aminoacid IL-17. IL-17, in turn, suppresses endothelial nitric oxide (NO) production and this NO deficit results in a

cascade of events that lead to tau phosphorylation, which is ultimately responsible for cognitive dysfunction. Additionally, the NO deficit will eventually impair blood perfusion triggering additional neurodegeneration. Moreover, it has been seen that HSD is independently associated to a number of cardiovascular risk factors [Baldo, 2015]. Hence, intestinal metabolic activity may play a key role in heart-brain interactions. Furthermore, it is known that cardiac function and CSF flow are influenced by respiratory rhythms, adding another layer of complexity into the analysis. Therefore, it would be interesting to see if multiple biophysical models of each individual organ but constrained for example with the same external data could be linked together and lead to meaningful, clinically plausible solutions. In combination with our work in Chapter 4, multiple emulation models could be trained and linked together to study the evolution of the models parameters conditioned on common external features.

6.2.3 Effect of drugs in longitudinal trajectories and personalised treatment

It would be interesting to explore the effect of drugs used to regulate cardiovascular risk factors in the longitudinal trajectory of a given subject. As stated in the introduction, the incidence of dementia in the developing countries has fallen, but clinical trials in which the population has been selected based on cardiovascular risk factors, have not shown any definitive result. Hence, it is needed to understand which specific factors must be targeted. These factors could be determined by studying which biomarkers modify the subject's longitudinal trajectory. Moreover, this would enable to identify biomarkers that can act as end-point surrogate in neuroprotective trials, which would reduce the number of years required to assess the trial outcome. The effect of the drug treatment could be simulated by modifying the parameters of the mechanistic model. Moreover, given the multifactorial and complex pathophysiological nature of dementia, it is possible that the treatment varies from subject to subject. Hence, the use of mechanistic approaches could help to personalise the treatment and select the most efficient drug for each subject.

6.2.4 Analysis of CSF and blood flow coupling

As introduced in the Heart & Brain physiology Chapter the dynamics of cerebrospinal fluid (CSF) flow are intertwined with the heart cycle. Mechanically, the CSF serves as spatial buffering system. Due to the limited volume inside the skull when the heart pumps arterial blood into the brain, space has to be made for this arterial blood, partly by venous blood leaving, and partly by CSF leaving. Thus, the CSF pulsatile flow is generated by the contraction of the ventricles induced by the vascular expansion, although the exact mechanisms are under debate [Linninger, 2016]. Moreover, CSF acts functionally as a drainage system for waste and inflammatory byproducts, regulating

the composition of the interstitial fluid, and providing a route through which certain chemical messengers can be widely distributed throughout the nervous system [Ray, 2019]. The drainage of waste is likely to occur most actively within the perivascular spaces located in sensitive areas of the brain [Xie, 2013; Iliff, 2013]. Currently, enlarged perivascular spaces are considered to reflect an accumulation of waste products and are considered as a pathological biomarker [Wardlaw, 2020]. Thus, perivascular space function is important for maintaining brain health. However, the exact mechanisms driving the perivascular flow and its role in waste removal are unknown and a current source of controversy. Nevertheless, in general it is thought that vasomotion and/or arterial pulsations may play a key role in it [Agarwal, 2021; Mestre, 2020; Veluw, 2020]. In this context, precise modelling of CSF dynamics and its coupling with blood flow can aid to obtain new insights related to brain clearance mechanisms through the study of its connection with perivascular flow, testing the mechanistic plausibility of different clinical hypotheses. With that goal we initiated the development of a CFD solver based on the lattice Boltzmann method (LBM) which is introduced in the Appendix.

Overall, the obtained results in this thesis open new research directions, such as the use of more complex mechanistic models that allow to better characterise the heart-brain relationship, as exemplified by the development of our LBM solver. Other directions might involve the study of individuals longitudinal trajectories by modifying parameters of the mechanistic model, or the integration of biophysical models from different organs.

Appendices

A

Implementation of a Lattice Boltzmann Solver to Study CSF flow dynamics

The content presented in this Chapter is ongoing work and motivated by the tight relationship between the dynamics of cerebrospinal fluid (CSF) flow with the heart cycle, as introduced in the Heart & Brain physiology Chapter. We present a brief literature review on the work done studying the CSF flow and the Lattice Boltzmann Method (LBM), a numerical method that can be used to simulate computational fluid dynamics (CFD). The main goal of this Chapter is to introduce our implementation of the LBM and how we plan to use it to study the CSF-blood flow coupling. The discussion of the Navier-Stokes equations, the LBM and its associated computational aspects come mainly from the following books: [Krüger, 2017; Succi, 2018].

A.1 Introduction

CSF fills and flows through the ventricles as well as the cranial and spinal subarachnoid spaces (SAS), a schematic showing the CSF flow circulation is available at Figure 2.9. Usually, it is considered that the flow of CSF is induced by a constant production and clearance of CSF, which creates a volumetric bulk flow, and a more important pulsatile component closely related to the cardiac cycle and the respiratory motion [Ray, 2019]. However, the production and clearance of CSF is a controversial topic [**Linninger201a6**]. The classic view states that CSF is produced at the choroid plexus of the ventricles and drained trhough the venous sinuses. Alternative hypotheses point towards a CSF production and reabsorption throughout the parenchyma, which would result into a null bulk component due to production or clearance [Orešković, 2010]. Nevertheless, the classic view of choroidal production also contemplates a fraction of CSF secreted from brain tissue into the ventricles, originating from the interstitial fluid (ISF), and moving through the extracellular space (ECS). This has promoted the view of the brain as a sponge and applications of porus media theory to the biomechanics of the brain [Vardakis, 2013; Goriely, 2015]. Another controversial topic is perivascular flow [Mestre, 2020]. Penetrating arterioles from the brain surface present a fluid-filled conduit along them, as seen in Figure 2.7c. Experimental evidence suggests that perviascular flow is involved in brain waste clearence [Iliff, 2013; Xie, 2013]. Therefore, a better understanding of it

could be key in neurodegenerative diseases such as Alzheimer's disease (AD) [Wardlaw, 2020]. Nevertheless, currently the driving forces behind perivascular flow are unknown [Bothwell, 2019; Thomas, 2019], although it is speculated that arterial pulsatility may play an important role [Agarwal, 2021; Mestre, 2020].

In general pulsatile CSF oscillations are believed to be driven by systolic vascular dilatation followed by diastolic contraction. Some imaging studies have recorded displacements of CSF and brain tissue strongly correlated with the cardiac cycle [Enzmann, 1992; Jan, 2020; Zhong, 2009; Adams, 2020], and have confirmed the flow of CSF from the cranial to the spinal SAS during systole, and from the spinal SAS back to the cranial during diastole. Since the brain is enclosed in a rigid cavity the total volume in the brain must be constant at all time, as stated in the Monroe-Kellie doctrine [Wilson, 2016]. Thus, the blood flow pumped to the head induces an increase in blood volume during systole resulting in a vascular expansion of the main arteries traversing CSF-filled spaces that triggers CSF displacement. In addition, the expansion of the microvasculature inside the brain parenchyma may induce an expansion of the brain tissue and a contraction of the ventricles inducing further CSF displacement and ISF movement [Enzmann, 1992; Linninger, 2016]. Thus, the ventricular expansion-contraction motion that propels CSF flow is believed to have two origins: 1) vascular volume dilatation transmitted through brain tissue [Linninger, 2007; Loth, 2001], 2) arise from inside the ventricles by systolic expansion of the choroidal arteries [Linninger, 2005; Howden, 2008; Bering, 1955]. In addition to arterial expansion, imaging studies have provided evidence of venous compression as an additional mechanism for maintaining stable intracranial pressures over the cardiac cycle [Adams, 2020].

Nevertheless, despite the imaging advances in the quantification of movement [Adams, 2020; Jan, 2020] and flow [Pedrizzetti, 2017], biomechanical interactions between different compartments are not fully quantified, neither understood. Thus, mechanistic modelling can be used ot obtain valuable insights to better understand and interpret in-vivo data acquired at multiple locations, scales and physiological processes [Linninger, 2016]. In the particular case of fluid motion, most of the time the mechanistic models rely on the conservation of mass, momentum and energy, all together form a system of equations known as Navier-Stokes equations (NSE). Solving these equations is not trivial, and usually numerical approximations such as finite-element methods (FEM) or finite differences (FD) are used [Tangen, 2015]. These numerical methods together with boundary conditions (BC) obtained from imaging data can be used to simulate patient-specific scenarios [Feiger, 2019].

In general, to obtain patient-specific 3D simulations of the CSF flow a number of elements are required: 1) phase-contrast MRI, or analog measurements to obtain CSF and blood flow temporal profiles at specific locations; 2) high-resolution anatomical MRI to obtain accurate segmentation of the CSF pathways; and 3) a post-processing pipeline to obtain a

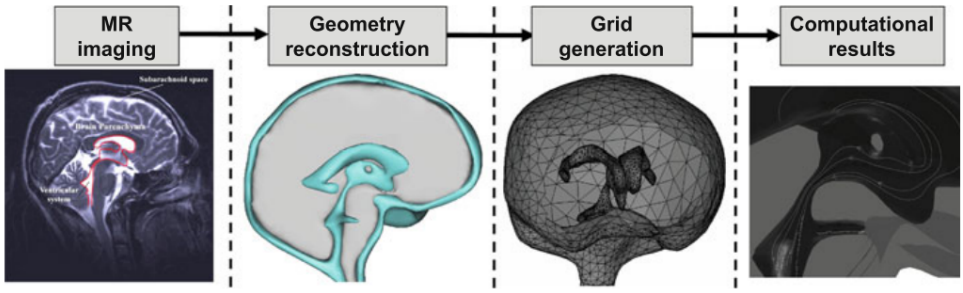

Fig. A.1.: Schematic workflow for developing a computational model of the CSF circulation. Reprint with authorisation from [Sweetman, 2011]

mesh suitable to carry out FEM or FD simulations. This process is illustrated schematically in Figure A.1. Most of the work in the literature has been carried out according to this workflow [Sweetman, 2011; Linninger, 2005]. However, it requires a lot of expert labor to obtain suitable computational models, and the simulations are computationally expensive. Therefore, approaches that allow to reduce or avoid some of these steps without compromising the simulations accuracy would be of interest. In this context, the lattice boltzmann method (LBM) has emerged as a potential alternative in the last years [Randles, 2015]. LBM is a computational model that allows to obtain CFD simulations from grid-lattice structures. Thus, it opens the possibility to obtain simulations directly in the segmented voxels, avoiding the time-consuming post-processing steps needed to obtain suitable meshes for classical numerical approaches.

The chapter is organised as follows: In section A.2 we discuss the Navier-Stokes equations and the associated challenges. In section A.3 we introduce the LBM, the computational aspects needed to take into account and our implementation. Next, in Section A.4 we present the tests and analyses used to validate our 2D implementation of LBM. To conclude, in Section A.5 we talk about future perspectives and how we plan to use the implemented solver to study the CSF-blood flow coupling.

A.2 Navier-Stokes equations

The motion of fluids can be described by mass, energy and momentum conservation. The resulting system of equations can be used to determine the velocity vector field that applies to a fluid given a set of initial conditions. However, they result in a non-linear system that induces turbulence and inpredictability in the equations, unless simplifications are applied.

A.2.1 Conservation of mass

The conservation of mass comes from the continuity equation,

$$\frac{d}{dt}\rho + \nabla \cdot (\rho\vec{u}) + Q = 0 \tag{A.1}$$

Where Q represents the external influx or efflux of mass into the system, and $\rho[kg/m^3]$ is the fluid density. Assuming incompressible fluids (ρ is constant, $d\rho/dt = 0$), and that no mass is added nor removed from the system ($Q = 0$), we obtain the conservation of mass:

$$\nabla \cdot \vec{u} = 0 \tag{A.2}$$

From now on, we will assume incompressible fluids.

A.2.2 Conservation of momentum

The conservation of momentum comes from Newton's second law: $\vec{F} = m\vec{a}$, and we can consider the action of forces and acceleration by volume: $\rho = m/v$, and $\vec{b} = \vec{F}/v$. Therefore, we can write the conservation of momentum as:

$$\vec{b} = \rho\frac{d}{dt}\vec{u}(x, y, z, t) = \rho(\frac{d\vec{u}}{dt} + \vec{u} \cdot \nabla\vec{u}) \tag{A.3}$$

Where the term $\frac{d\vec{u}}{dt} + \vec{u} \cdot \nabla\vec{u}$ is the material derivative $D\vec{u}/Dt$. We can see that we have two types of acceleration, a temporal one ($\frac{d\vec{u}}{dt}$) and a convective one ($\vec{u} \cdot \nabla\vec{u}$), associated to the inertial forces.

The body force on the fluid can be divided in two components $\vec{b} = \nabla \cdot \sigma + \vec{f}$. Where, σ accounts for fluid stresses and $\vec{f}$ for external forces. The divergence of the stress tensor is added to account for possible sink or sources of fluid. Thus, the stress tensor σ, can be divided in two terms: a volumetric tensor defining changes in the whole volume, which is approximated by the pressures. And a deviator tensor, accounting for the body deformations, which can be approximated by the shear stress. Hence, the stress tensor can be written as:

$$\sigma = -\begin{pmatrix} P & 0 & 0 \\ 0 & P & 0 \\ 0 & 0 & P \end{pmatrix} + \begin{pmatrix} \sigma_{xx} + P & \tau_{xy} & \tau_{xz} \\ \tau_{yx} & \sigma_{yy} + P & \tau_{yz} \\ \tau_{zx} & \tau_{zy} & \sigma_{zz} + P \end{pmatrix} = -PI + T \tag{A.4}$$

Where T_{ab} is the stress in a plane perpendicular to a in direction b, and σ_{aa} is the normal stress in the a direction. Using this equality we can define the most general form of the NSE:

$$\rho \frac{D\vec{u}}{Dt} = \nabla \cdot (-PI + T) + \vec{f} = -\nabla P + \nabla \cdot T + \vec{f} \tag{A.5}$$

In a *Newtonian fluid* the stress is proportional to the rate of deformation, i.e: to the change of velocity in the direction of stress, we can see it as the 'drag' of the fluid. Formally, the shear stress is determined by the derivative in perpendicular direction of the velocity component parallel to the direction of shear. For isotropic cases:

$$\tau_{ij} = \mu(\frac{du_i}{dx_j} + \frac{du_j}{dx_i}) \tag{A.6}$$

Where $\mu[kg/(m\ s)]$ is the dynamic or shear viscosity, it determines how easily fluid flows when subject to body forces, i.e: the force needed to move the fluid at a certain rate. For some non-Newtonian fluids, power-law fluids, the shear stress is raised to an exponent n, such that $\tau = \mu(\frac{du}{dy})^n$. In this case, we can recover the Newtonian case for $n = 1$. If $n < 1$ we talk about pseudoplastic behavior; as τ increases there is a decrease in dynamic viscosity. For example, this happens in blood as it reaches the capillaries. Assuming an incompressible fluid, the stress tensor in Equation A.4 can be re-calculated using the viscosity and we obtain:

$$\begin{cases} \nabla \cdot \sigma = \mu \nabla^2 \vec{u} - \nabla P, \\ \mu \nabla^2 \vec{u} = \nabla \cdot T \end{cases} \tag{A.7}$$

Where the term $\mu \nabla^2 \vec{u}$ represents the viscous forces, and ∇P the pressure. The momentum conservation becomes:

$$\rho(\frac{d\vec{u}}{dt} + \vec{u} \cdot \nabla \vec{u}) = -\nabla P + \mu \nabla^2 \vec{u} \tag{A.8}$$

In this equation the flow behavior results form the competition between large-scale advection, the inertial component, and small scale dissipation or diffusion, the viscous forces. The ratio between them is measured by the Reynolds number, Re:

$$Re = \frac{\rho \vec{u} L}{\mu} = \frac{\vec{u} L}{\nu} \tag{A.9}$$

Where L is the characteristic length of the problem and $\nu[m^2/s]$ is the kinematic viscosity, which is the ratio between dynamic viscosity and density, $\nu = \mu/\rho$. At low Re, the viscous forces are dominant and the flow is laminar, while at high Re the inertial forces dominate and the flow becomes turbulent. Thus, the convective term is at the origin of the non-linearity in the NSE.

Another important number is the Mach number, Ma, it is a measure of flow compressibility defined by the ratio of fluid velocity with respect to the speed of sound, c_s, in the medium:

$$Ma = \frac{\vec{u}}{c_s} \tag{A.10}$$

The higher the Ma, the more compressible. If the fluid is not assumed to be incompressible, an equation for the mass balance and for the conservation of energy are needed together with the conservation of momentum. However, this is out of the scope of this Chapter.

A.3 LBM: Implementation and Computational aspects

The Lattice Boltzmann method (LBM) has become an attractive approach to solving the Navier-Stokes equations in numerous scenarios because it easily handles complex geometries and efficiently scales across many processors. These advantages have led to biomedical applications of the LBM such as blood flow simulations in realistic vascular geometries to model for example clot formation and deposition, or hemodynamic patterns in stented cerebral aneurysms [Feiger, 2019]. Moreover, large-scale LBM solvers focused on vascular modelling have been developed, such as HemeLB [Mazzeo, 2008] or HARVEY [Randles, 2015]. Instead of discretising the partial differential equations (PDE) of the NSE, the LBM tracks the dynamics of a fictitious set of representative particles moving between the points of a regular Cartesian lattice. Hence, the boundary conditions

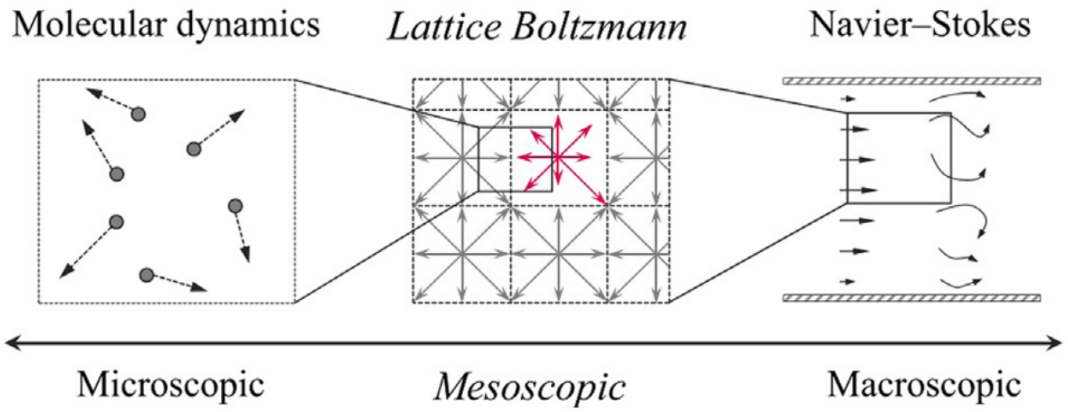

Fig. A.2.: Fluid flow properties revealed at different scales by different simulation methods, reprint from [Saito, 2021] with authorisation.

(BC) must be set with respect to the particle dynamics. The dynamics of the particles support the macroscopic fluid behavior as an emerging phenomenon, i.e: the macroscopic dynamics of a fluid are the result of the collective averaged behavior at the molecular level [Succi, 2010].

However, simulating the dynamics of every particle would be a long and expensive process. Therefore, the spatial domain is discretised on a regular finite grid of lattice nodes, the time is divided into timesteps, and each node has a set of discrete velocity directions with an associated group of molecules. Thus, each velocity direction of each node has an associated distribution function representing the grouped molecules. This procedure eliminates statistical noise in the calculations [McNamara, 1988].

The distribution functions can be indicated as: $f(\vec{x}, \vec{c}, t)$, and they represent the probability of finding a particle at location $\vec{x}$, with velocity $\vec{c}$, at a given time, t. The relations between distribution functions are regulated by the Boltzmann transport equation:

$$\frac{df}{dt} + c \cdot \nabla_{\vec{x}} f + \frac{F}{m} \nabla_{\vec{x}} f = \Omega(f) \tag{A.11}$$

The terms $\frac{df}{dt} + c \cdot \nabla_{\vec{x}} f$ represent the streaming process, i.e: the movement of particles, and the F term accounts for the external forces. The term $\Omega(f)$ is the collision operator, which regulates the interactions between particles. Its modelling is crucial since the colliding particles have to be correctly reassigned to their new trajectories. Due to the high number of unknowns present during a collision, it is not easy to fully determine the collision operator. Some approximations have to be made bearing in mind that its correct interpretation is key to grant sufficient accuracy. Thus, we consider the following hypotheses: collisions take place only between two particles, particles are independent

before and after the collision, and the collision process is instantaneous and uninfluenced by external factors.

A.3.1 Computational aspects

In the reduced NSE for incompressible fluids (Equation A.8) the Reynolds number determines the flow behavior. However, the LBM models the movement of particles. Thus, there is another number that we should consider, the Knudsen number, K_n. The K_n determines the ratio between the mean free-path of a molecule, l_u, i.e: the average distance a molecule travels before colliding with another molecule, and the length-scale of the problem (L):

$$Kn = \frac{l_u}{L}, \tag{A.12}$$

$$l_u = \frac{\nu}{c_s} \tag{A.13}$$

Thus, if the K_n is near or greater than one, the mean free-path of a molecule is comparable to the length-scale of the problem, and the continuum assumption of fluid mechanics is no longer a good approximation. The Re can be expressed by means of the Mach number and the Knudsen number:

$$Re = \frac{\vec{u}L}{\nu} = \frac{\vec{u}}{c_s}\frac{L}{l_u} = \frac{Ma}{K_n}, \tag{A.14}$$

Typically Ma is in the order of 1 or less. So, Re depends mainly on the K_n. Thus, in our simulations we measure the objects in units of free-path, l_u. An important point to consider is that the advection acts at macroscopic scales and is described by the divergence of a gradient (Laplacian), while dissipation/diffusion takes over at much smaller scales, and in kinetic theory emerge from the collisions.

These collisions act in such a way as to relax the Boltmzann distirbutions, f, to an equilibrium, f^{eq}, on a time scale that is proportional to the free-path, l_u. The local equilibrium is a Gaussian (Maxwell-Boltzmann) distribution in the velocity space which depends parametrically on the local fluid densitiy (ρ), velocity (u) and temperature (T).

$$f^{eq} = \frac{\rho}{m}(\frac{m}{2\pi k_B T})^{3/2} exp(-\frac{m(c-u)^2}{2k_B T}) \tag{A.15}$$

The equilibrium distributions are obtained when $u = 0$. This means that the relaxation process is expressed as a relaxation towards an equilibrium state of null speeds. Thus, one can state that the relaxation rate towards the equilibrium distribution function is close to the time between molecule collisions. As we seen, the parameter that relates the mean free-path with the characteristic length of the problem is the Knudsen number. Hence, we can say that K_n expresses the mean number of collisions affecting a particle in a certain time and that the collision operator simplifications are only valid for small K_n numbers.

The most common simplification for the collision operator is the one proposed by Bhatnagar-Gross-Krook (BGK) [Bhatnagar, 1954]. In the BKG assumption the distribution functions f are relaxed towards the equilibrium distributions f^{eq}, weighted by the single relaxation time (SRT), τ. Thus, the collision operator can be expressed as:

$$\Omega(f) = -\frac{f(\vec{x}, \vec{c}, t) - f^{eq}(\vec{x}, \vec{c}, t)}{\tau} \tag{A.16}$$

Where τ is a relaxation constant applied every time-step to 'relax' the distribution functions towards the equilibrium. To implement a discrete numerical method for the solution of the Boltzmann transport equation (Equation A.11), we discretise the infinite possible speed directions, c, to a finite number of speeds c_i. This discretisation is carried out in such a way that we obtain a symemtric set of velocities to ensure isotropy, and mass, momentum and energy are conserved. This allows to implement LBM through a two-step procedure, *collision* and *streaming*. While collision is local, streaming takes a value of the function and stream it in a certain direction c_i. Thus, the discretised version of Equation A.11 becomes:

$$f_i(\vec{x} + \vec{c}_i \Delta t, t + \Delta t) = f_i(\vec{x}, t) - \omega \Delta t[f_i(\vec{x}, t) - f_i^{eq}(\vec{x}, t)] \tag{A.17}$$

Where $\omega = 1/\tau$, and the distirbution f_i^{eq} is the result of a second-order expansion using Hermite polynomials in the fluid velocity space of Equation A.15 [Shan, 2006]:

$$f_i^{eq} = w_i \rho \left[1 + \frac{\vec{c}_i \cdot \vec{u}}{c_s^2} + \frac{1}{2}\left(\frac{(\vec{c}_i \cdot \vec{u})}{(c_s^2)^2} - \frac{u^2}{c_s^2}\right)\right], \tag{A.18}$$

where w_i are the weights attributed to each discretised velocity and c_s represents the speed of sound in the lattice, both determined by the Gauss-Hermite quadrature integrals of the second-order expansion of the equilibrium function in the velocity space.

The moments of the distribution functions give us the macroscopic variables, such as the fluid density, ρ, and momentum. In the discretised space, they are obtained as the sum of the directional distributions:

$$\rho = \sum_i f_i \tag{A.19}$$

$$\rho u = \sum_i c_i f_i \tag{A.20}$$

and the fluid velocity as:

$$u = \frac{1}{\rho} \sum_i c_i f_i \tag{A.21}$$

In order to obtain LBM simulations that correctly reflect the physics of the modelled system the lattice variables must be scaled accordingly. The main factor to take into account to simulate the same flow type is that the Reynolds number must be conserved. The switching from the physical system to the lattice one is performed in two steps; first the NSE are non-dimensionalised based on the characteristic length (L_0) and time-scale (t_0) of the problem. Then, the non-dimensional system is translated into lattice units through the choice of discrete time and space steps for the LBM simulation. The most common approach is to set the lattice units in terms of time and length as unitary. Thus, the discrete space step, Δx, is described as the reference length divided by the grid size used for the discretisation, N, i.e: $\Delta x = L_0/N$, and the same procedure is applied for the time step: $\Delta t = t_0/N_{iter}$.

Moreover, the kinematic viscosity is set according to which Reynolds number we aim to model. Its variation depends solely on the temperature, so in the case of isothermal flows it is constant. The viscosity in the lattice can be related to the the non-dimensional one by:

$$\nu = \nu_{LB} \cdot \Delta t/(\Delta x)^2 \tag{A.22}$$

In turn, the relaxation coefficient, τ, is related to the fluid's kinematic viscosity ν by:

$$\nu_{LB} = \frac{(\tau - 0.5)\Delta t c_s^2}{3} \tag{A.23}$$

We can observe how values of $\tau < 0.5$, will lead to negative viscosities, thus τ must be always greater than 0.5.

Finally, the application of boundary conditions depends on the type of boundary and on the macroscopic property (velocity or pressure) we want to impose. In computational fluid dynamics, inlet and outlet boundary conditions play a key role in determining the fidelity of fluid simulations. In the particular case of LBM, the main challenge consists in translating the macroscopic information to the microscopic distribution functions without affecting the numerical accuracy or stability. During the streaming step nodes close to the boundary lack some of their neighbors. Therefore, some of the distribution functions which are supposed to stream are missing. Many different inlet and outlet boundary conditions have been proposed with potentially varying accuracy and stability. However, in spite of the increasing number of applications it does not currently exist a unified scheme for implementing inlet and outlet boundary conditions. This has motivated recent works directed to the analysis of boundary conditions in complex geometries, such as image-derived vasculature geometries [Feiger, 2019].

In summary, the LBM can restore the slightly compressible NSE, small Ma, at small Knudsen numbers, i.e: close to the equilibrium. The main advantages of LBM compared to classical numerical approximations to simulate CFD are related to the possibility of handling complex geometries, and its massive parallelisation potential thanks to the local collisions. Moreover, the streaming operator is linear and does not depend on the spatial location, in opposition to the convective term of NSE. However, it also has limitations, the main one being the complexity in the definition of the boundary conditions and the associated stability issues.

A.3.2 Implementation

We implemented our LBM solver using PyTorch [Paszke, 2019], allowing us to have access to high-level parallelisation in GPU. Currently our solver handles 2D scenarios using a 2DQ9 lattice, i.e: the 2D domain is discretised in a grid of nodes with 9 possible directions. Periodic boundary conditions as well as no-slip walls ($\vec{u} = 0$) simulated through the bounce-back boundary condition are implemented. Inlet and outlet velocities and pressures can be imposed according to the Zou-He scheme [Zou, 1997]. Moreover, the contribution of external forces is supported based on the approach of Guo [Guo,

2002], and is possible to use of multiple relaxation times (MRT). In general, the procedure to obtain a CFD simulation for a given scenario is presented in the pseudo-code 3.

Algorithm 3 LBM Algorithm

Inputs:
  Domain and boundary conditions
  Simulation parameters $\leftarrow \tau$, Re, u_{LB}, N
  $k \leftarrow$ Max iterations
Returns:
  Macroscopic variables, ρ, u
Initialise:
  Non-dimensionalisation of related parameters
  Discretisation of physical domain
  Mapping of simulation parameters to the lattice grid
  Compute macroscopic variables and setting of BC
while $i < k$ **do**
  Compute macroscopic variables (includes F if not constant and non-zero)
  Collision step
  Streaming step
  Boundary conditions
  if convergence **then**
    $i = k$
  end if
  $i \leftarrow i + 1$
end while

During the non-dimensionalisation it is important to remember that in the LBM domain, the Knudsen number as well as the Mach number should be small. Usually $Kn \propto 1/N$, remembering that $K_n \propto Ma \cdot Re$. Moreover, τ must be larger than $\tau > 1/2$ in order to obtain stable solutions, as seen in Equation A.23. However, for large τ the accuracy deteriorates. In general, the simulation parameters include the grid size, N, the Reynolds number, the relaxation parameter τ, and/or the LBM velocity u_{lb}.

A.3.2.1 Lattice characteristics

As stated in section A.3.1 the lattice structure must fulfill a set of requirements, it must present a set of symmetric set of velocities to ensure isotropy and must conserve mass, momentum and energy. The weights of each lattice direction w_i are obtained by finding the weights of the Gauss-Hermite quadrature integrals of the second-order expansion of the equilibrium function in the velocity space. In our tests we have used the 2DQ9 lattice scheme, with the associated velocity magnitudes:

$$\begin{cases} c_x = [0, 1, 0, -1, 0, 1, -1, -1, 1] \\ c_y = [0, 0, 1, 0, -1, 1, 1, -1, 1] \end{cases} \tag{A.24}$$

The weights related to each discrete velocity are:

$$w_i = \begin{cases} 1/4 & \text{for } i = 0 \\ 1/9 & \text{for } i = 1, ..., 4 \\ 1/36 & \text{for} i = 5, ..., 8 \end{cases}, \tag{A.25}$$

and the speed of sound in the lattice is:

$$c_s = \frac{1}{\sqrt{3}} \tag{A.26}$$

Which is obtained by non-dimensionalising the set of velocities used in the Gauss-Hermite quadrature.

A.3.2.2 Guo Force

The discretisation of the Boltzmann equation presented in Equation A.17 conserves density and momentum but not the force. To that end, Guo introduced the formulation below:

$$f_i(x + c_i\Delta t, t + \Delta t) = \frac{\Delta t}{\tau} f_i^{eq}(x, t) + f_i(x, t)(1 - \frac{\Delta t}{\tau}) + F_i\Delta t(1 - \frac{1}{2\tau}) \tag{A.27}$$

In this formulation, the equilibrium functions are calculated with the shifted macroscopic velocity as:

$$\rho u = \sum_i f_i c_i + \frac{F\Delta t}{2} \tag{A.28}$$

A.3.2.3 MRT and TRT

The BKG assumption has an associated problem, the whole procedure depends on the parameter τ, which assumes that there is only one viscosity. In order to tackle this issue the goal is to relax the different probability distribution functions with different relaxation rates and mix them. Formally:

$$f_i(x + c_i, t + 1) = f_i(x, t) - M_{ij} f_j - f_j^{eq} \tag{A.29}$$

The matrix M should have certain properties, mainly it needs to conserve density and momentum. To achieve that the eigenvectors of M are connected to the velocity set, such that the eigenvalues are the relaxation rates. Thus, we can construct M as:

$$M_{ij} = \sum_k M_i^k s_k M_j^k, \tag{A.30}$$

where s_k are the relaxation rates and M^k is the k^{th} eigenvector. The basis vectors are obtained by means of eigenvector decomposition using Gramm-Schmidt. In the 2DQ9 case the matrix M becomes:

$$M = \begin{pmatrix} \rho \\ e \\ \epsilon \\ j_x \\ q_x \\ j_y \\ q_y \\ p_{xx} \\ p_{xy} \end{pmatrix} = \begin{pmatrix} 1 & 1 & 1 & 1 & 1 & 1 & 1 & 1 & 1 \\ -4 & -1 & -1 & -1 & -1 & 2 & 2 & 2 & 2 \\ 4 & -2 & -2 & -2 & -2 & 1 & 1 & 1 & 1 \\ 0 & 1 & 0 & -1 & 0 & 1 & -1 & -1 & 1 \\ 0 & -2 & 0 & 2 & 0 & 1 & -1 & -1 & 1 \\ 0 & 0 & 1 & 0 & -1 & 1 & 1 & -1 & -1 \\ 0 & 0 & -2 & 0 & 2 & 1 & 1 & -1 & -1 \\ 0 & 1 & -1 & 1 & -1 & 0 & 0 & 0 & 0 \\ 0 & 0 & 0 & 0 & 0 & 1 & -1 & 1 & -1 \end{pmatrix} \tag{A.31}$$

The collision matrix can be constructed from the eigenvectors matrix M as $A = M^{-1}SM$. Then, the boltzmann equation can be written as:

$$f_i(x + c_i, t + 1) = f_i(x, t) - A_{ij}(f_j(x, t) - f_j^{eq}(x, t)), \tag{A.32}$$

and we can recover the isotropic case for $A = I/\tau$. However, to reduce the number of operations in the MRT the calculation of A is typically ommited, instead the whole LBM process is multiplied by M and S is used for the relaxation, making it equivalent

to the BKG update rule but in the moment space. However, since we cannot propagate moments in the streaming step we need to use M^{-1} to obtain back the populations, f.

The MRT has more free parameters to tune the viscosity and offers a higher stability compared to BKG, a control of higher-order moments necessary for non-Newtonian fluids, and precise boundary conditions. However, is slower than BKG, and it raises the problem of how to select the different relaxation parameters. There is a subset of MRT, the two-relaxation rates (TRT) that offers a trivial solution. In TRT the model uses two relaxation times, ω_+ and ω_-. ω_+ is used for even order tensors and ω_- for odd order. It is also possible to use TRT without using MRT, in this case the populations are decomposed on positive and negative parts:

$$\begin{cases} f_i = f_i^+ + f_i^-, \\ f_i^{eq} = f_i^{eq,+} + f_i^{eq,-}, \\ f_i^+ = (f_i + f_{\bar{i}})/2, \\ f_i^- = (f_i - f_{\bar{i}})/2, \\ f_i^{eq,+} = (f_i^{eq} + f_{\bar{i}}^{eq})/2, \\ f_i^{eq,-} = (f_i^{eq} - f_{\bar{i}}^{eq})/2 \end{cases} \tag{A.33}$$

Where the subscript $\bar{i}$ stands for the index of direction opposite to the direction i. The LBE equation can be written as follows:

$$f_i(x + c_i, t + 1) = f_i(x, t) - \omega_+(f_i^+(x, t) - f_i^{eq,+}(x, t)) - \omega_-(f_i^-(x, t) - f_i^{eq,-}(x, t)), \tag{A.34}$$

All macroscopic errors/quantities of TRT depend on the so-called 'magic' parameter:

$$\Lambda = \left(\frac{1}{\omega_+} - \frac{1}{2}\right)\left(\frac{1}{\omega_-} - \frac{1}{2}\right), \tag{A.35}$$

In general in the TRT one parameter is fixed with the viscosity and the other is fixed through the magic number combination.

A.4 2D Validation of LBM simulator

A.4.1 Taylor-Green vortex decay

The Taylor-Green vortex decay is an unsteady flow of a decaying vortex, which has an exact closed solution of the incompressible Navier–Stokes equations in Cartesian coordinates. The exact 2D analytical solution is shown in Figure A.3 and is given by:

$$\begin{cases} u_x(x,y) = u_0 sin(x) sin(y) exp(-2\nu t), \\ u_y(x,y) = u_0 cos(x) cos(y) exp(-2\nu t), & \text{for } 0 < x, y < 2\pi \\ p(x,y) = p_o + 0.25 u_0^2 (cos(2x) - cos(2y)) exp(-4\nu t), \end{cases} \tag{A.36}$$

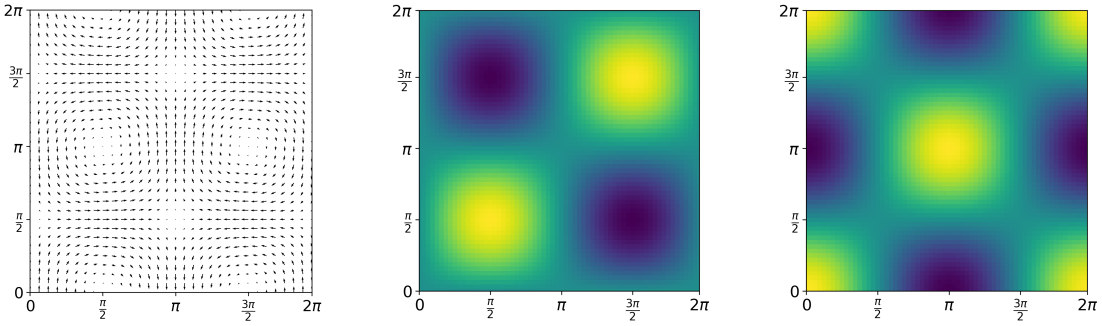

(a) Streamlines **(b)** u_x **(c)** u_y

Fig. A.3.: Analytical solution of the Taylor-Green vortex a) vector plot, b) u_x component, c) u_y component

This system of equations is an excellent benchmark to test our LBM implementation and explore the limitations of LBM. We studied the influence of the Mach number by testing different velocities u_{LB} at a given grid size, $N = 32$, and fixed relaxation step, $\tau = 1$ for 400 iterations. Thus, the increased velocity with respect to the lattice speed of sound results in higher Mach numbers. In Figure A.4 we can observe the decay of velocity with time both analytically and with the LBM. We see that at high Mach numbers the LBM becomes unstable and loses accuracy.

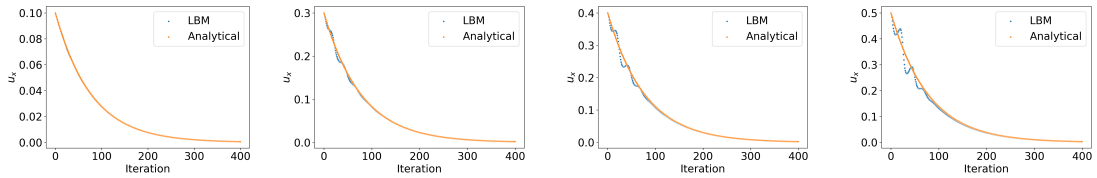

(a) $u_{max} = 0.1$ **(b)** $u_{max} = 0.3$ **(c)** $u_{max} = 0.4$ **(d)** $u_{max} = 0.5$

Fig. A.4.: Temporal evolution of u_x at $\left(\frac{\pi}{2}, \frac{\pi}{2}\right)$. Orange dots indicate the analytical solution while blue dots correspond to the LBM estimation. a) $u_{max} = 0.1$, b) $u_{max} = 0.3$ c) $u_{max} = 0.4$ d) $u_{max} = 0.5$. At high velocities we get high Mach numbers, and we can see that the LBM is not able to obtain accurate simulations.

Next, in Figure A.5 we explored the influence of τ given a fixed grid resolution, $N = 32$ and velocity $u_{LB} = 0.001$ for 400 iterations. We can see how for $\tau < 0.5$ we get negative viscosities in the LBM space, which also lead to negative viscosities in the physical domain. Thus, both analytical and LBM solutions lead to unrealistic results and the LBM becomes unstable. As we increase τ we observe how the LBM can obtain accurate solutions and we can see a faster relaxation towards the equilibrium. Nevertheless, the LBM viscosity increases as τ increases, since the other simulations parameters are fixed this implies that we are simulating flows with different Re. Thus, at high τ we cannot obtain accurate simulations for the simulated flow unless the grid discretisation is increased. In Figure A.6 we can see the 2D reconstruction of u_x at different relaxation factors, τ.

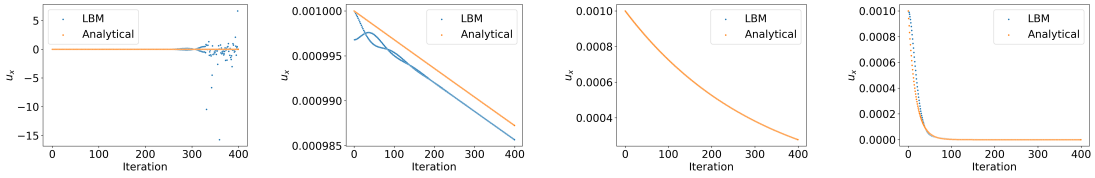

(a) $\tau = 0.49$ **(b)** $\tau = 0.505$ **(c)** $\tau = 1$ **(d)** $\tau = 10$

Fig. A.5.: Temporal evolution of u_x at $\left(\frac{\pi}{2}, \frac{\pi}{2}\right)$. Orange dots indicate the analytical solution while blue dots correspond to the LBM estimation. a) $\tau = 0.49$, b) $\tau = 0.505$ c) $\tau = 1$ d) $\tau = 10$. It is visible how at $\tau < 0.5$ the LBM is not stable and is unable to recover the actual velocity. At high τ the relaxation is too fast and it results in lose of accuracy.

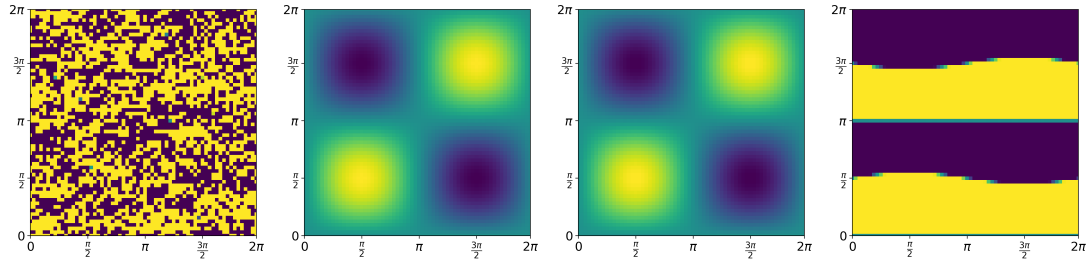

(a) $\tau = 0.49$ **(b)** $\tau = 0.505$ **(c)** $\tau = 1$ **(d)** $\tau = 10$

Fig. A.6.: Estimated u_x at different relaxation rates, τ. It is visible how at $\tau < 0.5$ the LBM is not stable and is unable to recover the actual velocity. At high τ the relaxation is too fast and it results in lose of accuracy.

A.4.2 Four rows mill

To assess the correct implementation of the force term we used the Four rows mill, a modification of the Taylor-Green flow. The forces are described as:

$$\begin{cases} F_x = 2\nu sin(x)sin(y) \\ F_y = 2\nu cos(x)cos(y) \end{cases} \tag{A.37}$$

Thus, the solution to the Navier-Stokes equations will take the form:

$$\begin{cases} u_x(x,y) = u_0 sin(x) sin(y) \\ u_y(x,y) = u_0 cos(x) cos(y) \qquad\qquad \text{for } 0 < x, y < 2\pi \\ p(x,y) = p_o + 0.25 u_0^2 (cos(2x) - cos(2y)) \end{cases} \tag{A.38}$$

We can see that they are the same as the Taylor-Green but without the time dependency. Moreover, we used this system of equations to test the implementation of the two-relaxation times (TRT). As simulation parameters we used $u_{LB} = 0.001$, grid size $N = 128$, relaxation step $\tau = 1$ for 400 iterations. For the TRT simulation we used as magic number $\Lambda = 1/4$. In Figure A.7 is visible how the analytical solution is constant, since there is no time dependency and the solution depends only on constant forces. At the same time, we can see how the SRT does not converge to a stable solution. Due to the simultaneous non-equal orthogonal forces in x and y direction at each space location the isotropic relaxation cannot recover the analytical solution. In contrast, we observe how the TRT scheme enables us to accurately simulate the anisotropic behaviour and recover the analytical solution.

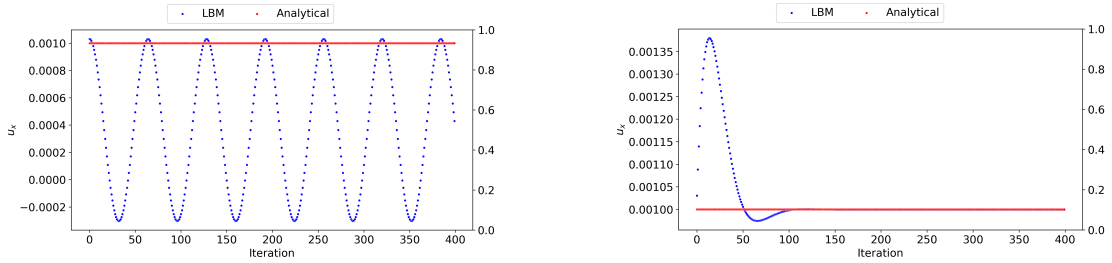

(a) SRT **(b)** TRT

Fig. A.7.: Temporal evolution of u_x at $\left(\frac{\pi}{2}, \frac{\pi}{2}\right)$. Orange dots indicate the analytical solution while blue dots correspond to the LBM estimation. a) SRT b) TRT. TRT recovers the analytical solution, while SRT is unable to converge to a stable solution.

A.4.3 Poiseuille flow

We simulated the flow between two static parallel plates to test the implementation of the Zou-He boundary condition and of the bounce-back walls. This setting generates a pressure-driven flow, known as Poiseuille flow. The velocity profile is given by equation:

$$u_x(y) = -\frac{dP}{dx}\frac{1}{2\mu} y(H - y), \tag{A.39}$$

Where H represent the distance between the plates. We can see that $u_x(y)$ describes a parabola with zeros at y and H. As simulation parameters we used $u_{LB} = 0.001$, grid

size $Ny = 32$, $Nx = 3$, relaxation step $\tau = 1$ for 1000 iterations. In Figure A.8 we can see the obtained results. We observe a parabolic flow with zeros at the walls.

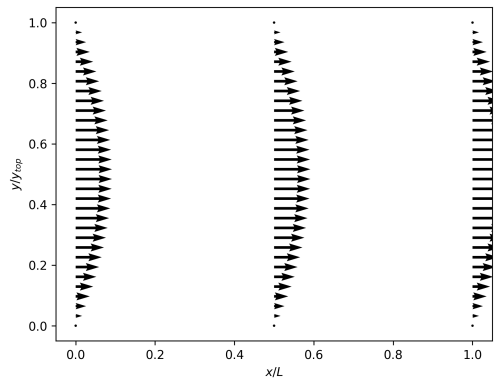

(a) Streamlines using BB

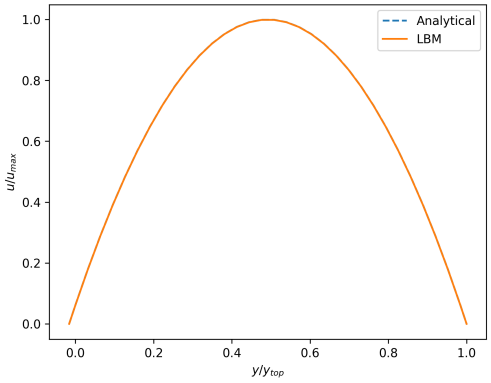

(b) Velocity profile using BB

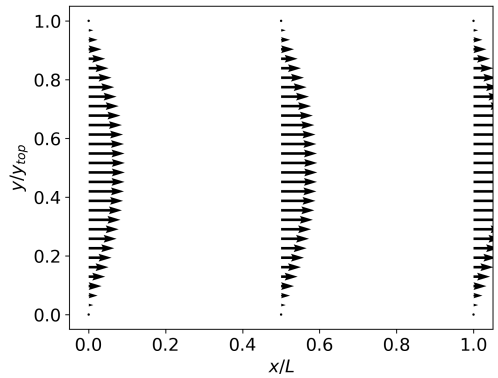

(c) Streamlines using Zou-He

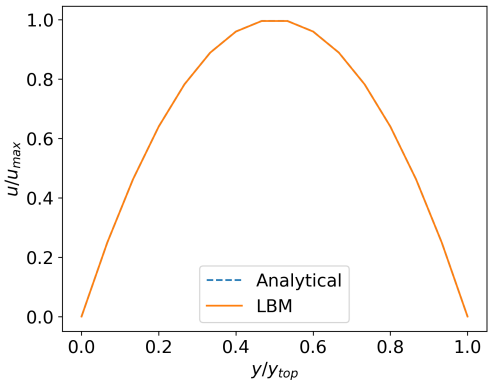

(d) Velocity profile using Zou-He

Fig. A.8.: Poiseuille flow simulations with no-slip condition on the walls ($u = 0$). Top row presents the results using bounce-back (BB) as boundary condition, in a) we observe the streamlines and in b) the velocity profile. Bottom row the results of the simulations using Zou-He as boundary condition, in c) the streamlines and in d) the velocity profile. The velocity profiles were obtained at $x = L/2$.

A.5 Perspectives and preliminary work

Currently 2D tests in more complex, realistic, geometries are ongoing. Moreover, we plan to include support for 3D simulations and multi-phase flows. Concerning the research interests linked to this thesis, thanks to our collaborators from the Pasqual Maragall foundation we have access to high-resolution anatomical MRI, and to images of CSF and blood flow. The CSF flow images are acquired at the level of the foramen Magnum, and the blood flow images at the carotid level. The goal is to assess differences in CSF-blood flow coupling in individuals with different levels of $A\beta$ aggregation. Therefore, we will extract the flow pattern at the carotid level and use it as input BC for the CSF flow at the lateral ventricles, similar to previous mechanistic studies [Sweetman, 2011; Howden, 2008; Linninger, 2007]. Then we will analyse the pressure transmission between CSF and blood flow using our LBM solver. We hypothesise that subjects with higher amyloid

aggregation may have an impaired CSF flow, which can be related to a hampered transmission of the pressure wave due to arterial stiffening. In Figure A.9 we present an example of the available flow images and the obtained velocity profiles. In Figure A.9c it is visible how at the level of the foramen Magnum the CSF flows towards the spinal canal during carotid systole and the motion is reversed during diastole. Moreover, we see the lag between the peak blood flow and the peak CSF flow. CFD simulations will allow us to explore the velocity field and pressure distribution throughout the whole CSF pathway.

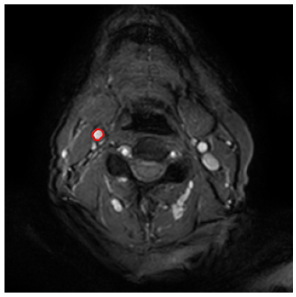

(a) Blood flow image

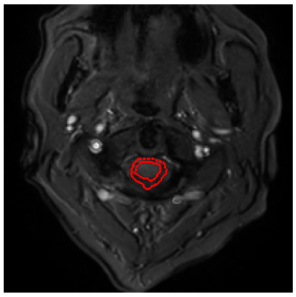

(b) CSF flow image

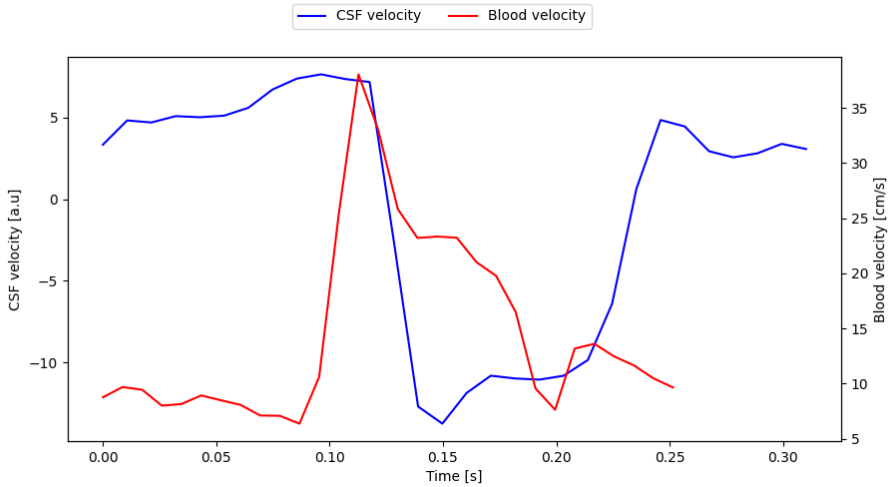

(c) Velocity

Fig. A.9.: a) Blood flow image at the carotid level, b) CSF flow image at the foramen Magnum level. The red area in both images indicate the regions of interest (ROI). c) Velocity profile of the blood flow at the carotid (red) and of the CSF (blue). The units of the CSF velocity are not properly scaled yet.

A preliminary work together with UPF students was done in the OASIS database [LaMontagne, 2019]. We selected a subject for which T1 and T2 MRI were available and used them to obtain an initial segmentation of the CSF pathways by means of FreeSurfer [Dale, 1999]. Next, the segmentation was corrected by means of topological operations performed using the MATLAB morphological toolbox (MATLAB 2020a). Manual corrections using ITK-Snap [Yushkevich, 2006] were applied to obtain the final segmentation. Next, the final segmentation was used to obtain a surface mesh using iso2mesh [Fang,

2009] in MATLAB. The surface mesh was used as input to generate a volumetric mesh in Gmsh [Geuzaine, 2009], where mesh smoothing was also carried out. The final geometry was composed of the brain subarachnoid space and the ventricles system, as can be seen in Figure A.10.

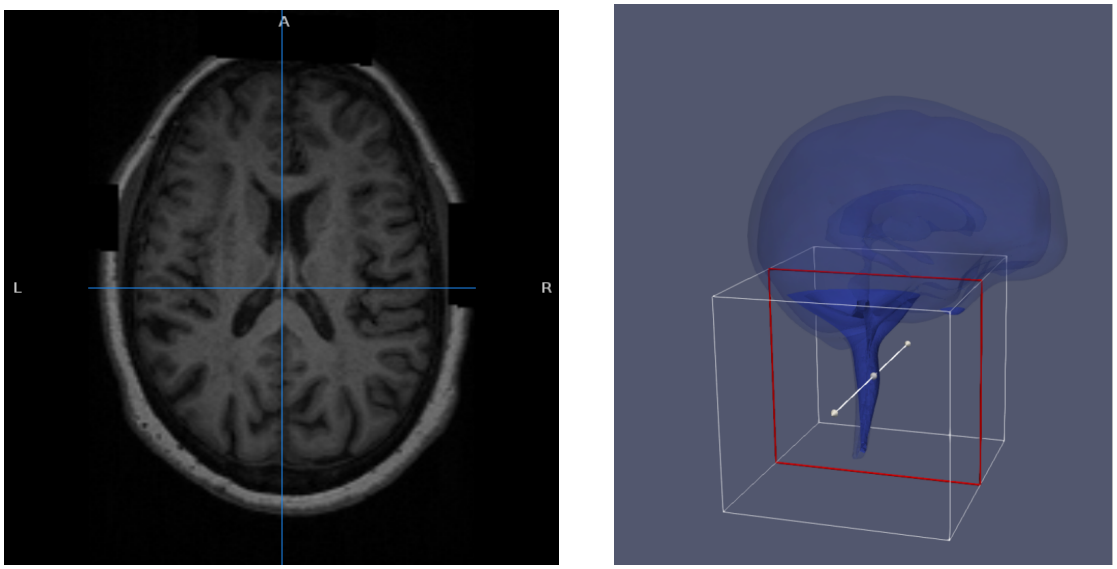

(a) T1 MRI **(b)** CSF segmentation

Fig. A.10.: a) T1 MRI used as input b) Final CSF segmentation

To carry out the CFD simulations a commercial FEM solver (ANSYS R 19.5) was used. A digitised waveform from a previous CSF modelling study was used as transient input [Linninger, 2007]. CSF viscosity was set to $0.003\ Kg/(m \cdot s)$ and density to $1007\ Kg/m^3$ [Sweetman, 2011]. As BC we specified two inlets at the choroid plexus in the two lateral ventricles, and two outlets: one in the upper subarachnoid space, emulating the sagittal venous sinus, and another in the spinal canal, the BC locations are shown in Figure A.11a. Figure A.11b illustrates the pressure values obtained at the 4th ventricle (red) and at the choroid plexus (in blue). The reported values are in the same range as the values reported in previous studies [Linninger, 2005].

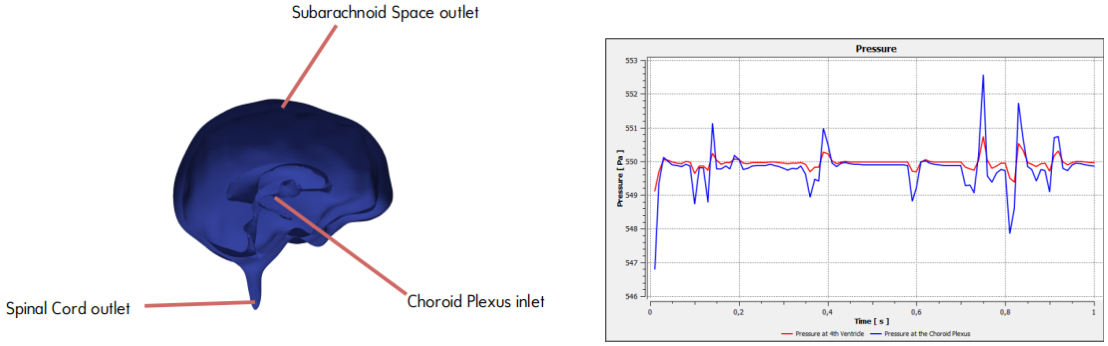

(a) Location of boundary conditions **(b)** Transient pressure profiles

Fig. A.11.: a) Location of the boundary conditions b) Transient pressure profiles

Overall, this preliminary work highlights the challenges associated to the process required to go from an anatomical MRI to a mesh suitable to obtain CFD simulations using classic FEM or FD numerical methods. Thus, we expect that our LBM method can help to reduce the associated burden to obtain CFD simulations.

Bibliography

[Abbott, 2018] N. Joan Abbott, Michelle E. Pizzo, Jane E. Preston, Damir Janigro, and Robert G. Thorne. “The role of brain barriers in fluid movement in the CNS: is there a ‘glymphatic’ system?” In: *Acta Neuropathologica* 135.3 (2018), pp. 387–407 (cit. on p. 29).

[Abi Nader, 2020] Clément Abi Nader, Nicholas Ayache, Philippe Robert, and Marco Lorenzi. “Monotonic Gaussian Process for spatio-temporal disease progression modeling in brain imaging data”. In: *NeuroImage* 205 (2020), p. 116266 (cit. on p. 72).

[Acosta, 2018] Sebastián Acosta, Daniel J. Penny, Ken M. Brady, and Craig G. Rusin. “An effective model of cerebrovascular pressure reactivity and blood flow autoregulation”. In: *Microvascular Research* 115.November 2016 (2018), pp. 34–43 (cit. on pp. 7, 62).

[Adams, 2020] Ayodeji L Adams, Max A Viergever, Peter R Luijten, and Jaco J M Zwanenburg. “Validating faster DENSE measurements of cardiac-induced brain tissue expansion as a potential tool for investigating cerebral microvascular pulsations”. In: *NeuroImage* (2020), p. 116466 (cit. on p. 96).

[Agarwal, 2021] Nivedita Agarwal and Roxana Octavia Carare. “Cerebral Vessels: An Overview of Anatomy, Physiology, and Role in the Drainage of Fluids and Solutes”. In: *Frontiers in Neurology* 11.January (2021), pp. 1–8 (cit. on pp. 5, 26, 29, 91, 96).

[Aghilinejad, 2020] Arian Aghilinejad, Faisal Amlani, Kevin S King, and Niema M Pahlevan. “Dynamic Effects of Aortic Arch Stiffening on Pulsatile Energy Transmission to Cerebral Vasculature as A Determinant of Brain-Heart Coupling”. In: *Scientific Reports* 10.1 (2020), p. 8784 (cit. on pp. 7, 36, 59, 73).

[Akasheva, 2015] Dariga U. Akasheva et al. “Age-related left ventricular changes and their association with leukocyte telomere length in healthy people”. In: *PLoS ONE* 10.8 (2015), pp. 1–10 (cit. on pp. 54, 69).

[Alfaro-Almagro, 2018] F. Alfaro-Almagro et al. “Image processing and Quality Control for the first 10,000 brain imaging datasets from UK Biobank.” In: *NeuroImage* 166 (2018), pp. 400–424 (cit. on pp. 47, 48, 74).

[Alonso, 2016] Alvaro Alonso and Antonio P Arenas de Larriva. “Atrial Fibrillation, Cognitive Decline and Dementia”. In: *European Cardiology Review* 11.1 (2016), p. 49 (cit. on p. 34).

[Alosco, 2013] Michael L. Alosco, Adam M. Brickman, Mary Beth Spitznagel, et al. “Cerebral Perfusion is Associated With White Matter Hyperintensities in Older Adults With Heart Failure”. In: *Congestive Heart Failure* 19.4 (2013), E29–E34 (cit. on pp. 34, 58).

[Azarpazhooh, 2018] Mahmoud Reza Azarpazhooh, Abolfazl Avan, Lauren E. Cipriano, et al. “Concomitant vascular and neurodegenerative pathologies double the risk of dementia.” In: *Alzheimer’s and Dementia* 14(2) (2018), pp. 148–156 (cit. on pp. 34, 71).

[Bacyinski, 2017] Andrew Bacyinski, Maosheng Xu, Wei Wang, and Jiani Hu. “The paravascular pathway for brain waste clearance: Current understanding, significance and controversy”. In: *Frontiers in Neuroanatomy* 11.November (2017), pp. 1–8 (cit. on pp. 29, 30).

[Bahrani, 2017] Ahmed A. Bahrani, David K. Powell, Guoquiang Yu, et al. “White Matter Hyperintensity Associations with Cerebral Blood Flow in Elderly Subjects Stratified by Cerebrovascular Risk”. In: *Journal of Stroke and Cerebrovascular Diseases* 26.4 (2017), pp. 779–786 (cit. on pp. 6, 35).

[Bakker, 2016] Erik N.T.P. Bakker, Brian J. Bacskai, Michal Arbel-Ornath, et al. “Lymphatic Clearance of the Brain: Perivascular, Paravascular and Significance for Neurodegenerative Diseases”. In: *Cellular and Molecular Neurobiology* 36.2 (2016), pp. 181–194 (cit. on p. 25).

[Baldo, 2015] Marcelo Perim Baldo, Sérgio Lamêgo Rodrigues, and José Geraldo Mill. “High salt intake as a multifaceted cardiovascular disease: new support from cellular and molecular evidence”. In: *Heart Failure Reviews* 20.4 (2015), pp. 461–474 (cit. on p. 90).

[Banus, 2019] Jaume Banus, Marco Lorenzi, Oscar Camara, and Maxime Sermesant. “Large Scale Cardiovascular Model Personalisation for Mechanistic Analysis of Heart & Brain Interactions”. In: *Functional Imaging and Modelling of the Heart* (2019) (cit. on pp. 33, 35, 65, 88).

[Banus, 2020] Jaume Banus, Maxime Sermesant, Oscar Camara, and Marco Lorenzi. “Joint Data Imputation and Mechanistic Modelling for Simulating Heart-Brain Interactions in Incomplete Datasets”. In: *Medical Image Computing and Computer Assisted Intervention – MICCAI 2020*. Ed. by Martel A.L. et al. (eds). Springer, Cham, 2020, pp. 478–486 (cit. on pp. 61, 73, 75, 77, 88).

[Benjamin, 2018] Emelia J. Benjamin et al. “Heart Disease and Stroke Statistics—2018 Update: A Report From the American Heart Association.” In: *Circulation* 137(12) (2018) (cit. on p. 34).

[Bering, 1955] Edgar A. Bering. “Choroid plexus and arterial pulsation of cerebrospinal fluid”. In: *A.M.A. Archives of Neurology & Psychiatry* 73.2 (1955), p. 165 (cit. on pp. 29, 96).

[Bhatnagar, 1954] P. L. Bhatnagar, E. P. Gross, and M. Krook. “A Model for Collision Processes in Gases. I. Small Amplitude Processes in Charged and Neutral One-Component Systems”. In: *Physical Review* 94.3 (1954), pp. 511–525 (cit. on p. 103).

[Blanco, 2015] P. Blanco et al. “An anatomically detailed arterial network model for one-dimensional computational hemodynamics.” In: *IEEE Transactions on Biomedical Engineering* 62(2) (2015), pp. 736–753 (cit. on pp. 7, 62).

[Bothwell, 2019] Steven William Bothwell, Damir Janigro, and Adjanie Patabendige. “Cerebrospinal fluid dynamics and intracranial pressure elevation in neurological diseases”. In: *Fluids and Barriers of the CNS* 16.1 (2019), pp. 1–18 (cit. on pp. 29, 96).

[Broce, 2019] Iris J. Broce, Chin Hong Tan, Chun Chieh Fan, et al. “Dissecting the genetic relationship between cardiovascular risk factors and Alzheimer’s disease”. In: *Acta Neuropathologica* 137.2 (2019), pp. 209–226 (cit. on p. 4).

[Caruel, 2014] M. Caruel, R. Chabiniok, P. Moireau, Y. Lecarpentier, and D. Chapelle. “Dimensional reductions of a cardiac model for effective validation and calibration”. In: *Biomechanics and Modeling in Mechanobiology* 13 (2014), pp. 897–914 (cit. on pp. 37, 39, 41, 42, 65, 74).

[Chapelle, 2012] D. Chapelle, P. Le Tallec, P. Moireau, and M. Sorine. “Energy-preserving muscle tissue model: formulation and compatible discretizations.” In: *International Journal for Multiscale Computational Engineering* 10(2) (2012), pp. 189–211 (cit. on pp. 37, 40).

[Chen, 2018] Lin Y. Chen, Faye L. Norby, Rebecca F. Gottesman, et al. “Association of atrial fibrillation with cognitive decline and dementia over 20 years: The ARIC-NCS (Atherosclerosis Risk in Communities Neurocognitive Study)”. In: *Journal of the American Heart Association* 7.6 (2018), pp. 1–13 (cit. on p. 34).

[Cox, 2019] Simon R Cox et al. “Associations between vascular risk factors and brain MRI indices in UK Biobank”. In: *European Heart Journal* 44 (2019), pp. 1–11 (cit. on pp. 6, 36, 62).

[Dabrowska, 2020] Edyta Dabrowska, Joanna M. Harazny, Eliza Miszkowska-Nagórna, et al. “Lumen narrowing and increased wall to lumen ratio of retinal microcirculation are valuable biomarkers of hypertension-mediated cardiac damage”. In: *Blood Pressure* 29.2 (2020), pp. 70–79 (cit. on p. 58).

[Dagres, 2018] Nikolaos Dagres. “Expert consensus on arrhythmias and cognitive function: What is the best practice?” In: *Europace* 20.9 (2018), pp. 1399–1400 (cit. on pp. 58, 85).

[Dale, 1999] Anders M. Dale, Bruce Fischl, and Martin I. Sereno. “Cortical Surface-Based Analysis”. In: *NeuroImage* 9.2 (1999), pp. 179–194 (cit. on p. 114).

[Debette, 2010] S. Debette and H. S. Markus. “The clinical importance of white matter hyperintensities on brain magnetic resonance imaging: systematic review and meta-analysis”. In: *Bmj* 341.jul26 1 (2010), pp. c3666–c3666 (cit. on pp. 5, 31, 34, 35).

[Delingette, 2012] Herve Delingette, Florence Billet, Ken C.L. Wong, et al. “Personalization of cardiac motion and contractility from images using variational data assimilation”. In: *IEEE Transactions on Biomedical Engineering* 59.1 (2012), pp. 20–24 (cit. on pp. 7, 36).

[Dichgans, 2017] Martin Dichgans and Didier Leys. “Vascular Cognitive Impairment”. In: *Circulation Research* 120.3 (2017), pp. 573–591 (cit. on pp. 3, 4, 31).

[Diener, 2019] Hans-christoph Diener, Robert G Hart, Peter J Koudstaal, Deirdre A Lane, and Gregory Y.H. Lip. “Atrial Fibrillation and Cognitive Function”. In: *Journal of the American College of Cardiology* 73.5 (2019), pp. 612–619 (cit. on pp. 4, 6, 31, 71, 85).

[Ding, 2020] Jie Ding. “Antihypertensive medications and risk for incident dementia and Alzheimer’s disease: a meta-analysis of individual participant data from prospective cohort studies”. In: *The Lancet Neurology* 19.1 (2020), pp. 61–70 (cit. on p. 85).

[Doehner, 2018] Wolfram Doehner et al. “Heart and brain interaction in patients with heart failure: overview and proposal for a taxonomy. A position paper from the Study Group on Heart and Brain Interaction of the Heart Failure Association”. In: *European Journal of Heart Failure* 20.2 (2018), pp. 199–215 (cit. on pp. 4, 6, 30, 31, 34, 61, 71).

[Downey, 2001] James M. Downey and Gerd Heusch. “Sequence of Cardiac Activation and Ventricular Mechanics”. In: *Heart Physiology and Pathophysiology*. Elsevier, 2001, pp. 3–18 (cit. on p. 54).

[Dyrna, 2013] Felix Dyrna, Sophie Hanske, Martin Krueger, and Ingo Bechmann. “The blood-brain barrier”. In: *Journal of Neuroimmune Pharmacology* 8.4 (2013), pp. 763–773 (cit. on p. 25).

[Enzmann, 1992] D R Enzmann and N J Pelc. “Brain motion: measurement with phase-contrast MR imaging.” In: *Radiology* 185.3 (1992), pp. 653–660 (cit. on p. 96).

[Epstein, 2013] Noam U Epstein, Kathleen A Lane, Martin R Farlow, et al. “Cognitive dysfunction and greater visit-to-visit systolic blood pressure variability”. In: *Journal of the American Geriatrics Society* 61.12 (2013), pp. 2168–2173 (cit. on pp. 62, 72).

[Fang, 2009] Q Fang and D a Boas. “Tetrahedral mesh generation from volumetric binary and gray scale images”. In: *International Symposium on Biomedical Imaging* Isbi (2009), pp. 1563–1569 (cit. on p. 114).

[Faraco, 2019] Giuseppe Faraco, Karin Hochrainer, Steven G. Segarra, et al. “Dietary salt promotes cognitive impairment through tau phosphorylation”. In: *Nature* 574.7780 (2019), pp. 686–690 (cit. on p. 89).

[Feiger, 2019] Bradley Feiger, Madhurima Vardhan, John Gounley, et al. “Suitability of lattice Boltzmann inlet and outlet boundary conditions for simulating flow in image-derived vasculature”. In: *International Journal for Numerical Methods in Biomedical Engineering* 35.6 (2019), pp. 1–15 (cit. on pp. 96, 100, 105).

[Feinleib, 1975] Manning Feinleib, William B. Kannel, Robert J. Garrison, Patricia M. McNamara, and William P. Castelli. “The framingham offspring study. Design and preliminary data”. In: *Preventive Medicine* 4.4 (1975), pp. 518–525 (cit. on p. 4).

[Friedman, 2014] Joseph I. Friedman, Cheuk Y. Tang, Hans J. De Haas, et al. “Brain imaging changes associated with risk factors for cardiovascular and cerebrovascular disease in asymptomatic patients”. In: *JACC: Cardiovascular Imaging* 7.10 (2014), pp. 1039–1053 (cit. on pp. 4, 34, 35).

[Geuzaine, 2009] Christophe Geuzaine and Jean-François Remacle. “Gmsh: A 3-D finite element mesh generator with built-in pre- and post-processing facilities”. In: *International Journal for Numerical Methods in Engineering* 79.11 (2009), pp. 1309–1331 (cit. on p. 115).

[Goriely, 2015] Alain Goriely, Marc G.D. Geers, Gerhard A. Holzapfel, et al. “Mechanics of the brain: perspectives, challenges, and opportunities”. In: *Biomechanics and Modeling in Mechanobiology* 14.5 (2015), pp. 931–965 (cit. on p. 95).

[Guo, 2002] Zhaoli Guo, Chuguang Zheng, and Baochang Shi. “Discrete lattice effects on the forcing term in the lattice Boltzmann method”. In: *Physical Review E - Statistical Physics, Plasmas, Fluids, and Related Interdisciplinary Topics* 65.4 (2002), p. 6 (cit. on p. 105).

[Gupta, 2018] Nidhi Gupta, Alexis N. Simpkins, Emi Hitomi, Christian Dias, and Richard Leigh. “White Matter Hyperintensity-Associated Blood-Brain Barrier Disruption and Vascular Risk Factors”. In: *Journal of Stroke and Cerebrovascular Diseases* 27.2 (2018), pp. 466–471 (cit. on pp. 5, 31).

[Hansen, 2016] N. Hansen. “The CMA Evolution Strategy: A Comparing Review.” In: *Towards a New Evolutionary Computation* 102 (2016), pp. 75–102 (cit. on p. 44).

[Hansson, 2018] Oskar Hansson, John Seibyl, Erik Stomrud, et al. “CSF biomarkers of Alzheimer’s disease concord with amyloid-β PET and predict clinical progression: A study of fully automated immunoassays in BioFINDER and ADNI cohorts”. In: *Alzheimer’s and Dementia* 14.11 (2018), pp. 1470–1481 (cit. on p. 4).

[Herring, 2018] Neil Herring and David J. Paterson. *Levick’s Introduction Cardiovascular Physiology*. 6th. CRC Press, 2018, p. 448 (cit. on pp. 13, 19, 21–23, 26).

[Hofman, 2015] Albert Hofman et al. “The Rotterdam Study: 2016 objectives and design update”. In: *European Journal of Epidemiology* 30.8 (2015), pp. 661–708 (cit. on p. 4).

[Hooghiemstra, 2017] Astrid M. Hooghiemstra et al. “The Missing Link in the Pathophysiology of Vascular Cognitive Impairment: Design of the Heart-Brain Study”. In: *Cerebrovascular Diseases Extra* 7.3 (2017), pp. 140–152 (cit. on pp. 6, 34).

[Hooghiemstra, 2019] Astrid M Hooghiemstra, Anna E Leeuwis, Anne Suzannne Bertens, Geert Jan Biessels, and Michiel L Bots. “Frequent Cognitive Impairment in Patients With Disorders Along the Heart-Brain Axis”. In: (2019), pp. 1–7 (cit. on p. 6).

[Howden, 2008] L. Howden, D. Giddings, H. Power, et al. “Three-dimensional cerebrospinal fluid flow within the human ventricular system”. In: *Computer Methods in Biomechanics and Biomedical Engineering* 11.2 (2008), pp. 123–133 (cit. on pp. 96, 113).

[Huxley, 1957] A. F Huxley. “Muscle structure and theories of contraction”. In: *Progress in biophysics and biological chemistry* 7.3 (1957), pp. 255–318 (cit. on p. 38).

[Iadecola, 2013] C Iadecola. “The pathology of vascular dementia”. In: *Neuron* 80.4 (2013), pp. 844–866 (cit. on pp. 5, 24, 31).

[Iadecola, 2017] Costantino Iadecola. “The Neurovascular Unit Coming of Age: A Journey through Neurovascular Coupling in Health and Disease”. In: *Neuron* 96.1 (Sept. 2017), pp. 17–42 (cit. on p. 24).

[Iliff, 2013] Jeffrey J. Iliff, Minghuan Wang, Douglas M. Zeppenfeld, et al. “Cerebral arterial pulsation drives paravascular CSF-Interstitial fluid exchange in the murine brain”. In: *Journal of Neuroscience* 33.46 (2013), pp. 18190–18199 (cit. on pp. 25, 29, 91, 95).

[Iturria-Medina, 2016] Y. Iturria-Medina et al. “Early role of vascular dysregulation on late-onset Alzheimer’s disease based on multifactorial data-driven analysis”. In: *Nature Communications* 7.May (2016) (cit. on pp. 4, 72).

[Ivanov, 2019] O. Ivanov et al. “Variational autoencoder with arbitrary conditioning”. In: *7th, ICLR 2019* (2019), pp. 1–25. eprint: 1806.02382 (cit. on p. 64).

[Jack, 2013] Clifford R Jack et al. “Tracking pathophysiological processes in Alzheimer’s disease: an updated hypothetical model of dynamic biomarkers”. In: *The Lancet Neurology* 12.2 (2013), pp. 207–216 (cit. on pp. 3, 72).

[Jack, 2018] Clifford R. Jack et al. “NIA-AA Research Framework: Toward a biological definition of Alzheimer’s disease”. In: *Alzheimer’s & Dementia* 14.4 (2018), pp. 535–562 (cit. on p. 4).

[Jan, 2020] Jacob Jan, Geert Jan, and Jaco J M Zwanenburg. “NeuroImage Cardiac and respiration-induced brain deformations in humans quanti fi ed with high- fi eld MRI”. In: 210.August 2019 (2020) (cit. on p. 96).

[Jani, 2006] B. Jani and C. Rajkumar. “Ageing and vascular ageing”. In: *Postgraduate Medical Journal* 82.968 (2006), pp. 357–362 (cit. on p. 54).

[Jefferson, 2009] Angela L Jefferson, David F Tate, Athena Poppas, et al. “Lower Cardiac Output Is Associated with Greater White Matter Hyperintensities in Older Adults with Cardiovascular Disease”. In: *J Am Geriatr Soc* 55 (2009), pp. 1044–1048 (cit. on pp. 6, 34, 35, 58, 70, 72, 85).

[Jegier, 1963] W. Jegier, P. Sekelj, P. A. Auld, R. Simpson, and M. McGregor. “the Relation Between Cardiac Output and Body Size.” In: *British heart journal* 25.604 (1963), pp. 425–430 (cit. on pp. 54, 69).

[Kapasi, 2017] Alifiya Kapasi, Charles DeCarli, and Julie A. Schneider. “Impact of multiple pathologies on the threshold for clinically overt dementia”. In: *Acta Neuropathologica* 134.2 (2017), pp. 171–186 (cit. on pp. 4, 71).

[Khalil, 2006] Ahmad S. Khalil, Brett E. Bouma, and Mohammad R. Kaazempur Mofrad. “A combined FEM/genetic algorithm for vascular soft tissue elasticity estimation”. In: *Cardiovascular Engineering* 6.3 (2006), pp. 93–102 (cit. on pp. 7, 36).

[Kohn, 2015] J. Kohn et al. “Age-related vascular stiffening: Causes and consequences”. In: *Frontiers in Genetics* 6.MAR (2015), pp. 1–17 (cit. on p. 69).

[Koval, 2017] I Koval, J.-B. Schiratti, A Routier, et al. “Statistical Learning of Spatiotemporal Patterns from Longitudinal Manifold-Valued Networks”. In: *Medical Image Computing and Computer Assisted Intervention - MICCAI* (2017), pp. 451–459. arXiv: `arXiv:1709.08491v1` (cit. on p. 72).

[Krüger, 2017] Timm Krüger, Halim Kusumaatmaja, Alexandr Kuzmin, et al. *The Lattice Boltzmann Method*. Graduate Texts in Physics. Cham: Springer International Publishing, 2017 (cit. on p. 95).

[LaMontagne, 2019] Pamela J LaMontagne, Tammie L S Benzinger, John C Morris, et al. “OASIS-3: Longitudinal Neuroimaging, Clinical, and Cognitive Dataset for Normal Aging and Alzheimer Disease”. In: *medRxiv* (2019), p. 2019.12.13.19014902 (cit. on p. 114).

[Lane, 2019] Christopher A. Lane, Josephine Barnes, Jennifer M. Nicholas, et al. “Associations between blood pressure across adulthood and late-life brain structure and pathology in the neuroscience substudy of the 1946 British birth cohort (Insight 46): an epidemiological study”. In: *The Lancet Neurology* 18.10 (2019), pp. 942–952 (cit. on pp. 4, 72, 85).

[Lau, 2012] Y. F. Lau, K. H. Yiu, C. W. Siu, and H. F. Tse. “Hypertension and atrial fibrillation: Epidemiology, pathophysiology and therapeutic implications”. In: *Journal of Human Hypertension* 26.10 (2012), pp. 563–569 (cit. on p. 59).

[Laurent, 2015] Stephane Laurent and Pierre Boutouyrie. “The Structural Factor of Hypertension: Large and Small Artery Alterations”. In: *Circulation Research* 116.6 (2015), pp. 1007–1021 (cit. on p. 58).

[Leeuwis, 2020] Anna E Leeuwis, Eline A Oudeman, L Jaap Kappelle, et al. “Cerebral blood flow and cognitive functioning in patients with disorders along the heart – brain axis Cerebral blood flow and the heart – brain axis”. In: March (2020), pp. 1–11 (cit. on p. 6).

[Linninger, 2005] Andreas A. Linninger, Cristian Tsakiris, David C. Zhu, et al. “Pulsatile cerebrospinal fluid dynamics in the human brain”. In: *IEEE Transactions on Biomedical Engineering* 52.4 (2005), pp. 557–565 (cit. on pp. 96, 97, 115).

[Linninger, 2007] Andreas A Linninger, Michalis Xenos, David C Zhu, et al. “Cerebrospinal Fluid Flow in the Normal and Hydrocephalic Human Brain”. In: *IEEE Transactions on Biomedical Engineering* 54.2 (2007), pp. 291–302 (cit. on pp. 96, 113, 115).

[Linninger, 2016] Andreas A. Linninger, Kevin Tangen, Chih Yang Hsu, and David Frim. “Cerebrospinal Fluid Mechanics and Its Coupling to Cerebrovascular Dynamics”. In: *Annual Review of Fluid Mechanics* 48 (2016), pp. 219–257 (cit. on pp. 90, 96).

[Lorenzi, 2018] Marco Lorenzi and Maurizio Filippone. “Constraining the dynamics of deep probabilistic models”. In: *35th International Conference on Machine Learning, ICML 2018* 7 (2018), pp. 5089–5101 (cit. on p. 73).

[Lorenzi, 2019] Marco Lorenzi, Maurizio Filippone, Giovanni B. Frisoni, Daniel C. Alexander, and Sebastien Ourselin. “Probabilistic disease progression modeling to characterize diagnostic uncertainty: Application to staging and prediction in Alzheimer’s disease”. In: *NeuroImage* 190 (2019), pp. 56–68 (cit. on pp. 72, 76).

[Loth, 2001] F. Loth, M. A. Yardimci, and N. Alperin. “Hydrodynamic modeling of cerebrospinal fluid motion within the spinal cavity”. In: *Journal of Biomechanical Engineering* 123.1 (2001), pp. 71–79 (cit. on pp. 29, 96).

[Lourida, 2019] Ilianna Lourida, Eilis Hannon, Thomas J Littlejohns, et al. “Association of Lifestyle and Genetic Risk With Incidence of Dementia”. In: (2019), pp. 1–8 (cit. on p. 6).

[Marchesseau, 2013] Stéphanie Marchesseau, Hervé Delingette, Maxime Sermesant, and Nicholas Ayache. “Fast parameter calibration of a cardiac electromechanical model from medical images based on the unscented transform”. In: *Biomechanics and Modeling in Mechanobiology* 12.4 (2013), pp. 815–831 (cit. on p. 37).

[Marinescu, 2019] V Marinescu, Arman Eshaghi, Marco Lorenzi, et al. “DIVE : A spatiotemporal progression model of brain pathology in neurodegenerative disorders”. In: *NeuroImage* 192.June 2018 (2019), pp. 166–177 (cit. on p. 72).

[Mastorakos, 2019] Panagiotis Mastorakos and Dorian McGavern. “The anatomy and immunology of vasculature in the central nervous system”. In: *Science Immunology* 4.37 (2019), pp. 1–15 (cit. on p. 25).

[Matthews, 2016] F. E. Matthews et al. “A two decade dementia incidence comparison from the Cognitive Function and Ageing Studies i and II”. In: *Nature Communications* 7 (2016) (cit. on p. 4).

[Mattsson, 2014] Niklas Mattsson, Philip S. Insel, Susan Landau, et al. “Diagnostic accuracy of CSF Ab42 and florbetapir PET for Alzheimer’s disease”. In: *Annals of Clinical and Translational Neurology* 1.8 (2014), pp. 534–543 (cit. on p. 4).

[Mazzeo, 2008] M. D. Mazzeo and P. V. Coveney. “HemeLB: A high performance parallel lattice-Boltzmann code for large scale fluid flow in complex geometries”. In: *Computer Physics Communications* 178.12 (2008), pp. 894–914 (cit. on p. 100).

[McNamara, 1988] Guy R. McNamara and Gianluigi Zanetti. “Use of the Boltzmann Equation to Simulate Lattice-Gas Automata”. In: *Physical Review Letters* 61.20 (1988), pp. 2332–2335 (cit. on p. 101).

[Melis, 2017] A. Melis et al. “Bayesian sensitivity analysis of a 1D vascular model with Gaussian process emulators”. In: *INT J NUMER METH BIO.* 33.12 (2017), pp. 1–11 (cit. on p. 64).

[Mestre, 2018] Humberto Mestre, Jeffrey Tithof, Ting Du, et al. “Flow of cerebrospinal fluid is driven by arterial pulsations and is reduced in hypertension”. In: *Nature Communications* 9.1 (2018) (cit. on p. 29).

[Mestre, 2020] Humberto Mestre, Yuki Mori, and Maiken Nedergaard. “The Brain’s Glymphatic System: Current Controversies”. In: *Trends in Neurosciences* 43.7 (2020), pp. 458–466 (cit. on pp. 5, 29, 91, 95, 96).

[Modir, 2012] R. Modir, H. Gardener, and C. B. Wright. “Stroke Blood Pressure and White Matter Hyperintensity Volume — A Review of the Relationship and Implications for Stroke Prediction and Prevention.” In: *US Neurology* 8(1) (2012), pp. 33–36 (cit. on pp. 34, 54).

[Molléro, 2017] R. Molléro, X. Pennec, H. Delingette, et al. “Multifidelity-CMA: a multifidelity approach for efficient personalisation of 3D cardiac electromechanical models.” In: *Biomechanics & Modeling in Mechanobiology* 17(1) (2017), pp. 285–300 (cit. on pp. 7, 36, 62, 73).

[Molléro, 2018] R. Molléro, X. Pennec, H. Delingette, N. Ayache, and M. Sermesant. “Population-Based Priors in Cardiac Model Personalisation for Consistent Parameter Estimation in Heterogeneous Databases.” In: *International Journal for Numerical Methods in Biomedical Engineering.* (2018) (cit. on pp. 8, 35, 36, 45, 49, 60, 65).

[Moroni, 2018] Francesco Moroni, Enrico Ammirati, Maria A. Rocca, et al. “Cardiovascular disease and brain health: Focus on white matter hyperintensities.” In: *IJC Heart and Vasculature* 19 (2018), pp. 63–69 (cit. on pp. 5, 31, 34, 54).

[Mosteller, 1987] RD Mosteller. “Simplified calculation of body-surface area”. In: *The new england journal of medicine* 17.317 (1987), p. 1098 (cit. on pp. 49, 74).

[Mueller, 2005] Susanne G. Mueller, Michael W. Weiner, Leon J. Thal, et al. “The Alzheimer’s Disease Neuroimaging Initiative”. In: *Neuroimaging Clinics of North America* 15.4 (2005), pp. 869–877 (cit. on pp. 3, 72).

[Muiesan, 2014] Maria Lorenza Muiesan, Massimo Salvetti, Anna Paini, et al. “Central blood pressure assessment using 24-hour brachial pulse wave analysis”. In: *Journal of Vascular Diagnostics* (2014), p. 141 (cit. on p. 49).

[Müller, 2014] L. O. Müller and E. F. Toro. “Enhanced global mathematical model for studying cerebral venous blood flow.” In: *Journal of Biomechanics* 47(13) (2014), pp. 3361–3372 (cit. on pp. 59, 70).

[Neumann, 2016] Dominik Neumann, Tommaso Mansi, Lucian Itu, et al. “A self-taught artificial agent for multi-physics computational model personalization”. In: *Medical Image Analysis* 34 (2016), pp. 52–64 (cit. on pp. 7, 36).

[Nichols, 2019] Emma Nichols et al. “Global, regional, and national burden of Alzheimer’s disease and other dementias, 1990–2016: a systematic analysis for the Global Burden of Disease Study 2016”. In: *The Lancet Neurology* 18.1 (2019), pp. 88–106 (cit. on p. 3).

[Ois, 2008] A. Ois, M. Gomis, E. Cuadrado-Godia, et al. “Heart failure in acute ischemic stroke”. In: *Journal of Neurology* 255(3) (2008), pp. 385–389 (cit. on p. 34).

[Olsson, 2016] Bob Olsson et al. “CSF and blood biomarkers for the diagnosis of Alzheimer’s disease: a systematic review and meta-analysis”. In: *The Lancet Neurology* 15.7 (2016), pp. 673–684 (cit. on p. 4).

[Orešković, 2010] D. Orešković and M. Klarica. “The formation of cerebrospinal fluid: Nearly a hundred years of interpretations and misinterpretations”. In: *Brain Research Reviews* 64.2 (2010), pp. 241–262 (cit. on p. 95).

[ORourke, 2007] Michael F. O’Rourke and Junichiro Hashimoto. “Mechanical Factors in Arterial Aging. A Clinical Perspective”. In: *Journal of the American College of Cardiology* 50.1 (2007), pp. 1–13 (cit. on pp. 5, 22, 31).

[Østergaard, 2013] Leif Østergaard, Rasmus Aamand, Eugenio Gutiérrez-Jiménez, et al. “The capillary dysfunction hypothesis of Alzheimer’s disease”. In: *Neurobiology of Aging* 34.4 (2013), pp. 1018–1031 (cit. on pp. 5, 31).

[Pant, 2014] S. Pant, B. Fabrèges, J-F. Gerbeau, and I. E. Vignon-Clementel. “A methodological paradigm for patient-specific multi-scale CFD simulations: from clinical measurements to parameter estimates for individual analysis”. In: *International Journal for Numerical Methods in Biomedical Engineering* 30.12 (2014), pp. 1614–1648 (cit. on pp. 8, 36).

[Pant, 2017] Sanjay Pant, Chiara Corsini, Catriona Baker, et al. “Inverse problems in reduced order models of cardiovascular haemodynamics: Aspects of data assimilation and heart rate variability”. In: *Journal of the Royal Society Interface* 14.126 (2017) (cit. on pp. 7, 36, 59).

[Pappano, 2013] Achilles Pappano and Wier Withrow. *Cardiovascular Physiology*. 10th. Elsevier, 2013, p. 304 (cit. on p. 13).

[Paszke, 2019] Adam Paszke, Sam Gross, Francisco Massa, et al. "PyTorch: An Imperative Style, High-Performance Deep Learning Library". In: *Advances in Neural Information Processing Systems 32*. Curran Associates, Inc., 2019, pp. 8024–8035 (cit. on p. 105).

[Patel, 2017] Sheila K. Patel, Carolina Restrepo, Emilio Werden, et al. "Does left ventricular hypertrophy affect cognition and brain structural integrity in type 2 diabetes? Study design and rationale of the Diabetes and Dementia (D2) study". In: *BMC Endocrine Disorders* 17.1 (2017), pp. 1–9 (cit. on pp. 6, 31).

[Pedrizzetti, 2017] Gianni Pedrizzetti, Per M. Arvidsson, Johannes Töger, et al. "On estimating intraventricular hemodynamic forces from endocardial dynamics: A comparative study with 4D flow MRI". In: *Journal of Biomechanics* 60 (2017), pp. 203–210 (cit. on p. 96).

[Pizzo, 2017] Michelle E. Pizzo and Robert G. Thorne. *The Extracellular and Perivascular Spaces of the Brain*. Elsevier Inc., 2017, pp. 105–127 (cit. on p. 29).

[Prabhakar, 2020] Hemanshu Prabhakar and Indu Kapoor. *Brain and Heart Crosstalk*. Ed. by Hemanshu Prabhakar and Indu Kapoor. Physiology in Clinical Neurosciences – Brain and Spinal Cord Crosstalks. Singapore: Springer Singapore, 2020 (cit. on p. 13).

[Randles, 2015] Amanda Randles, Erik W. Draeger, and Peter E. Bailey. "Massively parallel simulations of hemodynamics in the primary large arteries of the human vasculature". In: *Journal of Computational Science* 9.3 (2015), pp. 70–75 (cit. on pp. 97, 100).

[Ray, 2019] Lori A. Ray and Jeffrey J. Heys. "Fluid flow and mass transport in brain tissue". In: *Fluids* 4.4 (2019) (cit. on pp. 91, 95).

[Rey, 2018] Julian Rey and Malisa Sarntinoranont. "Pulsatile flow drivers in brain parenchyma and perivascular spaces: A resistance network model study". In: *Fluids and Barriers of the CNS* 15.1 (2018), pp. 1–11 (cit. on p. 29).

[Ribaldi, 2018] Federica Ribaldi et al. "Ic-P-126: Volumetric Accuracy of a Fully Automatic Tool for White Matter Hyperintensities (Wmhs) Segmentation". In: *Alzheimer's & Dementia* 14.7S_Part_2 (2018), P105–P106 (cit. on p. 48).

[Roos, 2017] Albert de Roos, Jeroen van der Grond, Gary Mitchell, and Jos Westenberg. "Magnetic Resonance Imaging of Cardiovascular Function and the Brain". In: *Circulation* 135.22 (2017), pp. 2178–2195 (cit. on p. 31).

[Ryu, 2014] Wi Sun Ryu et al. "Grading and interpretation of white matter hyperintensities using statistical maps". In: *Stroke* 45.12 (2014), pp. 3567–3575 (cit. on pp. 6, 31).

[Saito, 2021] Shimpei Saito and Hui Cheng. “Lattice Boltzmann method code”. In: *Nuclear Power Plant Design and Analysis Codes*. Elsevier, 2021, pp. 463–480 (cit. on p. 101).

[Satizabal, 2016] Claudia L. Satizabal et al. “Incidence of Dementia over Three Decades in the Framingham Heart Study”. In: *New England Journal of Medicine* 374.6 (2016), pp. 523–532 (cit. on pp. 4, 85).

[Scarsoglio, 2017] S. Scarsoglio, A. Saglietto, M. Anselmino, F. Gaita, and L. Ridolfi. “Alteration of cerebrovascular haemodynamic patterns due to atrial fibrillation: An in silico investigation”. In: *Journal of the Royal Society Interface* 14.129 (2017) (cit. on pp. 7, 36, 58, 59, 73).

[Scheltens, 2016] Philip Scheltens, Kaj Blennow, Monique M B Breteler, et al. “Alzheimer ’ s disease”. In: *The Lancet* 388.10043 (2016), pp. 505–517 (cit. on p. 3).

[Schmidt, 2017] Paul Schmidt. “Bayesian inference for structured additive regression models for large-scale problems with applications to medical imaging”. In: *PhD* (2017) (cit. on pp. 48, 64, 74).

[Schrijvers, 2012] E. M.C. Schrijvers, B. F.J. Verhaaren, P. J. Koudstaal, et al. “Is dementia incidence declining? Trends in dementia incidence since 1990 in the Rotterdam Study”. In: *Neurology* 78.19 (2012), pp. 1456–1463 (cit. on p. 4).

[Seko, 2018] Yuta Seko, Takao Kato, Tetsuya Haruna, et al. “Association between atrial fibrillation, atrial enlargement, and left ventricular geometric remodeling.” In: *Scientific Reports* 8(1) (2018), pp. 1–8 (cit. on p. 59).

[Sepehri Shamloo, 2020] Alireza Sepehri Shamloo, Nikolas Dagres, Andreas Müssigbrodt, et al. “Atrial Fibrillation and Cognitive Impairment: New Insights and Future Directions”. In: *Heart Lung and Circulation* 29.1 (2020), pp. 69–85 (cit. on pp. 4, 6, 31, 58, 71, 85).

[Sevre, 2015] Knut Sevre. *Handbook of Cardiac Anatomy, Physiology, and Devices*. Ed. by Paul A. Iaizzo. Vol. 15. 1. Springer International Publishing, 2015, p. 59 (cit. on p. 13).

[Shan, 2006] Xiaowen Shan, Xue-Feng Yuan, and Hudong Chen. “Kinetic theory representation of hydrodynamics: a way beyond the Navier–Stokes equation”. In: *Journal of Fluid Mechanics* 550.-1 (2006), p. 413 (cit. on p. 103).

[Shi, 2011] Yubing Shi, Patricia Lawford, and Rodney Hose. “Review of Zero-D and 1-D Models of Blood Flow in the Cardiovascular System”. In: *BioMedical Engineering Online* 10 (2011) (cit. on pp. 20, 22).

[Stone, 2015] Jonathan Stone, Daniel M. Johnstone, John Mitrofanis, and Michael O’Rourke. “The mechanical cause of age-related dementia (Alzheimer’s Disease): The brain is destroyed by the pulse”. In: *Journal of Alzheimer’s Disease* 44.2 (2015), pp. 355–373 (cit. on pp. 5, 31).

[Succi, 2010] Sauro Succi, Mauro Sbragaglia, and Stefano Ubertini. “Lattice Boltzmann Method”. In: *Scholarpedia* 5.5 (2010), p. 9507 (cit. on p. 101).

[Succi, 2018] Sauro Succi. *The Lattice Boltzmann Equation*. Vol. 1. Oxford University Press, 2018 (cit. on p. 95).

[Sudlow, 2015] Cathie Sudlow, John Gallacher, Naomi Allen, et al. "UKBiobank An Open Access Resource for Identifying the Causes of a Wide Range of Complex Diseases of Middle and Old Age." In: *PLoS Med.* 12 (2015), pp. 1–10 (cit. on pp. 4, 34, 73).

[Sweeney, 2018] Melanie D. Sweeney, Kassandra Kisler, Axel Montagne, Arthur W. Toga, and Berislav V. Zlokovic. "The role of brain vasculature in neurodegenerative disorders". In: *Nature Neuroscience* 21.10 (2018), pp. 1318–1331 (cit. on pp. 4, 5, 9, 72, 85).

[Sweetman, 2011] Brian Sweetman and Andreas A. Linninger. "Cerebrospinal fluid flow dynamics in the central nervous system". In: *Annals of Biomedical Engineering* 39.1 (2011), pp. 484–496 (cit. on pp. 29, 97, 113, 115).

[Tangen, 2015] Kevin M. Tangen, Ying Hsu, David C. Zhu, and Andreas A. Linninger. "CNS wide simulation of flow resistance and drug transport due to spinal microanatomy". In: *Journal of Biomechanics* 48.10 (2015), pp. 2144–2154 (cit. on p. 96).

[Thomas, 2019] John H. Thomas. "Fluid dynamics of cerebrospinal fluid flow in perivascular spaces". In: *Journal of the Royal Society Interface* 16.159 (2019) (cit. on pp. 29, 96).

[Tithof, 2019] Jeffrey Tithof, Douglas H. Kelley, Humberto Mestre, Maiken Nedergaard, and John H. Thomas. "Hydraulic resistance of periarterial spaces in the brain". In: *Fluids and Barriers of the CNS* 16.1 (2019), pp. 1–13 (cit. on p. 29).

[Tomoto, 2021] Tsubasa Tomoto, Jun Sugawara, Takashi Tarumi, et al. "Carotid Arterial Stiffness and Cerebral Blood Flow in Amnestic Mild Cognitive Impairment". In: *Current Alzheimer Research* 17.12 (2021), pp. 1115–1125 (cit. on pp. 5, 31).

[Toth, 2017] Peter Toth, Stefano Tarantini, Anna Csiszar, and Zoltan Ungvari. "Functional vascular contributions to cognitive impairment and dementia: Mechanisms and consequences of cerebral autoregulatory dysfunction, endothelial impairment, and neurovascular uncoupling in aging". In: *American Journal of Physiology - Heart and Circulatory Physiology* 312.1 (2017), H1–H20 (cit. on pp. 5, 31).

[Vanderah, 2015] Todd Vanderah and Douglas Gould. *Nolte's The Human Brain: An Introduction to its Functional Anatomy*. 7th. Elsevier, 2015, p. 720 (cit. on pp. 13, 28).

[Vardakis, 2013] John C Vardakis, Brett J Tully, and Yiannis Ventikos. "Exploring the Efficacy of Endoscopic Ventriculostomy for Hydrocephalus Treatment via a Multicompartmental Poroelastic Model of CSF Transport : A Computational Perspective". In: i.12 (2013) (cit. on p. 95).

[Veldsman, 2020] Michele Veldsman, Xin You Tai, Thomas Nichols, et al. "Cerebrovascular risk factors impact frontoparietal network integrity and executive function in healthy ageing". In: *Nature Communications* 11.1 (2020), pp. 1–10 (cit. on pp. 4, 36).

[Veluw, 2020] Susanne J. van Veluw, Steven S. Hou, Maria Calvo-Rodriguez, et al. "Vasomotion as a Driving Force for Paravascular Clearance in the Awake Mouse Brain". In: *Neuron* 105.3 (2020), 549–561.e5 (cit. on pp. 29, 91).

[Wardlaw, 2015] Joanna M. Wardlaw, Maria C. Valdés Hernández, and Susana Muñoz-Maniega. *What are white matter hyperintensities made of? Relevance to vascular cognitive impairment*. 2015 (cit. on pp. 5, 31, 34, 65, 72).

[Wardlaw, 2019] Joanna M. Wardlaw, Colin Smith, and Martin Dichgans. "Small vessel disease: mechanisms and clinical implications". In: *The Lancet Neurology* 18.7 (2019), pp. 684–696 (cit. on pp. 4, 31, 71).

[Wardlaw, 2020] Joanna M. Wardlaw, Helene Benveniste, Maiken Nedergaard, et al. "Perivascular spaces in the brain: anatomy, physiology and pathology". In: *Nature Reviews Neurology* 16.3 (2020), pp. 137–153 (cit. on pp. 5, 25, 29, 91, 96).

[Westerhof, 2009] Nico Westerhof, Jan Willem Lankhaar, and Berend E. Westerhof. "The arterial windkessel". In: *Medical and Biological Engineering and Computing* 47.2 (2009), pp. 131–141 (cit. on p. 41).

[Wilson, 2016] Mark H. Wilson. "Monro-Kellie 2.0: The dynamic vascular and venous pathophysiological components of intracranial pressure". In: *Journal of Cerebral Blood Flow and Metabolism* 36.8 (2016), pp. 1338–1350 (cit. on pp. 29, 96).

[Wolters, 2017] Frank J. Wolters, Hazel I. Zonneveld, Albert Hofman, et al. "Cerebral perfusion and the risk of dementia: A population-based study". In: *Circulation* 136.8 (2017), pp. 719–728 (cit. on pp. 5, 6, 31).

[Wolters, 2018] Frank J. Wolters and M. Arfan Ikram. "Epidemiology of Dementia: The Burden on Society, the Challenges for Research". In: vol. 1750. 2018, pp. 3–14 (cit. on pp. 3–5, 31).

[Xia, 2017] Yufa Xia, Xin Liu, Dan Wu, et al. "Influence of beat-to-beat blood pressure variability on vascular elasticity in hypertensive population". In: *Scientific Reports* 7.1 (2017), p. 8394 (cit. on p. 58).

[Xie, 2013] Lulu Xie, Hongyi Kang, Qiwu Xu, et al. "Sleep drives metabolite clearance from the adult brain". In: *Science* 342.6156 (2013), pp. 373–377 (cit. on pp. 29, 91, 95).

[Yushkevich, 2006] Paul A. Yushkevich, Joseph Piven, Heather Cody Hazlett, et al. "User-guided 3D active contour segmentation of anatomical structures: Significantly improved efficiency and reliability". In: *NeuroImage* 31.3 (2006), pp. 1116–1128 (cit. on p. 114).

[Zhang, 2001] Y. Zhang, M. Brady, and S. Smith. "Segmentation of brain MR images through a hidden Markov random field model and the expectation-maximization algorithm". In: *IEEE Transactions on Medical Imaging* 20.1 (2001), pp. 45–57 (cit. on p. 47).

[Zhong, 2009] Xiaodong Zhong, Craig H Meyer, David J Schlesinger, et al. "Tracking brain motion during the cardiac cycle using spiral cine-DENSE MRI". In: (2009), pp. 3413–3419 (cit. on p. 96).

[Zou, 1997] Qisu Zou and Xiaoyi He. “On pressure and velocity boundary conditions for the lattice Boltzmann BGK model”. In: *Physics of Fluids* 9.6 (1997), pp. 1591–1598. arXiv: 9611001 [comp-gas] (cit. on p. 105).